NASA/TP—2011-216929

Aerodynamic Simulation of Ice Accretion on Airfoils

Andy P. Broeren and Harold E. Addy, Jr.
Glenn Research Center, Cleveland, Ohio

Michael B. Bragg and Greg T. Busch
University of Illinois at Urbana-Champaign, Urbana, Illinois

Didier Guffond and Emmanuel Montreuil
Office National d'Etudes et Recherches Aérospatiales, Châtillon, France

June 2011

NASA STI Program . . . in Profile

Since its founding, NASA has been dedicated to the advancement of aeronautics and space science. The NASA Scientific and Technical Information (STI) program plays a key part in helping NASA maintain this important role.

The NASA STI Program operates under the auspices of the Agency Chief Information Officer. It collects, organizes, provides for archiving, and disseminates NASA's STI. The NASA STI program provides access to the NASA Aeronautics and Space Database and its public interface, the NASA Technical Reports Server, thus providing one of the largest collections of aeronautical and space science STI in the world. Results are published in both non-NASA channels and by NASA in the NASA STI Report Series, which includes the following report types:

- TECHNICAL PUBLICATION. Reports of completed research or a major significant phase of research that present the results of NASA programs and include extensive data or theoretical analysis. Includes compilations of significant scientific and technical data and information deemed to be of continuing reference value. NASA counterpart of peer-reviewed formal professional papers but has less stringent limitations on manuscript length and extent of graphic presentations.

- TECHNICAL MEMORANDUM. Scientific and technical findings that are preliminary or of specialized interest, e.g., quick release reports, working papers, and bibliographies that contain minimal annotation. Does not contain extensive analysis.

- CONTRACTOR REPORT. Scientific and technical findings by NASA-sponsored contractors and grantees.

- CONFERENCE PUBLICATION. Collected papers from scientific and technical conferences, symposia, seminars, or other meetings sponsored or cosponsored by NASA.

- SPECIAL PUBLICATION. Scientific, technical, or historical information from NASA programs, projects, and missions, often concerned with subjects having substantial public interest.

- TECHNICAL TRANSLATION. English-language translations of foreign scientific and technical material pertinent to NASA's mission.

Specialized services also include creating custom thesauri, building customized databases, organizing and publishing research results.

For more information about the NASA STI program, see the following:

- Access the NASA STI program home page at *http://www.sti.nasa.gov*

- E-mail your question via the Internet to *help@sti.nasa.gov*

- Fax your question to the NASA STI Help Desk at 443–757–5803

- Telephone the NASA STI Help Desk at 443–757–5802

- Write to:
  NASA Center for AeroSpace Information (CASI)
  7115 Standard Drive
  Hanover, MD 21076–1320

NASA/TP—2011-216929

Aerodynamic Simulation of Ice Accretion on Airfoils

Andy P. Broeren and Harold E. Addy, Jr.
Glenn Research Center, Cleveland, Ohio

Michael B. Bragg and Greg T. Busch
University of Illinois at Urbana-Champaign, Urbana, Illinois

Didier Guffond and Emmanuel Montreuil
Office National d'Etudes et Recherches Aérospatiales, Châtillon, France

National Aeronautics and
Space Administration

Glenn Research Center
Cleveland, Ohio 44135

June 2011

Acknowledgments

The NASA Aviation Safety Program provided the support for this research. In addition, the authors acknowledge several individuals representing the three organizations involved for their significant contributions to the success of this large collaborative effort. Former NASA Icing Branch Chief Tom Bond, now at the Federal Aviation Administration, deserves credit for building and maintaining programmatic support for this research. Mark Potapczuk, Sam Lee, and Colin Bidwell of the NASA Glenn Research Center provided technical assistance in this research. The authors thank the staff of the NASA Glenn Icing Research Tunnel (IRT) for their assistance in the two IRT ice-accretion test campaigns completed as part of this program. Tammy Langhalls, formerly at NASA Glenn, deserves special thanks for digitizing all of the ice tracings from the IRT campaigns. Frédéric Moëns of Office National d'Etudes et Recherches Aérospatiales (ONERA) Châtillon, now at ONERA Meudon, provided technical assistance in this research. Philippe Desplas, Denis CassouDesalle, and the rest of the ONERA F1 wind-tunnel personnel provided excellent support in planning and executing the full-scale model aerodynamic testing. Leia Blumenthal of the University of Illinois, now at Harvard University, made important technical contributions in the early phases of this research. Finally, the University of Illinois Aerospace Engineering Machine Shop staff facilitated the manufacture and instrumentation of many of the ice-shape simulations used for wind-tunnel testing. David Foley deserves special recognition for fabricating and instrumenting nearly all of the high-fidelity three-dimensional castings used in the Phase III and V research.

Level of Review: This material has been technically reviewed by expert reviewer(s).

Available from

NASA Center for Aerospace Information
7115 Standard Drive
Hanover, MD 21076–1320

National Technical Information Service
5301 Shawnee Road
Alexandria, VA 22312

Available electronically at http://www.sti.nasa.gov

Contents

Aerodynamic Simulation of Ice Accretion on Airfoils

Andy P. Broeren and Harold E. Addy, Jr.
National Aeronautics and Space Administration
Glenn Research Center
Cleveland, Ohio 44135

Michael B. Bragg and Greg T. Busch
University of Illinois at Urbana-Champaign
Urbana, Illinois 61801

Didier Guffond and Emmanuel Montreuil
Office National d'Etudes et Recherches Aérospatiales
Châtillon, France F–92322

Summary

This report presents the results of a collaborative research program among NASA, Office National d'Etudes et Recherches Aérospatiales (ONERA), and the University of Illinois that was designed to improve the current state of the art in aerodynamic scaling and simulation of ice accretion on airfoils. Ice accretions were classified into four types on the basis of aerodynamic effects: roughness, horn, streamwise, and spanwise ridge. The NASA Icing Research Tunnel (IRT) was used to generate ice accretions within these four types using both subscale and full-scale models. Aerodynamic testing was performed at the ONERA F1 pressurized wind tunnel using a 72-in.- (1.83-m-) chord, full-span, NACA 23012 airfoil model with high-fidelity, three-dimensional castings of the IRT ice accretions. Performance data were recorded over Reynolds numbers from 4.5×10^6 to 15.9×10^6 and Mach numbers from 0.10 to 0.28. Lower fidelity ice-accretion simulation methods were developed and tested on an 18-in.- (0.46-m-) chord NACA 23012 airfoil model at the University of Illinois wind tunnel at Mach 0.18 and a Reynolds number of 1.8×10^6. The aerodynamic accuracy of the lower fidelity, subscale ice simulations was validated against the full-scale results for a factor of 4 reduction in model scale and a factor of 8 reduction in Reynolds number. The results show that geometric scaling of the gross ice-shape features is appropriate for horn and large spanwise-ridge ice shapes. Geometrically scaled simulations of streamwise ice and roughness on the subscale model tended to produce conservative aerodynamic performance relative to the full-scale model. The results presented in this report provide guidance regarding the effect of this roughness size in the subscale model testing. The completed program has defined the level of geometric fidelity required for artificial ice shapes to yield aerodynamic performance results to within a known level of uncertainty and has culminated in a proposed methodology for subscale iced-airfoil aerodynamic simulation.

1.0 Introduction

In many applications, simulation of the ice-accretion geometry on a wing or other surface is required for aerodynamic evaluation. The measurement of the aerodynamic performance of an aircraft or wing with actual ice accretions is very difficult and expensive and seldom a practical solution. Aircraft performance data with ice accreted in flight are available (Refs. 1 to 7), but limited, because of the cost and difficulty of acquiring these data. In flight, it is difficult to document the ice-accretion geometry accurately, particularly because shedding and sublimation often occur. In addition, the accretions are difficult to attribute to a particular icing condition because of the natural atmospheric variation through which the airplane traverses. For accretions formed in an icing wind tunnel, the inability to provide adequate instrumentation, the nonuniformity of the cloud over the model, poor aerodynamic flow quality, sublimation, and increased cost also make aerodynamic measurements difficult and rare (Ref. 8). The most common way to acquire iced-airfoil and wing data is to use geometric representations of ice accretion in a dry-air wind tunnel or in flight. These geometric representations are often referred to as "artificial ice shapes" or "ice-accretion simulations."

The best current technology for creating an accurate ice-accretion simulation is the mold and casting method developed at the NASA Glenn Research Center (Ref. 9). In this method, molds are made from an ice accretion generated in an icing wind tunnel, such as Glenn's Icing Research Tunnel (IRT). From these molds, ice-accretion castings are made that maintain the major features of the ice, including the detailed surface roughness and the spanwise and chordwise variations. Typically, these castings are attached to wings and airfoils and are instrumented to obtain high-fidelity aerodynamic data (Refs. 10 to 15). This is an expensive process and is not practical for many situations, but it does generate benchmark data for iced-airfoil and wing research.

Although much of our understanding of ice-accretion aerodynamics is anchored by cast-ice simulation data, there have been very few studies employing full-scale, ice-accretion cast shapes aerodynamically tested at full-scale Reynolds and Mach numbers. The second Federal Aviation Administration (FAA) and NASA Tailplane Icing Program provides full-scale cast-ice performance data at full-scale Reynolds and Mach numbers, but the ice shapes were applied to a fully three-dimensional tailplane model (Ref. 16). The NASA Modern Airfoils Program (Ref. 17) currently provides the best airfoil performance data set at flight Reynolds and Mach numbers; but because of size limitations in the NASA Low-Turbulence Pressure Tunnel used for the aerodynamic testing, the ice accretions were obtained on a 36-in.- (914.4-mm-) chord airfoil. Ice-accretion scaling methods can provide scaling of the gross ice shape for moderate scales (Ref. 18), but not of the roughness and ice-shape details known to be aerodynamically important in some cases.

Simulations of ice accretions on airfoils and wings are needed or desirable for many applications. For flight tests or wind-tunnel tests of iced wings and airfoils for certification or research, cast ice shapes are seldom available, and lower fidelity, artificial ice shapes are required. Often wind-tunnel testing requires scale models for which no castings are available, and small-scale simulations are needed. Computational methods must geometrically model ice on airfoils and wings, and it is either impossible or impractical to model a complete, rough three-dimensional accretion. Simpler geometries that accurately represent the key features important to the aerodynamics are needed. Currently, there is only a limited understanding of how to accurately simulate the ice-accretion geometry to reproduce the aerodynamic effect of ice accretion on lifting surfaces. For the artificial ice shapes to be robust under a wide range of geometries and flow conditions, accurate artificial ice shapes need to be based on an understanding of the fundamental flow physics. Although there are commonly accepted practices supported by some research in this area, there are also remaining questions about the aerodynamic accuracy of artificial ice shapes (Ref. 19).

There are several potential sources of uncertainty in the aerodynamic results of subscale simulations of airfoil ice accretions. As discussed by Busch and Bragg (Ref. 20), these sources include ice-accretion geometry uncertainty, iced-airfoil performance measurement uncertainty, and Reynolds and Mach number effects. The uncertainties associated with ice-accretion geometry arise from its surface complexities and roughness. These geometric features are difficult to measure and document. There can be significant spanwise variations in gross ice shape and roughness features like “feathers.” The difficulty in quantifying important ice features necessarily yields uncertainties in lower fidelity simulations, particularly on subscale models, where the features may be geometrically scaled to smaller sizes. The uncertainties associated with measuring iced-airfoil aerodynamic performance include the typical instrument uncertainties associated with any airfoil test along with others that may be amplified by the presence of artificial ice on the airfoil.

Busch and Bragg (Ref. 20) address two primary sources: pressure tap placement and spanwise drag variation. The placement of static pressure taps on an artificial ice shape must be done with some care to avoid anomalous or unrepresentative surface pressures due to flow variations in and around roughness elements. In typical two-dimensional airfoil performance tests, drag measurements are performed via a wake survey. The authors document iced-airfoil cases that show a large dependence of drag coefficient on the spanwise location of the wake-survey station. This type of uncertainty can make it difficult to evaluate the effectiveness of subscale ice-shape simulations in terms of drag coefficient. Finally, the effects of Reynolds and Mach numbers can introduce uncertainty when subscale ice-airfoil data are being compared with full-scale results. The present research program was developed, in part, to address these uncertainties. The results presented in this report attempt to quantify these uncertainties in terms of the iced-airfoil maximum lift coefficient, stalling angle, and drag coefficient.

The overall goal of this work was to provide, for the first time, high-fidelity, full-scale, iced-airfoil aerodynamic data and validated subscale-model simulation methods that produce the essential full-scale aerodynamic characteristics. As originally described by Bragg et al. (Ref. 21), the research program was organized into six phases that included both subscale and full-scale model experiments. The subscale-model testing was important to minimizing overall cost while providing a validation vehicle for the subscale ice-accretion simulations. The full-scale model trials were required to obtain heretofore nonexistent benchmark aerodynamic data.

In Phase I: Ice-Shape Classification, the existing iced-airfoil aerodynamic literature was reviewed to classify ice shapes according to their aerodynamic effects. In Phase II: Subscale-Model Ice-Accretion Testing, high-fidelity ice shapes were obtained for the subscale model having the characteristics developed in Phase I. In Phase III: Subscale-Model Aerodynamic Testing, the high-fidelity ice shapes obtained in Phase II were used to develop aerodynamic simulation methods on the subscale model. In Phase IV: Full-Scale-Model Ice-Accretion Testing, high-fidelity ice shapes were obtained for the full-scale model having the characteristics developed in Phase I. In Phase V: Full-Scale-Model Aerodynamic Testing, the ice shapes acquired in Phase IV were used for aerodynamic testing on the full-scale model to obtain a benchmark data set for the validation of subscale simulation methods. Finally, in Phase VI: Simulation Validation Testing, the methods developed in Phase III were used to scale and simulate the full-scale ice shapes for testing on the subscale model at a lower Reynolds number. The objective of this phase was to “close the loop” by using the subscale model data to reproduce the aerodynamic effects of the ice shapes tested on the full-scale model at high Reynolds numbers.

The purpose of this comprehensive final report is to describe the research and key results conducted in each phase. This research program has produced a number of papers and reports that document the work conducted during each phase in much more detail. These works are cited throughout this report in the context of the appropriate phase of the program.

2.0 Symbols

α	airfoil angle of attack
α_{stall}	stalling angle of attack, coincident with the maximum lift coefficient
c	airfoil chord length
C_d	drag coefficient
$C_{d,\,\text{casting}}$	drag coefficient for the three-dimensional casting
$C_{d,\,\text{sim}}$	drag coefficient for the simulation
$\Delta C_{d,\text{rms}}$	root-mean-square percent difference in drag coefficient between the lower fidelity simulation and the three-dimensional casting simulation over a given angle-of-attack range
$\Delta C_{d,\text{rms,bal}}$	root-mean-square percent difference in drag coefficient from the force balance between the lower fidelity simulation and the three-dimensional casting simulation over a given angle-of-attack range
C_l	lift coefficient
$C_{l,\alpha}$	lift-curve slope
$C_{l,\text{max}}$	maximum lift coefficient, coincident with stalling angle
C_m	quarter-chord pitching-moment coefficient
C_p	pressure coefficient
k	ice-roughness height or thickness
LWC	liquid water content
M	freestream Mach number
MVD	median volume diameter
N	number of angles of attack
Re	Reynolds number based on chord
s	surface length along airfoil profile
x	chordwise position along airfoil
y	normal position from airfoil chord line
δ	boundary-layer thickness

3.0 Phase I: Ice-Shape Classification

In the first phase of the research, ice-shape classifications were developed on the basis of the aerodynamics unique to each type. There are many types of ice accretions documented in the literature that are characterized by the accretion process. These include rime ice, glaze ice, mixed ice, beak ice, runback ice, and intercycle ice. Although these classifications are appropriate for thinking about the accretion of ice, they may not be as useful when the objective is aerodynamic simulation. In an initial stage of this research, Bragg et al. (Refs. 22 and 23) examined the icing aerodynamics literature and developed four fundamental types based on the flowfield physics. These ice-shape classifications are (1) roughness, (2) horn ice, (3) streamwise ice, and (4) spanwise-ridge ice. The important aerodynamics associated with each of these classifications is summarized in the following paragraphs. Much of this discussion is taken from Bragg et al. (Refs. 22 and 23), and more details can be found therein.

Ice roughness occurs during the initial stages of the accretion process before a significant ice shape, such as a horn, is accreted. The other three ice types are also "rough," but here the initial surface roughness does not significantly alter the airfoil contour or the inviscid flowfield. Ice roughness may be associated with glaze, rime, or mixed conditions and also results from the operation of ice-protection systems such as pneumatic deicers. A key aerodynamic feature of ice roughness is that it is usually much larger than the local boundary-layer thickness even at the very early stages of development. These roughness elements each act as bluff bodies with their own three-dimensional separated flowfield. In fact, the distinguishing characteristic of ice roughness and the other types of ice can be described in terms of the extent of boundary-layer separation. Horn, streamwise, and spanwise-ridge ice shapes are characterized by separated flow regions that are primarily two dimensional with characteristic lengths that are often large in comparison to the height of the ice accretion. In contrast, the separated flow regions generated by ice roughness are fundamentally three dimensional, are very local to the roughness elements, and are similar in scale to the roughness itself.

Roughness is characterized by its height, concentration (or density), and surface location and distribution. Its effect on airfoil performance depends on all of these parameters. Roughness shape can also be significant, but the irregular shapes seen in ice roughness are not thought to be as important as, and are certainly less well understood than, the other three parameters. Roughness can affect airfoil performance in several ways. The roughness elements themselves can extract momentum from the flow and cause boundary-layer separation near the trailing edge (Refs. 22 to 24). Trailing-edge separation can

contribute to reduced lift coefficients at lower stalling angles of attack. Roughness usually promotes bypass transition in the boundary layer that can lead to increased skin friction. These effects manifest themselves as performance degradation—increased drag and decreased maximum lift.

Longer icing exposures under glaze and mixed icing conditions usually result in the formation of horn ice. The horn ice shape can be characterized by its height, the angle it makes with the chord line, and its location indicated by s/c (the nondimensional surface length along the airfoil profile, distance/chord). The most pervasive feature of the horn ice flowfield is the large separation bubble that forms downstream of the horn. The stagnation point is usually located on the ice shape, and the boundary layer cannot negotiate the large adverse pressure gradient encountered at the tip of the horn. Thus the separation location remains approximately fixed at the horn tip over a large angle-of-attack range. The separated shear layer undergoes transition to turbulent flow and then usually reattaches to the airfoil surface downstream. The separation bubble causes a large redistribution of pressure that results in pitching moment changes and decreased lift; it also greatly increases the airfoil drag. This flowfield is also known to be unsteady and three dimensional. These factors make computational simulation extremely challenging. Therefore, understanding the behavior of the separation bubble is a key to understanding horn ice aerodynamics.

For this shape, it is somewhat paradoxical that the separation bubble features that make the flow complicated for analysis and computational modeling simplify the effects on lift, drag, and pitching moment. For example, several studies (Refs. 16 and 25 to 28) have shown that very simple geometries, such as a leading-edge "spoiler," can reproduce the performance characteristics of a horn ice shape. A simple geometry representing the height, angle, and location of the ice horn, essentially generates an equivalent separation bubble on the airfoil and, hence, very similar performance results. Also, the addition of surface roughness is shown in some studies (Refs. 11, 25, 27, and 29) to have only minor effects on the integrated performance.

Streamwise ice has the smallest effect of the nonroughness ice accretions and has received the least attention in the literature. Therefore, an understanding of the aerodynamics of these accretions is not as developed as for the horn and spanwise-ridge ice. Streamwise ice is often formed as a result of rime icing conditions that occur at cold temperatures when the incoming water droplets freeze on the surface upon impingement. As a result, the initial ice accretion that forms follows the contour of the airfoil surface. At large accretion times, or when the icing conditions are otherwise appropriate, streamwise ice shapes can occur that are not as conformal to the original airfoil surface and may grow a hornlike feature into the flow. In some cases, flow separation may result as with horn ice. However, these separation bubbles tend to be much smaller and, therefore, have less of an effect on overall flowfield and aerodynamic performance. This means that other flowfield features, such as trailing-edge separation, play at least an equal role in the aerodynamics. For streamwise ice, the specific ice geometry and surface roughness characteristics can be important factors in the aerodynamics.

For the streamwise ice geometries that are conformal to the airfoil leading edge, the stagnation point at moderate lift coefficients occurs on the ice shape, and the boundary layer remains attached as it flows around the leading edge of the ice and downstream on the upper surface. Since the streamwise ice/airfoil intersection is not smooth, an adverse pressure gradient may exist in this area and flow separation may occur in the junction region. The flow separation location is not fixed to a specific point on the ice shape like it is fixed to the tip for a horn shape, but it can move upstream or downstream depending upon the angle of attack and incoming boundary-layer state, which depend on the surface roughness, Reynolds number, and other factors. For a streamwise ice shape having a hornlike feature oriented into the flow direction, a larger separated flow region may exist especially at higher angles of attack. These separation bubbles are typically much smaller than for horn ice and thus do not have as large of an effect on the stall mechanisms (Refs. 11 and 30).

Spanwise-ridge ice accretions are perhaps most often associated with supercooled large-droplet (SLD) icing conditions. Usually these accretions form downstream of leading-edge ice-protection systems and, despite their association with SLD, can occur for all drop-size ranges. Runback icing can form ridge accretions and usually occurs when there is a heated leading-edge ice-protection system that is not evaporating all of the impinging water. Some water flows downstream on the surface from the heated section and freezes on the cooler, unheated surface. Because of the formation mechanisms just described, ridges often exhibit extensive spanwise variation in their geometry. These properties, and the associated flowfield, make the spanwise ridge-type accretion different from the horn shapes discussed previously. Spanwise-ridge ice can have more severe aerodynamic effects, and the shapes themselves are typically more three-dimensional than horn shapes. Spanwise ridges are generally located farther downstream than horns or streamwise shapes. This distance allows the boundary layer to develop, perhaps transition, or become transitional because of small ice roughness upstream of the spanwise ridge. Thus the spanwise ridge acts as a flow obstacle.

The unique characteristics of the ridge—a large spanwise variation and a downstream location—make the resulting aerodynamics and performance different from those for horn ice. The chief similarity is the large separation bubble downstream of the spanwise ridge, which can be complex, three dimensional, and highly unsteady. Spanwise ridges also have a separation bubble upstream of the ridge because the ridge is located well downstream of the stagnation point. This upstream separation can be a further challenge for computational simulation. The fact that the ridge is located down-

stream of the stagnation point also amplifies the effect of airfoil geometry, which is characterized by the clean airfoil pressure distribution, much more so than in the horn case. Other important features are the geometry, size, and location of the ridge on the airfoil (Ref. 31).

Later research conducted for spanwise ridges has revealed some potentially important differences in the fundamental aerodynamics between "short" and "tall" ridges. Broeren et al. (Refs. 32 and 33) distinguish between short and tall spanwise-ridge shapes on the basis of their effect on the airfoil pressure distribution and resulting aerodynamics. In the case of spanwise-ridge ice, this distinction recently led Broeren et al. (Refs. 32 and 33) to propose this subsclassification of spanwise-ridge ice. In the case of short ridges, the separation bubble is small and stable and does not substantially increase in size with increasing angle of attack. The effect on the pressure distribution is minimal, thus resulting in significantly lower aerodynamic penalties relative to tall spanwise ridges. Although much has been learned from this recent work, more research is required to further develop the short-ridge aerodynamic characteristics.

This brief summary of the salient characteristics of each type of ice shape presents a convenient classification of iced-airfoil aerodynamics. Real ice shapes may not fit neatly into only one classification, and of course, it is not realistic to think of these classifications as rigid, or unchanging. Undoubtedly more research will yield greater insight into the aerodynamics and may lead to further development of these concepts, as has already occurred in the case of spanwise ridges. Perhaps an additional classification will be added in the future. Future considerations notwithstanding, the present analysis formed the foundation for the research described in this report.

4.0 Phase II: Subscale-Model Ice-Accretion Testing

The objective of this phase was to obtain high-fidelity ice shapes having characteristics of the four types developed in Phase I. To obtain these ice shapes, a subscale model was subjected to simulated, in-flight icing conditions in an icing wind tunnel. The icing conditions were based on the in-flight icing environment that a commuter aircraft might encounter. Molds were acquired of the ice accreted on the model under these conditions. Castings were then made from these molds and used as the high-fidelity ice shapes for the tests in Phase III. The purpose here was not to produce scaled ice-accretion geometry, but to generate ice accretions that were representative of the four ice classifications to use for aerodynamic simulation development in Phase III.

The subscale ice accretions were acquired in Glenn's IRT. The IRT is a closed-return, refrigerated wind tunnel that contains a system of spray nozzles that are used to simulate in-flight icing cloud conditions (Ref. 34). The test section is 72 in. (1.83 m) high by 108 in. (2.74 m) wide by 240 in. (6.10 m) long. It has a maximum speed of 570 ft/sec (174 m/s) with no model installed. The total temperature can be controlled from –20 to 33 ºF (–29 to 0.5 ºC) via a heat exchanger located in the settling chamber supplied by an external refrigeration plant. Also located in the settling chamber are 10 horizontal spray bars that contain 251 individually controlled spray nozzles used to generate icing clouds within Code of Federal Regulations (CFR) Part 25, Appendix C icing certification envelopes (see Ref. 35).

The NACA 23012 airfoil model used in this phase of the testing had an 18-in. (0.46-m) chord and spanned the 72-in. (1.83-m) height of the IRT test section. The NACA 23012 airfoil was chosen for this research program because it is representative of a family of airfoils commonly used in the airframe industry and has been shown to be aerodynamically sensitive to ice accretion. Thus, aerodynamic penalties are amplified, resulting in a more severe testing of the simulation methods. The model was equipped with pressure taps that facilitated model alignment and a removable leading-edge section that facilitated the molding of selected ice accretions. For the spanwise-ridge ice accretion, an electric foil heater was attached to the removable leading edge. Icing conditions and heater settings were adjusted to create conditions where water flowed downstream over the heater and then froze as a spanwise ridge aft of the heater on both the upper and lower surfaces of the model. Figure 1 shows a photograph of the model in the IRT.

Selecting the icing conditions for this phase of the program began with the consideration of a full-scale commuter aircraft operating in various natural icing environments. As described by Blumenthal (Ref. 36), a representative commuter aircraft with a wing section similar to the NACA 23012 airfoil was reviewed and analyzed in terms of aircraft weight, airspeeds, lift requirements, and other factors. The analysis provided information on the desired airspeeds and model angles of attack to

Figure 1.—Subscale NACA 23012 ice-accretion model installed in the NASA Icing Research Tunnel.

TABLE 1.—ICING CONDITIONS FOR SUBSCALE ICING TESTS—ICE ACCRETIONS SELECTED FOR AERODYNAMIC TESTING IN PHASE III

[IRT, Icing Research Tunnel; α, angle of attack; MVD, median volume diameter; LWC, liquid water content.]

Ice-shape classification	IRT run	Airspeed, kn	α, deg	MVD, μm	LWC, g/m^3	Total temperature		Static temperature		Spray time, min
						°F	°C	°F	°C	
Roughness	ED0762	200	2.0	15.4	0.75	28.0	–2.2	18.5	–7.5	0.5
Horn	ED0735	200	2.0	15.4	0.75	28.0	–2.2	18.5	–7.5	5.0
Streamwise	ED0730	175	5.3	15.0	0.30	0.0	–17.8	–7.4	–21.8	5.0
Spanwise ridge	ED0760	175	0.9	15.0	0.64	24.0	–4.4	16.8	–8.5	5.0

use in the testing. Icing cloud conditions were initially selected from the CFR Part 25, Appendix C, icing envelopes. Icing scaling methods (Ref. 18) were then applied to help attain reasonable similarity in impingement limits, the collection efficiency, the freezing fraction, the accumulation parameter, and other scale factors. In addition, for some cases, analysis was conducted using the LEWICE ice-accretion software program (Ref. 37). This analysis helped to ensure that the icing conditions would generate representative ice accretions. Further adjustments to the icing conditions were made so that the test conditions fell within the IRT's operating envelope.

The ice accretions produced in the IRT were recorded using photographs, ice tracings, and ice-depth measurements. When a particular ice accretion was selected for Phase III testing, the accretion was repeated and a mold was made for that run. Molds were made of 16 ice accretions: 6 of these were horn accretions, 4 were streamwise accretions, and 3 each were roughness and spanwise-ridge accretions (see Ref. 36). Castings were subsequently made from each of these molds. The best representatives of the four classifications of ice shapes determined in Phase I formed the reference ice shapes for aerodynamic testing in Phase III. Table 1 provides the IRT test conditions for these four ice accretions. These ice shapes and the resulting aerodynamic effects are described in the following section.

5.0 Phase III: Subscale-Model Aerodynamic Testing

Phase III of the program explored methods for geometrically simulating ice accretions in each of the four classifications. Since each of the four types has different fundamental aerodynamics, if techniques can be developed to simulate these four shapes, then most ice accretions can be simulated. A variety of simulation methods can be found in the literature and in practice, and these were categorized for the subscale testing. The simulation categories or methods considered were three-dimensional casting, two-dimensional smooth, simple geometry, and simple geometry with spanwise variation. The roughness associated with ice accretion can be accounted for by adding distributed grit roughness to each of the noncasting simulation methods. The highest fidelity simulation method is considered to be the three-dimensional casting, since this is manufactured directly from a mold of the ice accretion. It is considered to be the benchmark for aerodynamic data that the other simulation methods are evaluated against. The purpose of this subscale testing was to explore many variations of the simulation methods in order to evaluate their ability to reproduce the proper iced-airfoil aerodynamics. In this way, the accuracy of the various simulation methods was systematically quantified. This phase of the program also addressed uncertainties associated with the ice-shape geometry and aerodynamic performance measurements. Quantifying this accuracy at small scale and understanding the aerodynamic differences of the simulation methods was a key to successfully executing Phase VI of this program.

5.1 Ice Accretions and Simulation Methods

The ice accretions selected in each of the four categories are shown in Figure 2 to Figure 5. Figure 2 shows the ice accretion typical of initial roughness. There is a very smooth zone on the leading edge in the stagnation-point region, followed by distributed roughness downstream. Tracings for this type of ice shape were not obtained because the ice tracing method could not adequately capture such geometric features. The horn shape shown in Figure 3 is a classic glaze ice shape with an upper and lower horn structure typical for this icing condition. The streamwise shape shown in Figure 4 is typical of a rime ice condition, having a smooth zone in the stagnation region with rime feathers and roughness downstream. Finally, the spanwise-ridge shape is shown in Figure 5. Both an upper and lower surface ridge formed because water flowing off of the heated surface froze downstream. Casting simulations were manufactured for aerodynamic testing from molds of each of these accretions.

The various lower fidelity simulation methods are described in detail by Busch et al. (Refs. 27, 28, and 38) and are summarized here using the horn ice shape as an example. Two-dimensional smooth simulations have been commonly used in previous work (Refs. 11 and 15 to 17). Digitized

Figure 2.—Photograph of subscale model ED0762 roughness shape. (No tracing was made for this shape.)

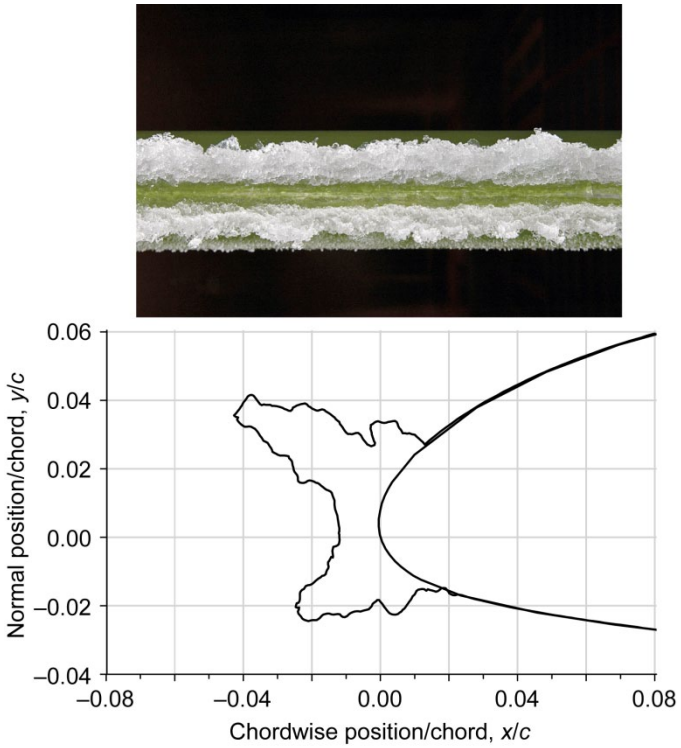

Figure 3.—Photograph and tracing of subscale model ED0735 horn ice shape.

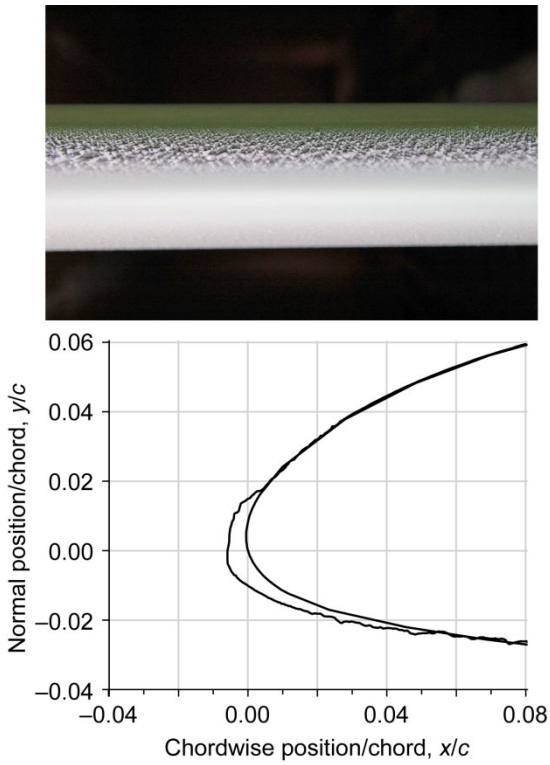

Figure 4.—Photograph and tracing of subscale model ED0730 streamwise ice shape.

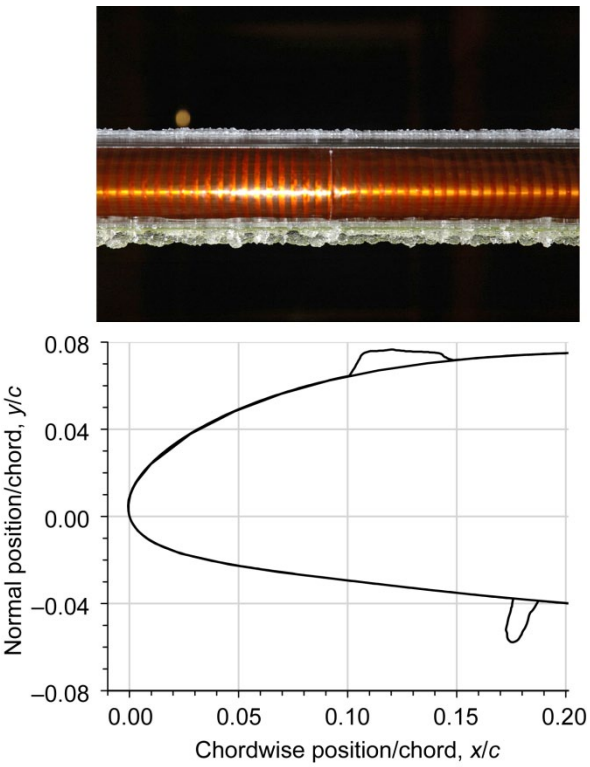

Figure 5.—Photograph and tracing of subscale model ED0760 spanwise-ridge ice shape.

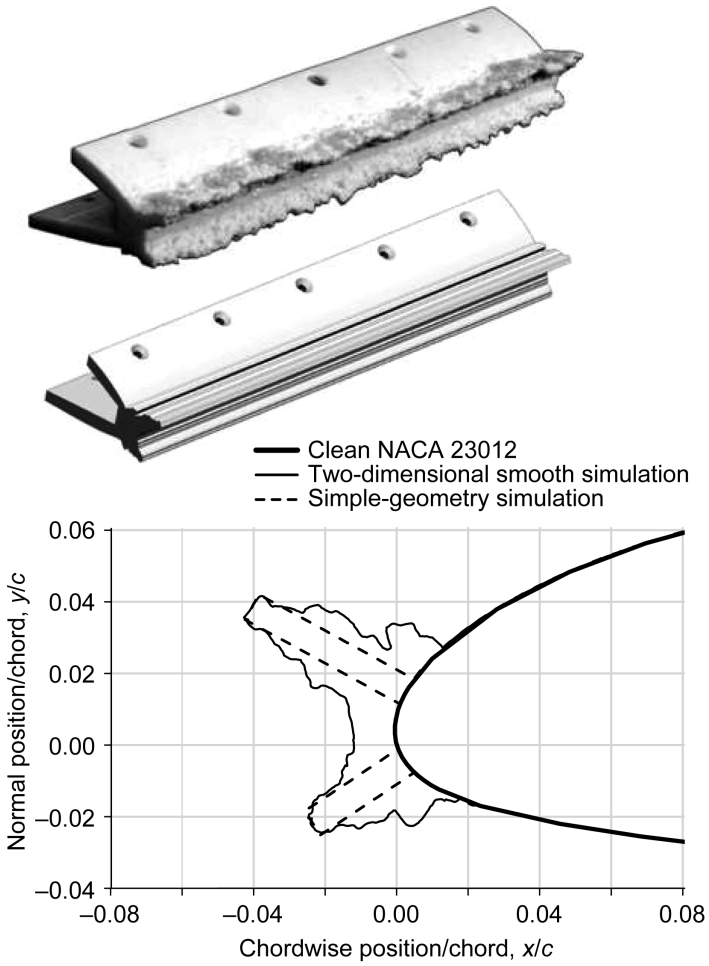

Figure 6.—Comparison of three-dimensional casting, two-dimensional smooth simulation, and simple-geometry simulation for ED0735 horn ice shape.

pencil tracings of ice shapes were processed using Surface Modeling and Grid Generation for Iced Airfoils (SmaggIce, Ref. 39) to create this type of simulation. This software assists in removing the point anomalies that often occur in digitized pencil tracings. It can also be used for smoothing; however, no smoothing was performed with SmaggIce. This tracing was then "extruded" across the model. The resulting shape is shown in Figure 6 along with an image of the three-dimensional casting for comparison. The simple-geometry simulation method entails replacing the major ice features with basic geometric shapes. The upper and lower surface horn structures were replaced with rectangular shapes that mimic the height, angle, and surface location (see Figure 6). This simulation method is also based on previous work by Papadakis et al. (Refs. 16, 25, and 26), who used spoiler ice simulations and methods by Kim and Bragg (Ref. 40). Other variations of the simple-geometry shape also were considered, including a simulation where the horns had a periodic spanwise variation in height based on measurements of the three-dimensional casting simulation (Ref. 28). Both the two-dimensional smooth and the simple-geometry simulations were also tested with various sizes of roughness applied to the external surfaces.

5.2 Experimental Methods

The subscale-model aerodynamic testing was carried out at the University of Illinois at Urbana-Champaign using the low-speed, low-turbulence wind tunnel. This facility has a 33.6-in. (0.85-m) by 48-in. (1.2-m) test section capable of speeds up to Mach 0.20. An 18-in.- (0.46-m-) chord NACA 23012 model was designed and built specifically for this program. Figure 7 shows the NACA 23012 model installed in the University of Illinois wind tunnel. The model was designed with interchangeable leading edges that accommodated the various ice simulations. There was a baseline leading edge having the NACA

Figure 7.—Subscale NACA 23012 aerodynamic model installed in the University of Illinois wind-tunnel test section.

23012 profile that was used to document the un-iced, or clean, airfoil performance, and there were two ice leading edges with truncated nose geometry that allowed for the attachment of the ice simulations. The three-dimensional ice castings were made from a hard, two-part polyurethane material of the very low viscosity required to flow into the intricate details of the ice molds. The spanwise length of the finished castings was limited to one-third of the model span, so that three identical casting sections were required to cover the span of the model in the Illinois wind tunnel. The simulations bolted on to this leading edge and thus had a rigid, repeatable mounting system. The model had a main chordwise row of pressure taps, a secondary chordwise row, and a set of spanwise taps on the upper surface. The three-dimensional casting and two-dimensional smooth ice-shape simulations also had pressure taps installed at certain locations that were identified in an earlier study (Refs. 36 and 41). The pressure tap placement was important on the irregular surfaces of the ice simulations to avoid unrepresentative static pressure readings.

The model lift and pitching moment data were acquired from a force balance and by integration of airfoil surface static pressures measured by an electronically scanned pressure system. Excellent agreement between these methods was obtained for the clean model configuration. The agreement was also good in most of the iced-model configurations with pressure-tapped ice simulations. There were a number of lower fidelity ice simulations, such as the simple-geometry shapes, that were not instrumented with pressure taps. Therefore, the lift and pitching moment data shown in this report for the subscale-model tests were obtained from the force balance for consistency. Momentum-deficit methods were used to compute the drag coefficient from total-pressure measurements collected by a traversable wake rake. This wake rake is shown downstream of the model in Figure 7. Also, surface-oil flow visualization was also conducted for selected cases. This method involves applying a light coat of mineral oil treated with fluorescent dye to the surface of the model in the region of interest. The tunnel flow condition is then set and maintained for a period of time sufficient to allow the local wall shear stress to cause the oil to flow on the surface. The resulting oil-flow patterns indicate boundary-layer transition and regions of attached and separated flow.

Busch (Ref. 38) provides more details about the experimental setup, including the experimental uncertainties summarized in Table 2. These uncertainties were all considered to be acceptable for this investigation. Although the relative uncertainty in quarter-chord pitching moment coefficient C_m appears to be large because the reference value is small, the absolute uncertainty is reasonable. The methods of Allen and Vincenti (Ref. 42) were used to correct the angle of attack α, lift coefficient C_l, pitching-moment coefficient C_m, and drag coefficient C_d for wind-tunnel wall boundary effects. All data were collected at a Reynolds number of $\mathrm{Re} = 1.8\times10^6$ and a corresponding Mach number of $\mathrm{M} = 0.18$.

TABLE 2.—ESTIMATED EXPERIMENTAL UNCERTAINTIES FOR AERODYNAMIC DATA FROM SUBSCALE MODEL TESTING IN UNIVERSITY OF ILLINOIS WIND TUNNEL

Aerodynamic quantity	Reference value	Absolute uncertainty	Relative uncertainty, percent
Angle of attack, α	4.16°	±0.02°	±0.48
Lift coefficient, C_l balance	0.548	±0.00019	±0.35
Pitching moment coefficient, C_m balance	–0.0020	±0.00023	±12.1
Pressure coefficient, C_p	–0.962	±0.0045	±0.47
Drag coefficient, C_d wake	0.0071	±0.00014	±1.9

5.3 Results and Discussion

Numerous experimental trials were conducted to investigate the aerodynamic effectiveness of the various ice-shape simulation methods. Some sample results are provided here for each of the ice shapes listed in Table 1 and shown in Figures 2 to 5.

5.3.1 ED0762 Roughness

The aerodynamic results presented in Figure 8 show C_l, C_m, and C_d versus α for the clean airfoil, the airfoil with the three-dimensional casting, and three sizes of distributed roughness. The average ice roughness height divided by the chord length on the ED0762 casting was $k/c = 0.0025$ on the upper surface and $k/c = 0.0012$ on the lower surface. The distributed roughness simulations were $k/c = 0.0009$ glass microbeads applied with an 80-percent concentration (80 percent of the surface area was covered by roughness elements), and $k/c = 0.0026$ and 0.0033 carborundum grains applied with a 50-percent concentration. The smooth zone near the stagnation point (see Figure 2) was preserved, and the roughness was applied evenly to the upper and lower surface at the appropriate locations to mimic the actual ice accretion. Since the roughness shape ED0762 was (by definition) fundamentally three dimensional, the two-dimensional smooth and simple-geometry simulations were not applicable in this case. A two-dimensional smooth simulation would simply be the clean airfoil leading-edge geometry. Thus, grit roughness was used exclusively to simulate the ice shape. Figure 8 shows the detrimental effect of a small amount of roughness on the performance of the NACA 23012 airfoil. For the airfoil with the three-dimensional casting, the maximum lift coefficient $C_{l,\max}$ and stalling angle α_{stall} were reduced to 0.97 and 10.3° from the clean-airfoil values of 1.48 and 14.4°, respectively. The minimum drag coefficient based on three-dimensional casting data was increased by nearly a factor of 2 with the ice roughness.

The roughness altered the shape of the lift curve in the stall region as well. The clean NACA 23012 airfoil had a leading-edge stall. McCullough and Gault (Ref. 43) characterized airfoil stall types and defined leading-edge stall as, "abrupt flow separation from the leading edge, generally without subsequent reattachment." The effect of this is observed in the sharp decrease in lift past $C_{l,\max}$. The presence of the ice roughness precipitated a change in the stalling characteristics to trailing-edge stall. In trailing-edge stall, boundary-layer separation gradually progresses forward on the airfoil upper surface with increasing angle of attack (Ref. 43). This description matches the fundamental aerodynamics of the ice roughness classification. The roughness decreased boundary-layer momentum, thus leading to early boundary-layer separation. The small changes in lift past $C_{l,\max}$ for the airfoil with the various ice simulations is indicative of trailing-edge stall.

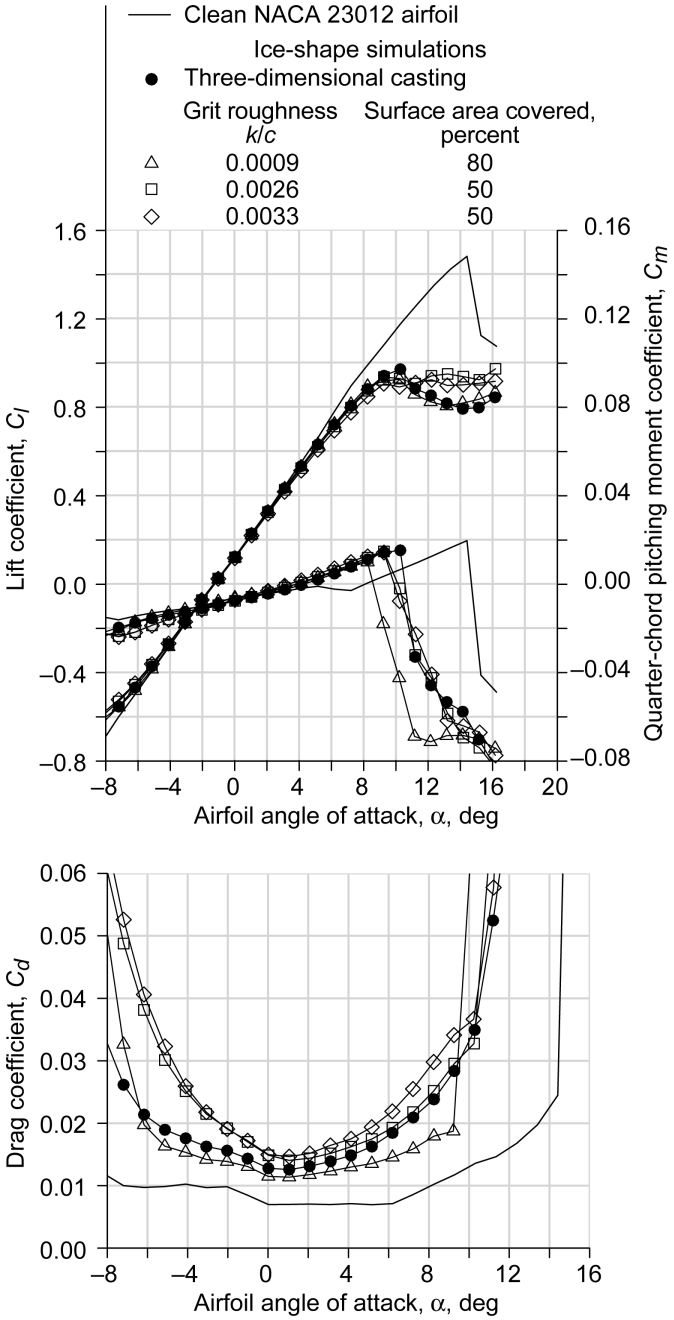

Figure 8.—Aerodynamic performance comparison for various simulations of the ED0762 roughness ice shape at a Reynolds number of 1.8×10^6 and a Mach number of 0.18; k/c, ice height per chord length.

Figure 8 also shows the varying effect of the increasing roughness size on the performance of the NACA 23012 airfoil. The lift and pitching moment coefficients were not very sensitive to changes in roughness size for the ED0762 simulations over the range tested. The data show that the most challenging aspect of ice roughness simulation lies in the drag coefficient. It was difficult to match the drag increase resulting

from the three-dimensional casting on the airfoil. To facilitate comparisons in drag coefficient, Busch et al. (Ref. 44) developed a parameter to compare C_d over an appropriate α range. The angle-of-attack range used in this research program was that over which C_l varied approximately linearly with α. The parameter $\Delta C_{d,\mathrm{rms}}$ is presented as a percentage and is computed by determining the root mean square of the percent difference between the three-dimensional casting drag coefficient $C_{d,\mathrm{casting}}$ and a given simulation drag coefficient $C_{d,\mathrm{sim}}$ at each angle of attack in the predefined linear range (a total of N angles of attack):

$$\Delta C_{d,\mathrm{rms}} = \sqrt{\frac{\sum_{i=1}^{N}\left(\frac{C_{d,\mathrm{sim}}^{i} - C_{d,\mathrm{casting}}^{i}}{C_{d,\mathrm{casting}}^{i}} \times 100\,\mathrm{percent}\right)^{2}}{N}}$$

For the ED0762 ice shape, $\Delta C_{d,\mathrm{rms}}$ was calculated on the interval $-4° \le \alpha \le 8°$. The $k/c = 0.0009$ configuration had a $\Delta C_{d,\mathrm{rms}}$ value of 14.4 percent, whereas the $k/c = 0.0026$ and 0.0033 configurations had $\Delta C_{d,\mathrm{rms}}$ values of 15.5 and 20.6 percent, respectively. The drag data indicate that the $k/c = 0.0009$ roughness simulation offered the closest match to the casting for lower angles of attack, whereas the $k/c = 0.0026$ roughness simulation offered the closest match at higher angles of attack. These data suggest that further experiments should be conducted with different grit sizes used on the upper and lower surfaces. In this case, using $k/c = 0.0026$ roughness on the upper surface and $k/c = 0.0009$ on the lower surface seems like the first logical combination. Furthermore, estimates of the actual roughness size on the casting indicate that this offers the best geometric size match as well. It is also known that the concentration, or percent surface coverage of roughness is also important to the resulting aerodynamic performance. These effects were investigated in more detail in Phase VI of the program.

The aerodynamic data are summarized in Table 3 for the three ED0762 roughness simulations. The first two columns list the lower fidelity simulation. The third column lists the difference in $C_{l,\max}$ between the airfoil with the given simulation versus the airfoil with the three-dimensional casting. The difference in percent of $C_{l,\max}$ for the three-dimensional casting configuration also is shown. Similar data are listed in the fourth column in terms of α_{stall}, and the fifth column lists the corresponding value of $\Delta C_{d,\mathrm{rms}}$. A value of zero in the last three columns is considered to show perfect agreement. The results show that the distributed roughness simulations caused lower (more conservative) $C_{l,\max}$ and α_{stall} relative to the three-dimensional casting configuration and that the $k/c = 0.0009$ roughness gave the best drag comparison in terms of $\Delta C_{d,\mathrm{rms}}$. These data support the conclusion that $C_{l,\max}$ and α_{stall} were relatively insensitive to the size of the grit roughness over the range tested. The $k/c = 0.0026$ configuration exhibited the best overall aerodynamic simulation of the three-dimensional casting. This determination was based on that configuration having the closest match to the three-dimensional casting data in terms of $C_{l,\max}$, with the values of α_{stall} and $\Delta C_{d,\mathrm{rms}}$ very similar to those for the other roughness cases.

5.3.2 ED0735 Horn Ice

Figure 9 shows the effect of the ED0735 horn shape on the performance of the NACA 23012 airfoil. As described in Phase I, the horn geometry resulted in a large upper surface separation bubble that grew with increasing angle of attack. This is consistent with the thin-airfoil stall type (Ref. 43) resulting in $C_{l,\max} = 0.66$ at $\alpha_{\mathrm{stall}} = 7.2°$ for the model with the three-dimensional casting simulation. The separation bubble also caused a significant redistribution of surface static pressure relative to the clean configuration. In terms of performance, this effect was observed most readily in the large dependence of the iced-airfoil pitching moment coefficient on angle of attack.

The large areas of separated flow contributed to large increases in drag coefficient as illustrated in Figure 9 (note the scale change in C_d from Figure 8). As mentioned in the Phase I discussion, the key to the aerodynamic simulation of horn ice is to properly represent the size and location of the horns themselves. The data in Figure 9 show very little difference in the performance coefficients for all of the various simulation configurations. The effect of roughness added to the two-dimensional smooth and simple-geometry simulations

TABLE 3.—SUMMARY OF SIMULATION EFFECTIVENESS FOR SUBSCALE MODEL ED0762 ROUGHNESS SHAPE
[$C_{l,\max}$, maximum lift coefficient; α_{stall}, stalling angle; $\Delta C_{d,\mathrm{rms}}$, root-mean-square percent difference in drag coefficient; α, angle of attack.]

Simulation roughness		Simulation $C_{l,\max}$ – casting $C_{l,\max}$	Simulation α_{stall} – casting α_{stall}, deg	$\Delta C_{d,\mathrm{rms}}$, percent ($-4° \le \alpha \le 8°$)
Ice roughness height per chord length, k/c	Area covered, percent			
0.0009	80	–0.055 (–5.7 percent)	–1.06	14.4
0.0026	50	–0.036 (–3.7 percent)	–1.02	15.5
0.0033	50	–0.065 (–6.7 percent)	–1.03	20.6

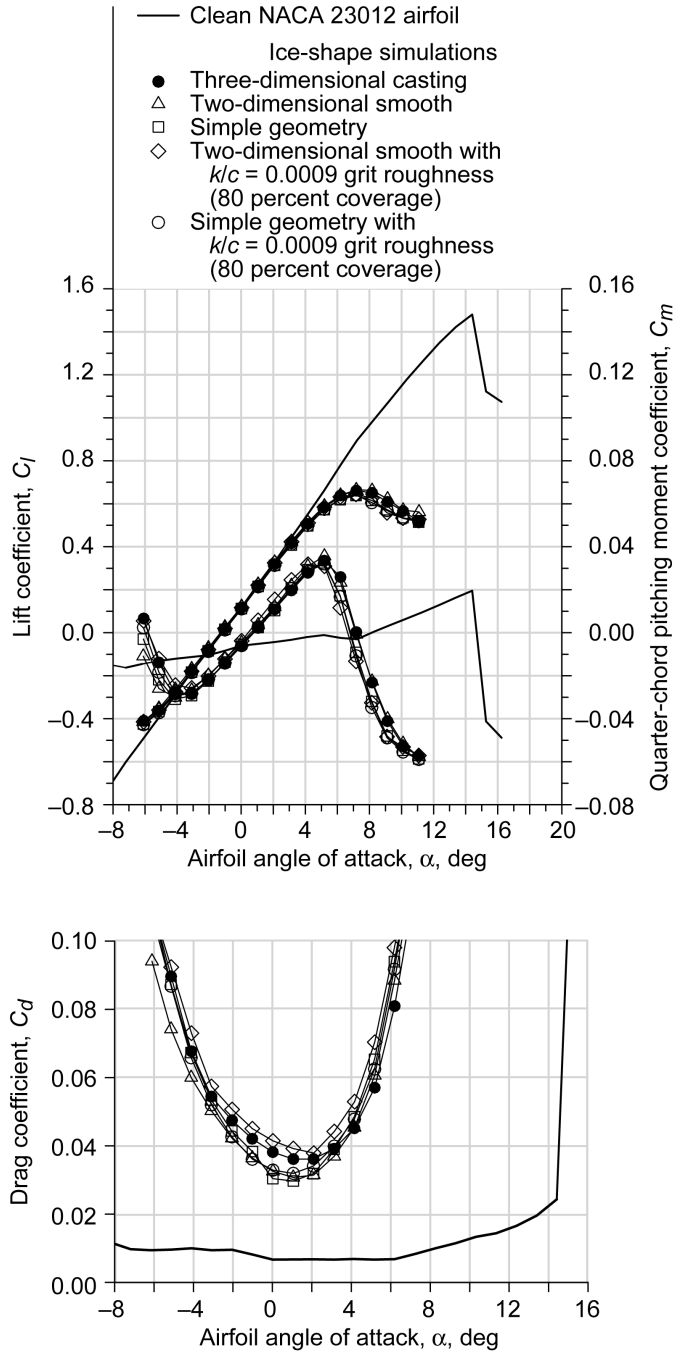

Figure 9.—Aerodynamic performance comparison for various simulations of the ED0735 horn ice shape at a Reynolds number of 1.8×10^6 and a Mach number of 0.18; k/c, roughness height per chord length.

was very small, with the possible exception of C_d. The $\Delta C_{d,\mathrm{rms}}$ values computed on the interval $-4° \le \alpha \le 6°$ only ranged from 9.4 percent (simple geometry with $k/c = 0.0009$ roughness) to 11.9 percent (two-dimensional smooth with $k/c = 0.0009$ roughness). Busch et al. (Refs. 27, 28, and 38) investigated many simulation variants for this particular ice shape to explore the effects in more detail. The authors also measured and comment on the spanwise variation in drag coefficient determined from the wake data. Busch and Bragg (Ref. 20) summarize these effects as they contribute to the uncertainties in subscale ice-shape simulation. The iced-airfoil C_d was measured to vary from 15 to 45 percent in the spanwise direction in some cases and did not appear to correlate with ice-shape geometry. The data indicate that comparisons of drag coefficient are difficult and that wake surveys should be acquired at multiple spanwise locations whenever possible.

Although the bulk of this research was focused on aerodynamic simulation as measured in terms of lift, pitching moment, and drag, simulation of the flowfield physics was equally important. That is, the low-fidelity simulations of ice accretion should replicate the key flowfield features. Since the flowfield properties were more difficult to measure and quantify, this was accomplished via analysis of chordwise pressure distributions and surface-oil flow visualizations. Busch et al. (Refs. 27, 28, and 38) provide more documentation and descriptions of these results. An illustrative example is provided in Figure 10, which is a plot of the pressure coefficient C_p for three representations of the ED0735 ice shape. The effect of the upper surface separation bubble is seen in the region of approximately constant pressure from $x/c = -0.04$ to 0.10. A similar pressure signature on the lower surface corresponds to the smaller separation bubble due to the lower surface horn. The important point for Figure 10 is that there is excellent agreement in pressure coefficient for the range of simulation fidelities. The data provide some assurance that the key flowfield physics were preserved with the two-dimensional smooth and simple-geometry simulations.

The aerodynamic data are summarized in Table 4 for the ED0735 horn ice simulations in terms of maximum lift coefficient, stalling angle,, and root-mean-square percent difference in drag coefficient. Very accurate simulation was obtained in this case as quantified by these metrics. The addition of roughness to the two-dimensional smooth and simple-geometry configurations did little to improve the simulation accuracy. As described in Phase I, accurately representing the horn ice geometry is a key to accurate aerodynamic simulation, with roughness having little effect.

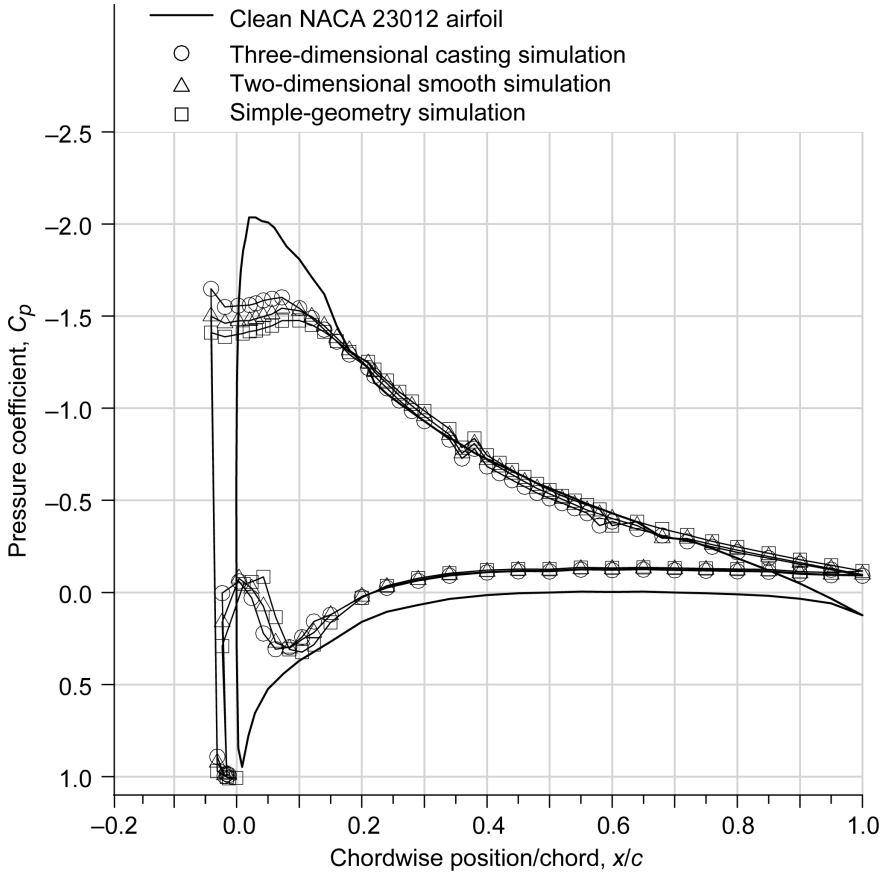

Figure 10.—Comparison of chordwise pressure distribution for various simulations of the ED0735 horn ice shape at an airfoil angle of attack of 6.2°, a Reynolds number of 1.8×10^6, and a Mach number of 0.18.

TABLE 4.—SUMMARY OF SIMULATION EFFECTIVENESS FOR SUBSCALE MODEL ED0735 HORN SHAPE
[$C_{l,\max}$, maximum lift coefficient; α_{stall}, stalling angle; $\Delta C_{d,rms}$, root-mean-square percent difference in drag coefficient; α, angle of attack; k/c, ice roughness height per chord length.]

Simulation	Simulation $C_{l,\max}$ – casting $C_{l,\max}$	Simulation α_{stall} – casting α_{stall}, deg	$\Delta C_{d,rms}$, percent ($-4° \le \alpha \le 6°$)
Two-dimensional smooth	0.001 (0.2 percent)	0.00	10.7
Simple geometry	–0.013 (–2.0 percent)	0.00	11.8
Two-dimensional smooth with 80-percent $k/c = 0.0009$	–0.017 (–2.6 percent)	0.00	11.9
Simple geometry with 80-percent $k/c = 0.0009$	–0.020 (–3.0 percent)	0.00	9.4

5.3.3 ED0730 Streamwise Ice

Figure 11 summarizes the aerodynamic effect of the ED0730 streamwise ice simulations on the NACA 23012 airfoil. The three-dimensional casting simulation reduced α_{stall} to 10.3° from the clean value of 14.4° and reduced $C_{l,max}$ to 1.02 from the clean value of 1.48. The three-dimensional casting simulation increased C_m for $\alpha > 4°$ up to stall and increased the minimum C_d to 0.01204 from the clean minimum of 0.00696. Figure 11 also shows the resulting performance with the lower fidelity streamwise ice simulations installed on the NACA 23012 airfoil (refer to Refs. 38 and 45 for geometry information). For both the two-dimensional smooth and simple-geometry simulations, α_{stall} was 11.3°, 1° higher than for the casting simulation. For the two-dimensional smooth simulation, $C_{l,max}$ was 1.15, 13.5 percent higher than for the three-dimensional casting simulation. The simple-geometry simulation yielded a $C_{l,max}$ of 1.10, 7.8 percent higher than for the three-dimensional casting simulation. The roughness added to the lower fidelity simulations caused a reduction in maximum lift and stalling angle and subsequently better agreement with the three-dimensional casting configuration. The pitching-moment data showed no major differences for the various ice-shape configurations except that they reflect the differences in stalling angle. The drag data reveal that the simple-geometry simulation had a minimum C_d that was much closer to the clean configuration than for the airfoil with the three-dimensional casting, and it therefore had a very high $\Delta C_{d,rms}$ of nearly 31 percent computed on the interval $-4° \le \alpha \le 8°$. The comparison in drag coefficient for the two-dimensional smooth simulation was much more favorable with $\Delta C_{d,rms} = 9.4$ percent. As was the case for C_l and C_m, the addition of roughness to both the two-dimensional smooth and simple-geometry simulations helped improve the agreement with the three-dimensional casting benchmark.

The flowfield features discussed in Phase I are a key to understanding these differences in aerodynamic performance. Broeren et al. (Ref. 45) and Busch (Ref. 38) describe surface-oil flow visualization data for several of the simulation configurations. An example is depicted in Figure 12 for the three-dimensional casting configuration at $\alpha = 10°$. The flow is from left to right, and the casting is visible on the left side of the image. The markings at the top and bottom indicate chordwise position, x/c in percent. The markings along the right side of the image indicate spanwise position in inches measured from the pressure tap row. The oil streaks are aligned with the chordwise flow direction and give way to a more speckled pattern between $x/c = 0.50$ and 0.60, indicating boundary-layer separation at this location. Similar flow visualizations performed at $\alpha = 6°$ and 8° clearly show that the aerodynamics leading to stall were driven by boundary-layer separation on the upper surface moving forward from the

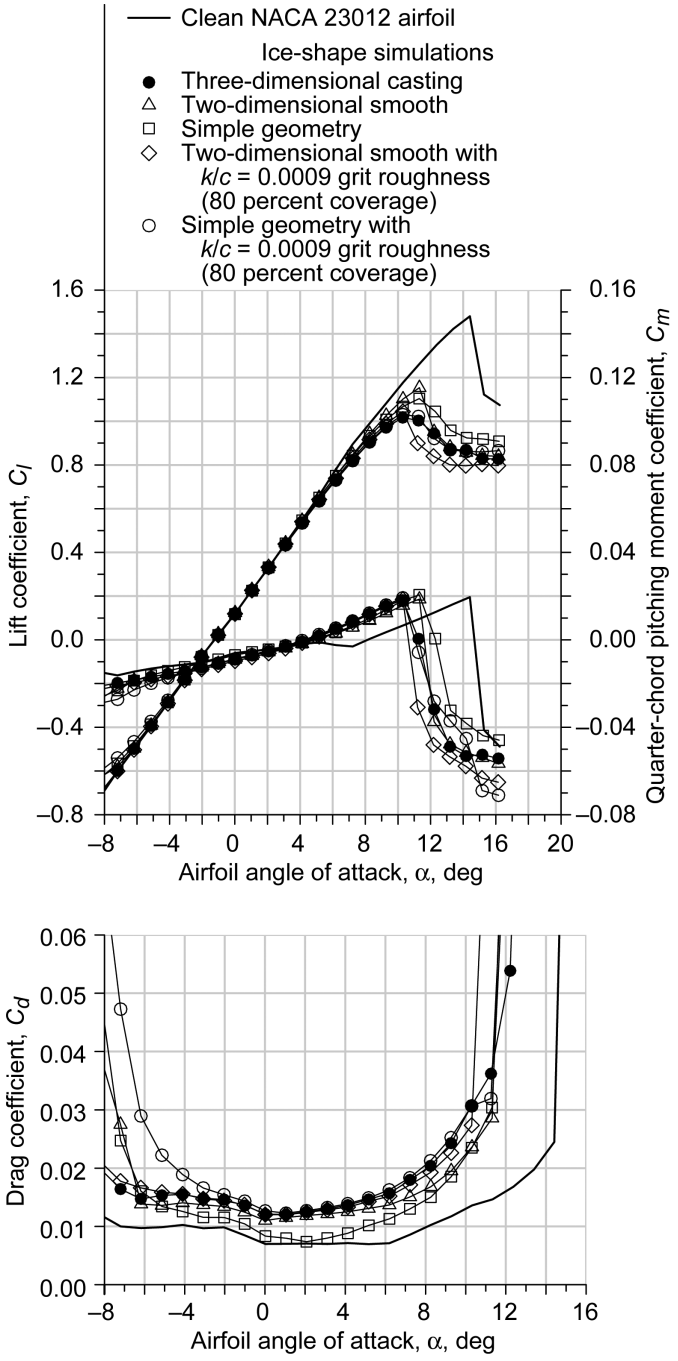

Figure 11.—Aerodynamic performance comparison for various simulations of the ED0730 streamwise ice shape at a Reynolds number of 1.8×10^6 and a Mach number of 0.18; k/c, roughness height per chord length.

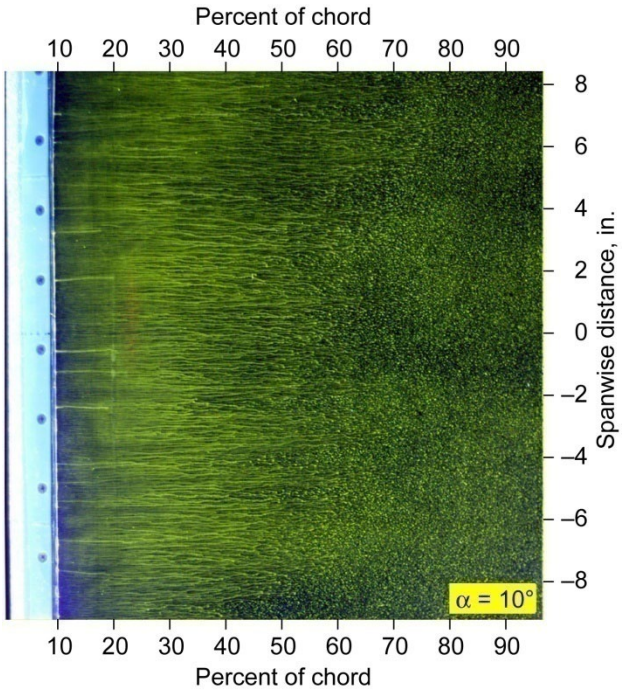

Figure 12.—Surface-oil flow visualization image for the ED0730 streamwise ice shape three-dimensional casting simulation at an airfoil angle of attack of 10°, a Reynolds number of 1.8×10^6, and a Mach number of 0.18.

trailing edge with increasing angle of attack. Therefore, the airfoil with the ED0730 three-dimensional casting simulation had a trailing-edge stall. A comparison of flow-visualization and surface-pressure-distribution data for the two-dimensional smooth and simple-geometry configurations showed less boundary-layer separation (in comparison to the three-dimensional casting configuration) at identical angles of attack. Therefore, the roughness present on the three-dimensional casting was likely responsible for the larger extent of trailing-edge separation at higher angles of attack leading to stall. Thus the grit roughness that was added to the two-dimensional smooth and simple-geometry shapes helped to improve the comparison with the three-dimensional casting data. This effect of roughness increasing the extent of boundary-layer separation explains the lower lift coefficient and higher drag coefficient observed for $\alpha > 6°$ for the three-dimensional casting and roughened configurations.

Differences in drag coefficient at lower angles of attack are more difficult to explain. For example, on the interval $-6° \le \alpha \le 6°$, the drag coefficient of the two-dimensional smooth configuration follows that of the casting much more closely than does the drag coefficient of the simple-geometry simulation. This is discussed in detail in Broeren et al. (Ref. 45), and the following discussion is adapted from that paper.

There are a number of mechanisms that may be responsible for the difference in drag coefficient for these configurations. First, the difference in the size and type of roughness may have influenced the size of any local separation zone at the ice-shape/airfoil junction. Second, the size and type of roughness may have affected the amount of boundary-layer momentum extracted by the roughness elements themselves. Often this is described as roughness element drag. Finally, the size and type of roughness may affect the boundary-layer transition process, thus affecting the contribution to drag due to skin friction in the downstream boundary layer. Determining the complicated balance of these and other factors was beyond the scope of this work. However, it was clear that there were obvious differences in the surface roughness characteristics of the simulations. The three-dimensional casting simulation had the rime feather features associated with this type of ice accretion. Aerodynamically, this could be described as three-dimensional roughness. The two-dimensional smooth simulation had spanwise running "grooves" that resulted from the pencil tracing of the rime feathers on the casting. The surface of the simple-geometry simulation was completely smooth. A simple experiment was performed where the spanwise grooves in the two-dimensional simulation were smoothed with a thin-film surface covering. The resulting measurements yielded drag coefficients that were much closer to that of the simple-geometry simulation. These results, combined with the flow-visualization results at higher angle of attack indicated that the roughness characteristics of streamwise ice are important for accurate aerodynamic simulation. This idea was developed by Bragg et al. (Refs. 22 and 23) at the outset of this research program, but it could not be confirmed because of the lack of available data at that time.

This notion led to a detailed study of roughness size and concentration for the streamwise ice accretion. Broeren et al. (Ref. 45) and Busch (Ref. 38) describe these results in detail, and they are summarized here. The effect of roughness size applied to the two-dimensional smooth and simple-geometry shapes was investigated using the baseline concentrations of 80 percent for the $k/c = 0.0009$ microbeads and 50 percent for the $k/c = 0.0026$ and 0.0033 carborundum grains. Over this range, $C_{l,\max}$ decreased nearly linearly with increasing size of added roughness. This behavior is interesting from a simulation perspective because it is different from the effect of the same roughnesses applied directly to the airfoil. In that case, as discussed earlier for the ED0762 roughness shape, $C_{l,\max}$ was practically independent of roughness size over the range tested. The effects of roughness concentration were investigated for $k/c = 0.0009$ and 0.0026 applied to two-dimensional smooth, streamwise ice simulation. There was an effective range of concentration where $C_{l,\max}$ decreased with increasing concentration. After a certain concentration was applied, 30 percent for $k/c = 0.0009$ and 20 percent for $k/c = 0.0026$, no significant decline in $C_{l,\max}$ was observed for higher concentrations.

TABLE 5.—SUMMARY OF SIMULATION EFFECTIVENESS FOR SUBSCALE MODEL ED0730 STREAMWISE SHAPE

[$C_{l,\max}$, maximum lift coefficient; α_{stall}, stalling angle; $\Delta C_{d,rms}$, root-mean-square percent difference in drag coefficient; α, angle of attack; k/c, ice roughness height per chord length.]

Simulation	Simulation $C_{l,\max}$ – casting $C_{l,\max}$	Simulation α_{stall} – casting α_{stall}, deg	$\Delta C_{d,rms}$, percent ($-4° \le \alpha \le 8°$)
Two-dimensional smooth	0.137 (13.5 percent)	1.03	9.4
Simple geometry	0.087 (8.6 percent)	1.02	30.8
Two-dimensional smooth with 80-percent $k/c = 0.0009$	0.027 (2.7 percent)	0.01	2.1
Simple geometry with 80-percent $k/c = 0.0009$	0.013 (1.3 percent)	–0.02	4.8

As described by Bragg et al. (Refs. 22 and 23) in their review, this effect of roughness concentration has been observed in other studies for roughness applied directly to the airfoil surface. This was also investigated in Phase VI of this program. Broeren et al. (Ref. 45) also present and discuss the results for drag coefficient, which were much more complicated and therefore difficult to summarize succinctly. The results do show that roughness size and concentration can be equally important. From a practical perspective, it is very difficult to quantify the size and concentration of the rime feather roughness of streamwise ice. Therefore, it is equally difficult to determine what roughness size and concentration best simulates the rime feather roughness. This is clearly a significant uncertainty in the aerodynamic simulation process for streamwise ice.

The aerodynamic effectiveness of the lower fidelity simulations and added roughness is further quantified in Table 5 for $C_{l,\max}$, α_{stall}, and $\Delta C_{d,rms}$. These data clearly show that the most accurate simulation required the addition of roughness. Note, in particular, the large improvement in drag performance with the roughness added to the simple-geometry simulation.

5.3.4 ED0760 Spanwise-Ridge Ice

Figure 13 summarizes the effect of the ED0760 spanwise-ridge ice on the NACA 23012 airfoil performance for various simulation fidelities (refer to Refs. 38 and 45 for geometry information). Inspection of the iced-airfoil lift curves shows that identifying the maximum lift coefficient is difficult and perhaps more subjective than for the previous ice shapes. This parameter was determined primarily by analyzing the surface pressure distributions for which a large chordwise extent of separated flow could be identified. For the three-dimensional casting configuration, this led to $C_{l,\max} = 0.97$ at $\alpha_{stall} = 14.2°$. Although the stalling angle was similar to that of the clean airfoil, the lift coefficient was substantially degraded. For the two-dimensional smooth configuration, $C_{l,\max}$ was 0.95, which agreed well with the three-dimensional casting configuration, except that the stall occurred at 12.2°, 2° lower. The simple-geometry simulation resulted in more severe degradation, with $C_{l,\max}$ determined to be 0.78 at $\alpha_{stall} = 11.1°$. This difference in performance is further illustrated in the pitching moment variation with angle of attack being much more negative (nose down) than for the other simulations for $\alpha > 7°$.

The effect of the spanwise-ridge shape on drag coefficient was similar in magnitude to that for the horn shape (see Figure 9). The minimum C_d for the airfoil with the three-dimensional casting spanwise ridge was 0.045 in comparison to 0.036 for the three-dimensional casting horn shape. A major contribution in drag to the former configuration was due to the lower surface ridge. As depicted in Figure 5, this ridge was large and nearly perpendicular to the airfoil surface, thus amounting to a lower surface spoiler. Other research has shown that lower surface ice can have a large effect on drag but tends to have only a minimal effect on lift at higher (positive) angles of attack (Refs. 46 and 47). The drag data in Figure 13 show that the lower fidelity simulations were not very effective in reproducing the effect of the three-dimensional casting, particularly outside of the range $0° \le \alpha \le 5°$. The addition of roughness to the lower fidelity simulations did have a measurable effect, but it did not significantly improve the aerodynamic comparison with the three-dimensional casting configuration.

As discussed for the previous ice shapes, an extensive analysis of the iced-airfoil flowfield was conducted to better understand the variations in the aerodynamic performance data. These results are described in detail by Broeren et al. (Ref. 45) and Busch (Ref. 38) and are summarized here. Surface-oil flow visualization performed for various spanwise-ridge simulations indicated that the time-averaged surface flow was characterized by three-dimensional features. At $\alpha = 8°$, there was some evidence of a small separation bubble associated with the upper surface ridge at certain spanwise stations. This was most pronounced for the simple-geometry simulation and was consistent with the larger degradations in aerodynamic performance associated with this configuration.

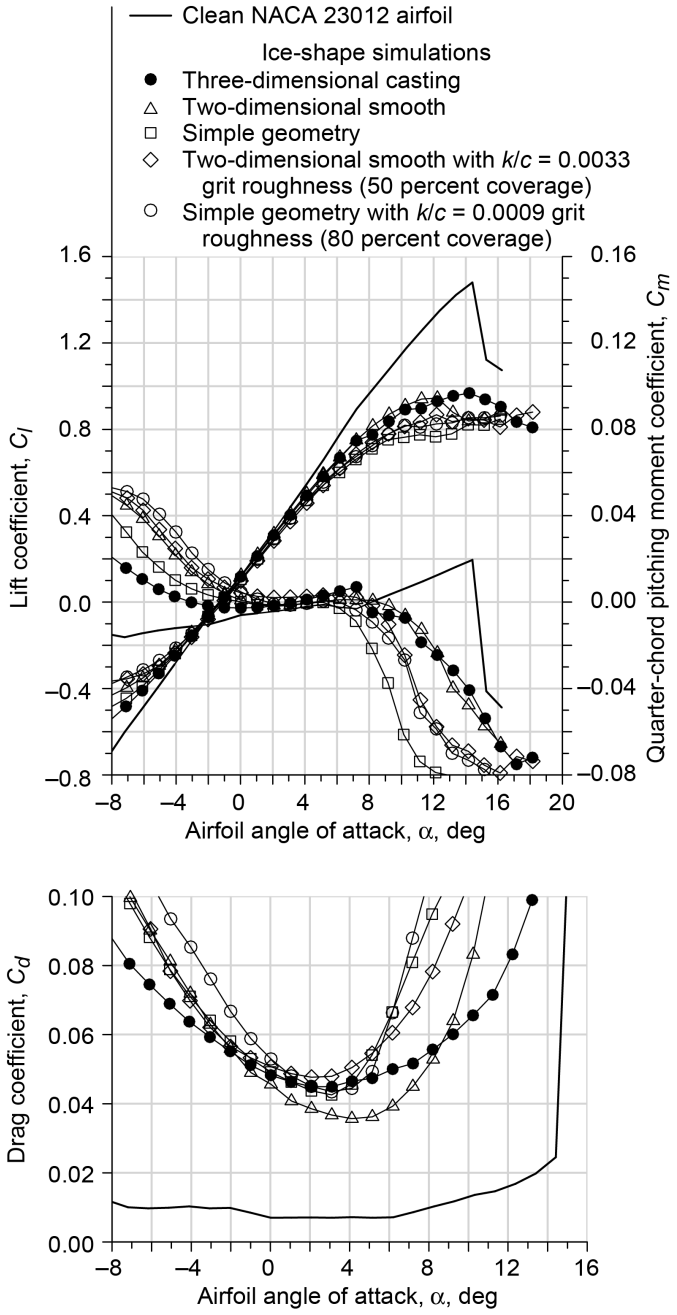

Figure 13.—Aerodynamic performance comparison for various simulations of the ED0760 spanwise-ridge ice shape at a Reynolds number of 1.8×10^6 and a Mach number of 0.18; k/c, roughness height per chord length.

The flowfield of all three configurations had evidence of trailing-edge separation for this angle of attack as well. Both of these features persisted at higher angles of attack leading to stall. As a result, the iced-airfoil stall type was classified as a combination of thin-airfoil and trailing-edge stall. In this case, the combination of flowfield features proved to be difficult to simulate accurately with the lower fidelity methods.

The surface pressure distribution comparison of Figure 14 offers a further comparison of the simulation methods. It is important to note that, although the surface flow visualization indicated spanwise variation, the pressure data were only measured at a single spanwise location. This location, however, was identical for all configurations. For all of the iced-airfoil configurations, there were characteristic discontinuities in C_p due to both the upper and lower surface ridges. All three cases had a similar pressure signature on the lower surface from $x/c \approx 0.15$ to ≈ 0.35, which indicated that the separation bubble was associated with the lower surface ridge. Since this ridge was large and relatively two-dimensional, all three simulation methods generated a similar pressure signature and likely had a similar lower surface flowfield.

The more interesting results are, of course, for the upper surface. For the three-dimensional casting and two-dimensional smooth cases, the flow accelerated to a C_p of –2.2 to –2.4, then decelerated in front of the ridge. The change in C_p across the ridge (i.e., $x/c = 0.10$ to 0.14) indicated flow acceleration over the ridge. This was followed by a steep pressure recovery with C_p that began to match the clean values at $x/c = 0.50$. There was a small divergence of the trailing-edge pressure for the three-dimensional casting and two-dimensional smooth cases from the clean configuration that was consistent with the trailing-edge separation observed in the flow visualization. For the simple-geometry simulation, the region of nearly constant pressure (from $x/c = 0.14$ to 0.24) indicated that a larger separation bubble formed aft of the ridge, consistent with the flow visualization. The data show that the flowfields for the three-dimensional casting and two-dimensional smooth configurations matched fairly closely, both of which differed from the simple-geometry configuration. The chief difference in the upper-surface ridge geometry between the two-dimensional smooth and the simple-geometry simulation was that, in the former case, the leading and trailing faces of the ridge were rounded to match the traced cross section shown in Figure 5. In contrast, the simple-geometry simulation was a simple rectangle whose leading and trailing faces were essentially perpendicular to the airfoil surface.

The importance of such a seemingly minor geometric detail to accurate aerodynamic simulation illustrates the potential difficulties for spanwise-ridge shapes. Bragg et al. (Refs. 22 and 23) discuss some aerodynamic features that can potentially

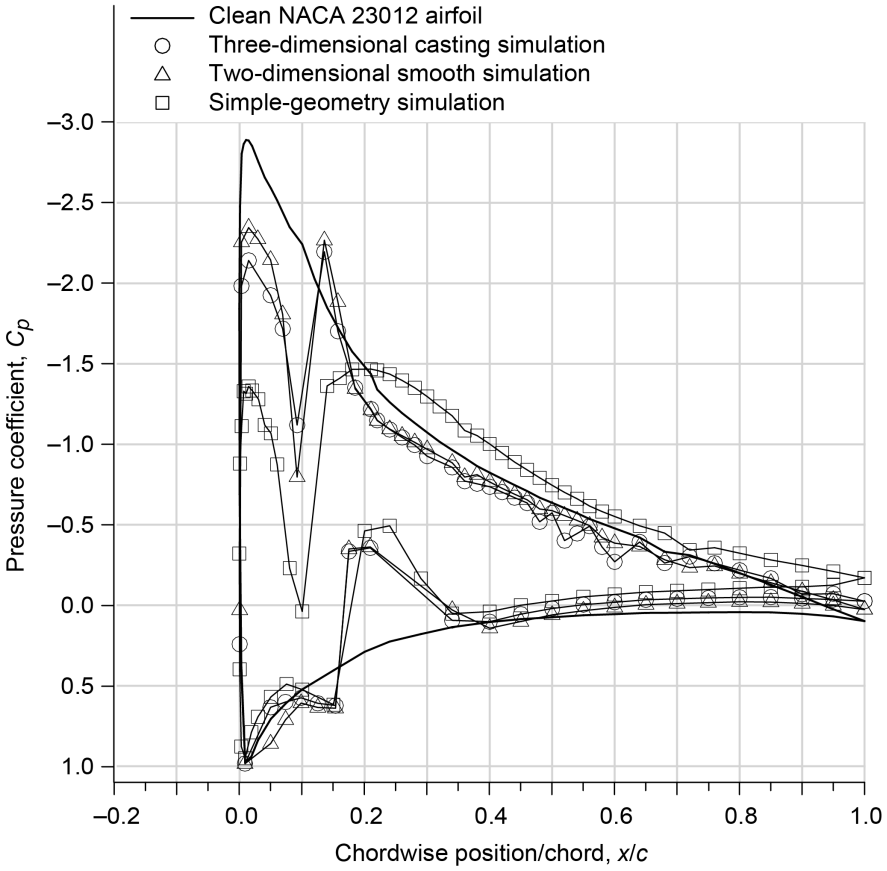

Figure 14.—Comparison of chordwise pressure distribution for the various simulations of the ED0760 spanwise-ridge ice shape at an airfoil attack of attack of 8.2°, a Reynolds number of 1.8×10^6, and a Mach number of 0.18.

contribute to this difficulty. The fact that the ridge itself was located downstream of the leading edge has several implications. A boundary layer develops on the smooth leading edge upstream of the ridge. The characteristics of this boundary layer depend on many factors including the airfoil geometry, pressure distribution, and Reynolds number. For forward-loaded airfoils like the NACA 23012, an ice ridge farther downstream would be located in a region where there would be a significant adverse pressure gradient on the clean airfoil. These factors add complexity to the flowfield via boundary-layer interactions with the ice ridge and adverse pressure gradient. Contrast this with the situation for ice located on the airfoil leading edge: the stagnation point is located on the accretion, and the pressure gradient is normally favorable. Aerodynamic simulation of spanwise ridges of similar size and type to the ED0760 case used here was addressed in later studies (Refs. 32 and 33) and led to further development of the spanwise-ridge ice classification described in Phase I.

More evidence of the complicated nature of the spanwise-ridge simulation is shown in Figure 13 for the cases where roughness was added to the lower fidelity simulations. A number of roughness cases were attempted and these results are presented and discussed by Broeren et al. (Ref. 45) and Busch (Ref. 38). As can be seen in Figure 13, there is no clear trend in the effect of added roughness. For the two-dimensional smooth simulation, the added roughness compromised the agreement with the three-dimensional casting data. The $k/c = 0.0033$ data had the least detrimental effect, but the other roughness configurations (not shown) resulted in poorer agreement. The maximum lift coefficient was reduced to 0.87 in comparison to 0.95 for the two-dimensional smooth configuration without roughness and to 0.97 for the airfoil with the three-dimensional casting simulation. Relative to the two-dimensional smooth simulation results, α_{stall} was unchanged when the roughness was added.

Comparisons in drag coefficient were complicated by the spanwise variations observed in the surface-flow visualization results. Since the wake data were acquired at a single spanwise station, it was unclear if the data were representative of the drag of the iced airfoil. Therefore, the root-mean-square

differences in drag coefficient were calculated using the force balance data for the ED0760 ice-shape simulations. Typically, drag coefficients obtained from the force balance are not reported because of inaccuracies due to model end effects and sidewall interactions. Since what was calculated here amounts to a difference in C_d values over a given α range, these differences were determined to be representative, whereas the absolute values would suffer from the described deficiencies. Therefore, the comparisons of the root-mean-square percent difference in drag coefficient from the force balance between the lower fidelity simulation and the three-dimensional casting simulation over a given angle-of-attack range, $\Delta C_{d,\mathrm{rms,bal}}$, represent a valid analysis on a relative basis. In this case, the α range was –4° to 8°. For the two-dimensional smooth simulation relative to the three-dimensional casting, $\Delta C_{d,\mathrm{rms,bal}}$ was 5.7 percent. The addition of $k/c = 0.0033$ roughness caused $\Delta C_{d,\mathrm{rms,bal}}$ to increase to 28.6 percent. Different effects were noted for the $k/c = 0.0009$ roughness added to the simple-geometry simulation. Slightly better agreement was obtained in maximum lift coefficient, but the effect of the roughness was that this occurred 1° lower in α. The comparison in drag coefficient also improved slightly, with the addition of roughness resulting in a $\Delta C_{d,\mathrm{rms,bal}}$ of 20.9 percent compared with 26.2 percent without added roughness. The contrasting nature of these results further illustrates the complexity of the aerodynamic simulation of the ED0760 spanwise-ridge shape.

Table 6 summarizes the aerodynamic data for the ED0760 spanwise-ridge ice simulations in terms of $C_{l,\max}$, α_{stall}, and $\Delta C_{d,\mathrm{rms}}$. The data show that the most accurate lower fidelity simulation was the two-dimensional smooth configuration. The other configurations could not reproduce the complicated flowfield features that were associated with this ice shape. These data clearly show the large negative impact of added roughness. It is important to note that the flowfield characteristics of the ED0760 spanwise-ridge shape were likely some combination of the tall and short ridge shapes described in Phase I (also see Refs. 32 and 33). The facts that a large separation bubble emanating from the upper surface ridge was not observed and that added roughness had a large impact on the performance suggest that the ridge was not tall. Conversely, the key characteristic of short ridges—a small, stable separation bubble—also was not observed. Therefore, simulation results for this case are not necessarily indicative of large spanwise-ridge ice shapes.

5.4 Summary of Simulation Effectiveness for Phase III

The results presented here for the Phase III research effort were selected to be a representative sample of the total data set. Much was learned about the effectiveness of the various simulation methods for each of type of ice shape. In all cases the performance of the NACA 23012 airfoil with the three-dimensional casting simulation was taken as the benchmark, and all other results are relative to it. The aerodynamic data are summarized in Table 3 to Table 6 for each of the ice shapes tested in Phase III. For each of the four ice shapes, the most accurate lower fidelity simulation was selected and included in Table 7. Selecting the most accurate was somewhat subjective because there was not a single simulation of each casting that had the lowest values of each of the three parameters (i.e., $C_{l,\max}$, α_{stall}, and $\Delta C_{d,\mathrm{rms}}$). More weight was given to $C_{l,\max}$ and α_{stall} because these values had less uncertainty than $\Delta C_{d,\mathrm{rms}}$. This was due mainly to the potential spanwise variation in drag that was not quantified for all the cases tested. Furthermore, the lower fidelity simulations with the best accuracy in terms of $C_{l,\max}$, and α_{stall} also had fairly low values of $\Delta C_{d,\mathrm{rms}}$. For example, the most accurate simulation of the ED0730 streamwise shape was the simple-geometry simulation with $k/c = 0.0009$ roughness because it had the best accuracy in terms of $C_{l,\max}$ and had an α_{stall} value that was very close to the two-dimensional smooth simulation with $k/c = 0.0009$ roughness (see Table 5). The $\Delta C_{d,\mathrm{rms}}$ of 4.8 percent for the former simulation was still considered to be fairly low, implying good overall comparison in C_d between the lower fidelity simulation and the three-dimensional casting.

TABLE 6.—SUMMARY OF SIMULATION EFFECTIVENESS FOR SUBSCALE MODEL ED0760 SPANWISE-RIDGE SHAPE

[$C_{l,\max}$, maximum lift coefficient; α_{stall}, stalling angle; $\Delta C_{d,\mathrm{rms\ bal}}$, root-mean-square percent difference in drag coefficient (balance); α, angle of attack; k/c, ice roughness height per chord length.]

Simulation	Simulation $C_{l,\max}$ – casting $C_{l,\max}$	Simulation α_{stall} – casting α_{stall}, deg	$\Delta C_{d,\mathrm{rms,bal}}$, percent ($-4° \le \alpha \le 8°$)
Two-dimensional smooth	–0.023 (–2.4 percent)	–1.98	5.7
Simple geometry	–0.193 (–20.0 percent)	–3.09	26.2
Two-dimensional smooth with 50-percent $k/c = 0.0033$	–0.100 (–10.3 percent)	–2.04	28.6
Simple geometry with 80-percent $k/c = 0.0009$	–0.149 (–15.4 percent)	–4.05	20.9

TABLE 7.—SUMMARY OF SIMULATION EFFECTIVENESS FOR THE MOST ACCURATE SIMULATIONS FOR EACH OF THE SUBSCALE MODEL ICE SHAPES

[$C_{l,\max}$, maximum lift coefficient; α_{stall}, stalling angle; $\Delta C_{d,rms}$, root-mean-square percent difference in drag coefficient; α, angle of attack; k/c, ice roughness height per chord length.]

Ice shape		Simulation	Simulation $C_{l,\max}$ – casting $C_{l,\max}$	Simulation α_{stall} – casting α_{stall}, deg	$\Delta C_{d,rms}$, percent (linear α range)
Classification	Configuration				
Roughness	ED0762	50-percent k/c = 0.0026 roughness	–0.036 (–3.7 percent)	–1.02	15.5
Horn	ED0735	Two-dimensional smooth	0.001 (0.2 percent)	0.00	10.7
Streamwise	ED0730	Simple geometry with 80-percent k/c = 0.0009 roughness	0.013 (1.3 percent)	–0.02	4.8
Spanwise ridge	ED0760	Two-dimensional smooth	–0.023 (–2.4 percent)	–1.98	5.7

The performance data acquired in Phase III and summarized in Table 7 provide a measure of the aerodynamic uncertainty associated with quantifying the ice-accretion geometry and subsequent iced-airfoil performance. Since it is assumed that the three-dimensional casting configurations have no uncertainty in terms of ice-accretion geometry, the primary source of uncertainty in these data was the aerodynamic performance measurement. The data for the lower fidelity simulations also contain uncertainties because the accretion geometry was represented with less fidelity and there were uncertainties in the aerodynamic performance measurement. The data in Table 7 for the $C_{l,\max}$ comparison indicate that these values are an order of magnitude larger than the measurement uncertainty given in Table 2. In the case of stalling angle, there were significant effects of ice-accretion geometry uncertainty for roughness and spanwise-ridge ice, whereas for horn and streamwise ice, the simulation accuracy was similar to the measurement uncertainty. Visual inspection of the C_d versus α plots in Figure 8, Figure 9, Figure 11, and Figure 13 shows that the lower fidelity simulations that had good agreement with the casting had a corresponding $\Delta C_{d,rms}$ value that was about 10 percent or less. This was the case for all but the ED0762 roughness simulation in Table 7, which had a value of 15.5 percent. However, it was noted in the discussion of this case that better drag simulation could likely be achieved using different sizes of roughness on the upper and lower surfaces.

The combined results of the subscale-model aerodynamic simulation studies indicated that different simulation methods should be used to best represent the aerodynamics of the iced airfoil according to the different types of ice accretions based on the governing flow physics. This confirmed the ideas that were developed in Phase I.

- For ice roughness, good aerodynamic simulation was achieved using distributed grit roughness, but a combination of sizes may be needed to accurately simulate drag coefficient, in addition to maximum lift coefficient and stalling angle.
- For horn ice, the dominance of the separation bubble flowfield made the two-dimensional smooth and simple-geometry simulations nearly equal in effectiveness. The addition of roughness had little effect on the simulation fidelity. Better aerodynamic fidelity was achieved with three-dimensional simulations (see Busch et al. (Refs. 27, 28, and 38)), but these are complicated to build and require detailed ice measurements.
- For streamwise ice, roughness had to be added to two-dimensional simulations to obtain the best agreement in performance with the casting configuration. In this case, the size and concentration had significant effects such that these parameters should be taken into account. This was consistent with the effect of the roughness on the trailing-edge stall characteristics of the airfoil with the streamwise ice configurations.
- For spanwise-ridge ice, the performance effects were best reproduced by the two-dimensional smooth simulation. Attempts to improve the simulation fidelity were largely unsuccessful because of the inability to reproduce the three-dimensional flowfield features. In this case, the size and location of the upper surface ridge on the NACA 23012 model did not result in a large, closed, two-dimensional separation bubble. There was also evidence of trailing-edge separation. The combination of these effects complicated the ability to simulate the performance of the casting with lower fidelity geometries.

The aerodynamic data for the various levels of ice-shape simulation fidelity gathered in Phase III aided in confirming and further refining the ice-shape classifications described in Phase I. The data illustrate the range in performance data for typical simulation methods as applied to a subscale model. Establishing the relationship between simulation fidelity and the resulting aerodynamic performance was a key goal of this program. Accomplishing this goal for the subscale model led to increased understanding of the effects, which was applied directly to the full-scale model research phases. This is described in Phases IV and V.

6.0 Phase IV: Full-Scale-Model Ice-Accretion Testing

The objective of this phase was to obtain molds of ice accretions in each of the four ice classifications on a full-scale airfoil. In a scaling methods development effort such as this, it is important to have a set of benchmark data and firm knowledge of the full-scale phenomena. This information provides validation data for both the subscale testing and scaling methods developed. In order to gain full-scale aerodynamic effects information for the four types of ice, accurate representations of the ice needed to be obtained. Therefore, a full-scale ice accretion model was built and tested in the IRT. This effort provided the full-scale, reference ice shapes for the program.

The model built for this phase was again a two-dimensional, NACA 23012 that spanned the IRT test section from floor to ceiling. The model was machined from solid aluminum and had a removable leading edge section for making molds of the ice accretions. It had a chord length of 72 in. (1.83 m)—4 times that of the subscale model. Figure 15 shows a photograph of the model mounted vertically in the IRT. It was instrumented with pressure taps for alignment purposes and with thermocouples to monitor model temperature.

Test conditions for the full-scale icing tests were selected as indicated in the Phase II discussion: that is, icing conditions that a commuter aircraft might encounter in flight, as defined by Appendix C icing conditions, and that would yield ice accretions falling within the four ice classifications described in Phase I. Some adjustments in the test conditions were made because of limitations in the IRT operating envelope. To generate the spanwise-ridge ice accretion, an electric foil heater was attached to the removable leading edge, similar to the subscale-model testing (Phase II). Icing conditions and heater settings were adjusted such that water flowed downstream past the heated surface and then froze as a spanwise ridge on both the upper and lower surfaces of the model.

The full-scale ice accretions produced in the IRT were, as in the subscale testing, recorded using photographs, ice tracings, and ice-depth measurements. When a particular ice accretion was selected for the Phase V testing, the accretion run was repeated, and the removable leading edge and resulting ice accretion were detached from the model. The leading edge and ice were installed in a mold box, and the mold was poured. Molds were made of 10 ice accretions. There were three each of the horn and streamwise accretions and two each of the roughness and spanwise-ridge accretions. Castings were subsequently made from each of these molds. The castings were then prioritized according to which were the best representatives of the four ice classifications and then according to which were of most interest for forming a full-scale, high-fidelity, ice-contaminated aerodynamic validation database. A total of six ice shapes were selected for aerodynamic testing in Phase V, and the IRT test conditions are provided in Table 8. There were two each of the roughness and streamwise shapes and one each of the horn and spanwise-ridge shapes. These ice shapes and the resulting aerodynamic effects are described in the following section.

Figure 15.—Full-scale NACA 23012 ice-accretion model installed in NASA Icing Research Tunnel.

7.0 Phase V: Full-Scale-Model Aerodynamic Testing

In Phase V of the program, aerodynamic testing was conducted to establish a set of high-fidelity benchmark data useful for the development of simulation methods on the subscale model. The ice molds acquired in Phase IV were used to develop high-fidelity, ice-casting simulations for testing on a 72-in.- (1.83-m-) chord NACA 23012 model. This model was considered to be full-scale or near full-scale for the purposes of this research program. The aerodynamic performance

TABLE 8.—ICING CONDITIONS FOR FULL-SCALE ICING TESTS—ICE ACCRETIONS SELECTED FOR AERODYNAMIC TESTING IN PHASE V

[IRT, Icing Research Tunnel; α, angle of attack; MVD, median volume diameter; LWC, liquid water content.]

Ice-shape classification	IRT run	Airspeed, kn	α, deg	MVD, μm	LWC, g/m^3	Total temperature		Static temperature		Spray time, min
						ºF	ºC	ºF	ºC	
Horn	EG1164	175	5.0	20	0.85	28.0	–2.2	20.8	–6.2	11.3
Streamwise 1	EG1162	150	2.0	30	0.55	–8.0	–22.2	–13.5	–25.3	10.0
Roughness 1	EG1126	200	2.0	20	0.50	28.0	–2.2	18.6	–7.4	2.0
Spanwise ridge	EG1159	150	1.5	20	0.81	20.0	–6.7	14.8	–9.6	15.0
Streamwise 2	EG1125	200	2.0	15	0.30	4.0	–15.6	–5.3	–20.7	20.0
Roughness 2	EG1134	200	2.0	40	0.55	4.0	–15.6	–5.3	–20.7	2.0

testing was carried out at the Office National d'Etudes et Recherches Aérospatiales (ONERA) F1 pressurized wind tunnel to achieve near-flight Reynolds number. Only three-dimensional casting simulations were tested on the full-scale model in order to maximize the number of different ice accretions that could be investigated. The pressurized wind tunnel was also used to vary Re from 4.5×10^6 to 16.0×10^6 and M from 0.10 to 0.28 in order to determine the sensitivity of the aerodynamic performance to these parameters. The set of benchmark data acquired in this phase was then used extensively in Phase VI to complete the research program.

7.1 Ice Accretions Tested

The ice accretions that were acquired in Phase IV and selected for full-scale model aerodynamic testing are shown in Figure 16 to Figure 21. Six ice accretions were tested: one horn shape, one spanwise-ridge shape, two streamwise shapes, and two roughness shapes. Two each of the streamwise and roughness shapes were selected for full-scale testing because these were thought to be more challenging for aerodynamic subscale simulation. Therefore, it was decided that variations within these categories (i.e., streamwise ice and roughness) would be useful in quantifying the uncertainties associated with subscale simulations of these accretions.

The horn shape in Figure 16 shows the classic upper surface horn typical of this glaze-type accretion. The streamwise shape in Figure 17 is more conformal to the leading-edge radius, with a smooth zone on the nose followed by downstream rime feather roughness. The glaze roughness in Figure 18 had a smooth zone in the stagnation region followed by large roughness downstream. The spanwise-ridge shape in Figure 19 was formed by applying a heater mat to the model leading edge. The heat input and icing conditions were adjusted to accrete the upper and lower surface ridges shown in Figure 19. The streamwise shape in Figure 20 was selected for aerodynamic testing because it had a more "pointed" geometry at the leading edge and was less conformal to the surface than the other streamwise shape (Figure 17). The remaining roughness case in Figure 21 was formed in cold conditions, resulting in very fine rime feathers downstream of the smooth stagnation region that were very different in size and distribution from the glaze roughness case in Figure 18. Casting simulations were manufactured for aerodynamic testing from the molds of these accretions acquired in Phase IV of the program.

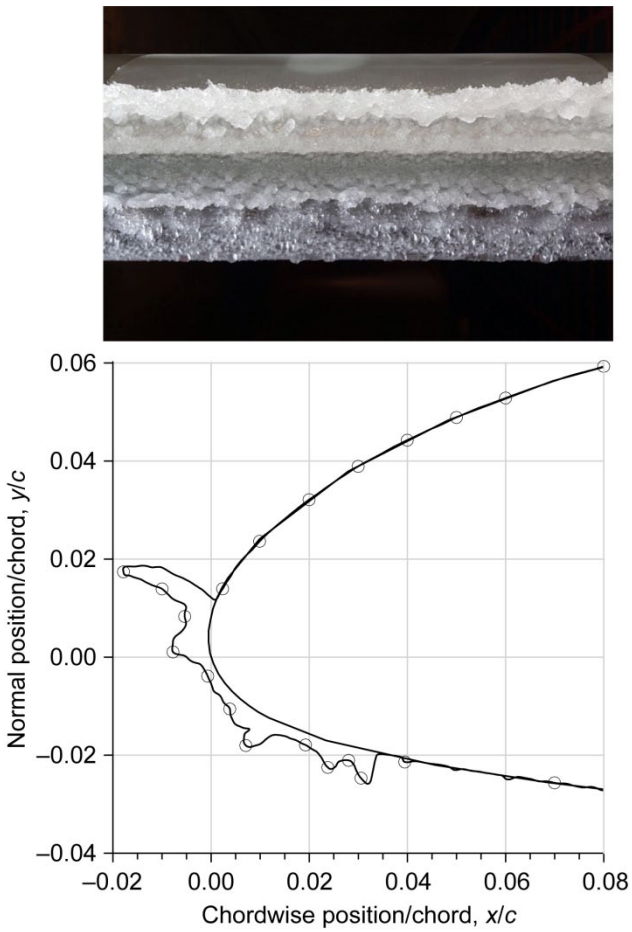

Figure 16.—Tracing and photograph of EG1164 horn ice shape. Tracing was taken from ice casting used for aerodynamic testing; pressure orifice locations are indicated by open circles.

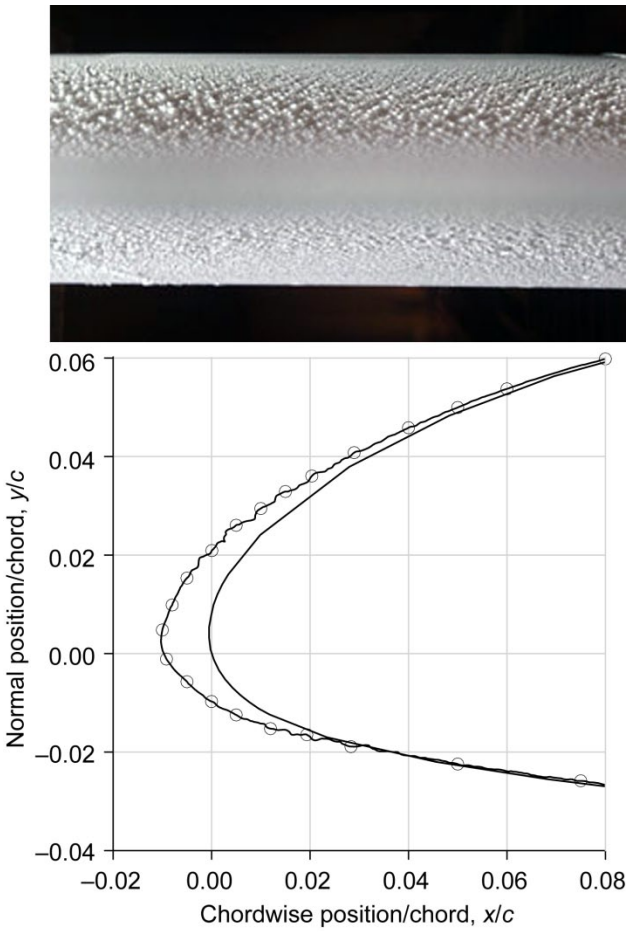

Figure 17.—Tracing and photograph of EG1162 streamwise ice shape 1. Tracing was taken from ice casting used for aerodynamic testing; pressure orifice locations are indicated by open circles.

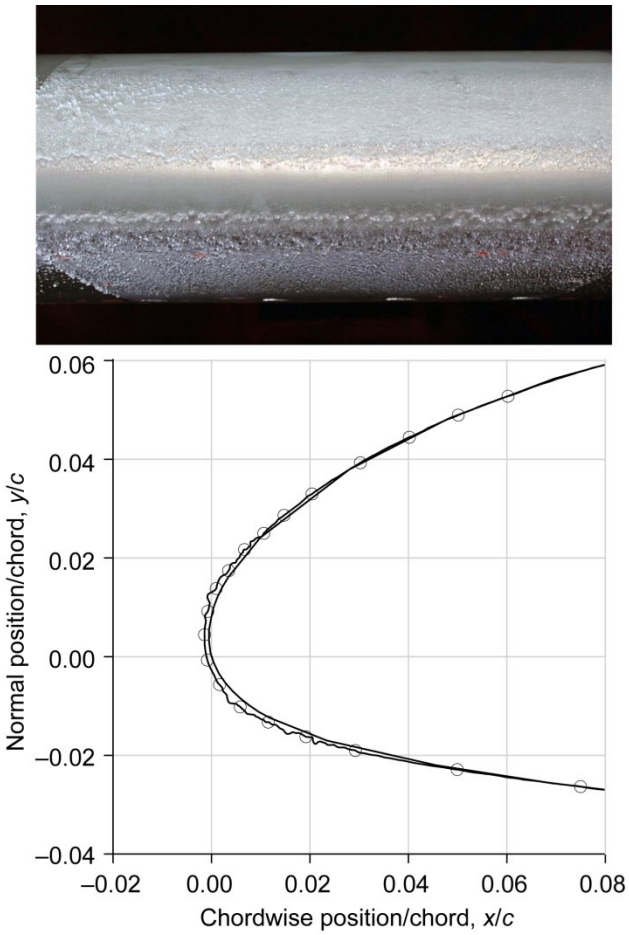

Figure 18.—Tracing and photograph of EG1126 roughness ice shape 1. Tracing was taken from ice casting used for aerodynamic testing; pressure orifice locations are indicated by open circles.

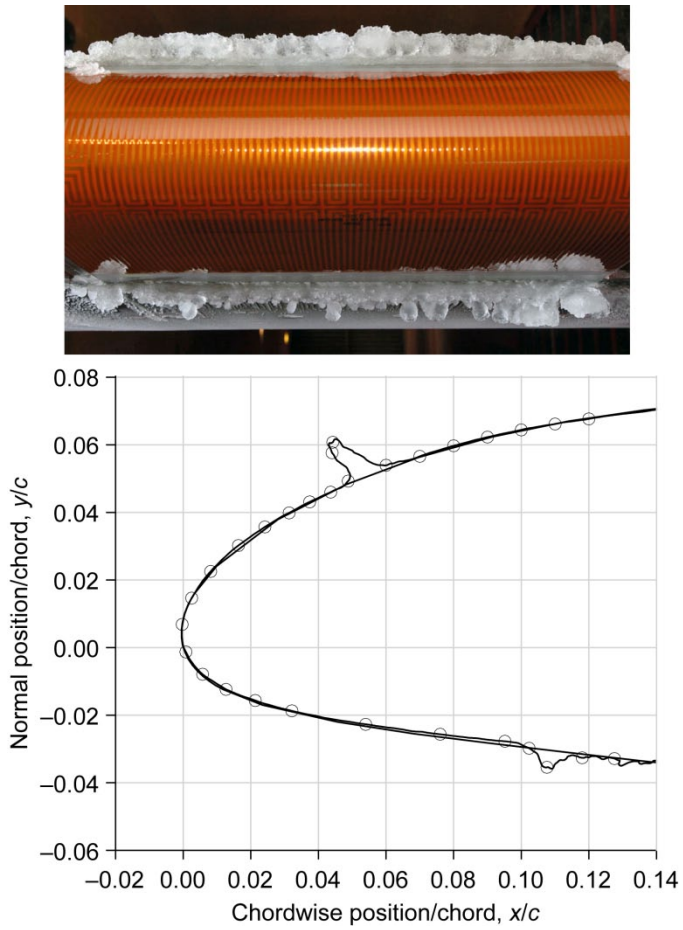

Figure 19.—Tracing and photograph of EG1159 spanwise-ridge ice shape. Tracing was taken from ice casting used for aerodynamic testing; pressure orifice locations are indicated by open circles.

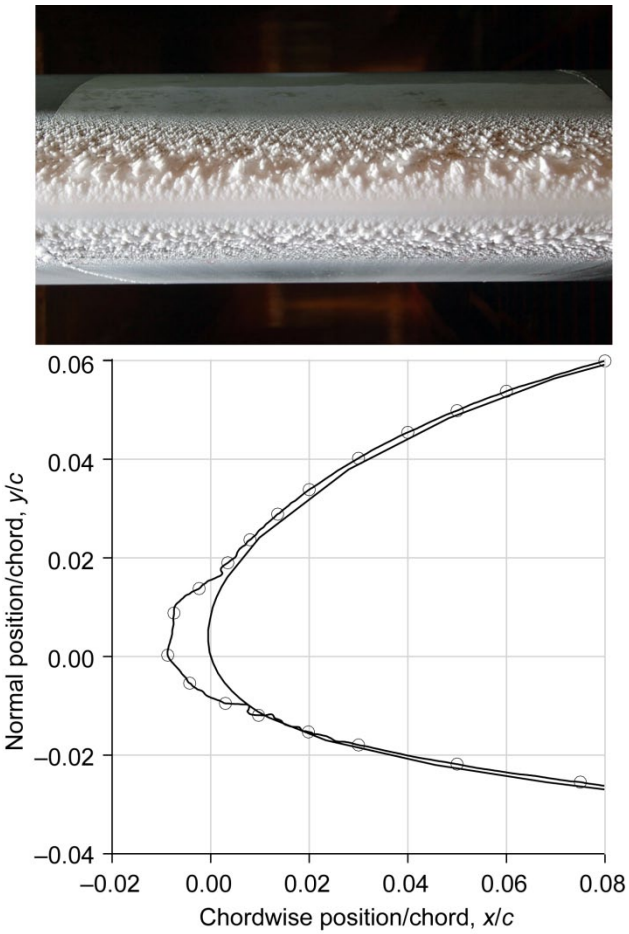

Figure 20.—Tracing and photograph of EG1125 streamwise ice shape 2. Tracing was taken from ice casting used for aerodynamic testing; pressure orifice locations are indicated by open circles.

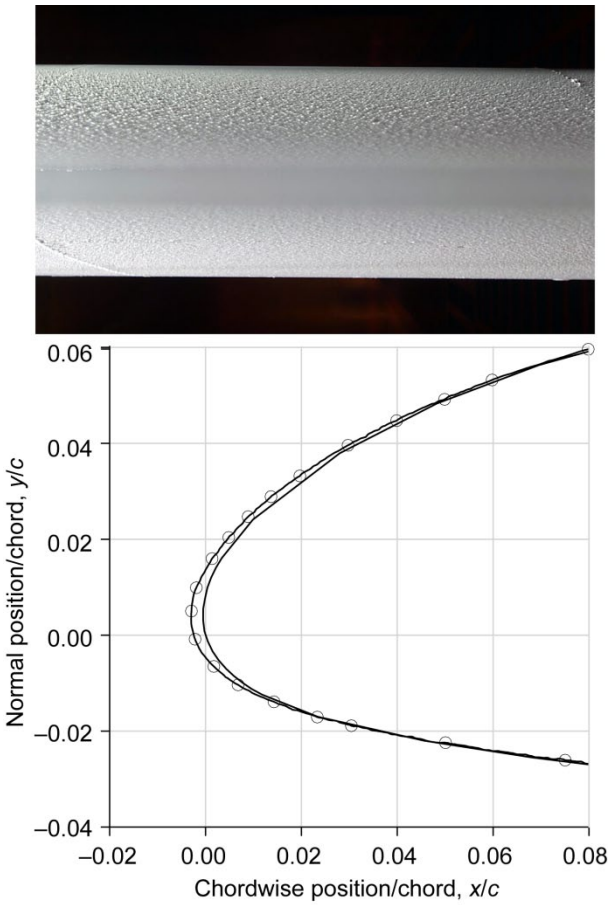

Figure 21.—Tracing and photograph of EG1134 roughness ice shape 2. Tracing was taken from ice casting used for aerodynamic testing; pressure orifice locations are indicated by open circles.

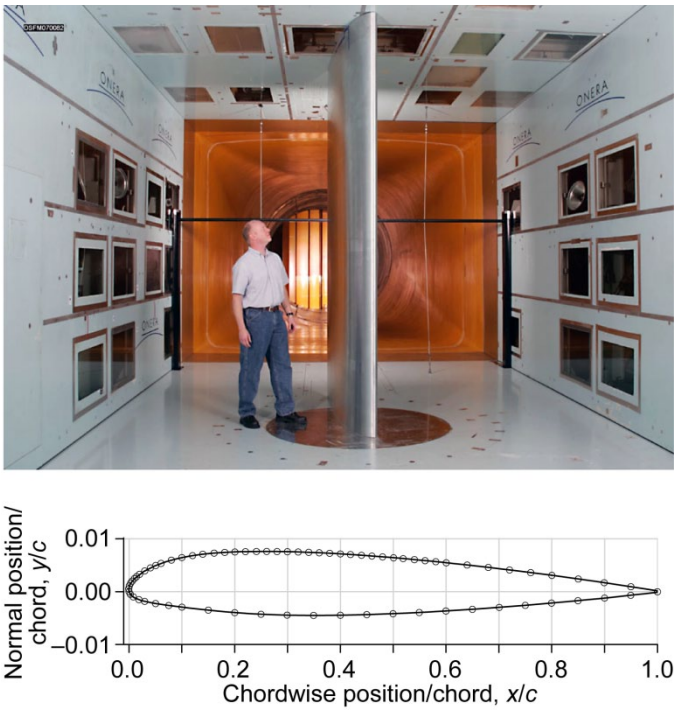

Figure 22.—Photograph of the full-scale NACA 23012 airfoil model installed in Office National d'Etudes et Recherches Aérospatiales (ONERA) F1 wind-tunnel test section and model pressure tap layout.

7.2 Experimental Methods

All of the aerodynamic testing in Phase V was performed at the ONERA F1 full-scale, pressurized wind-tunnel facility (Ref. 48). The closed-return wind tunnel has a test-section measuring 138 in. (3.5 m) high by 177 in. (4.5 m) wide by 433 in. (11.0 m) long. The maximum test section Mach number is 0.36, and the maximum stagnation pressure is 57 psia (3.85 bar). The unit Reynolds number can be varied to a maximum of $Re = 6.0\times10^6$/ft at M = 0.23. Total temperature is maintained via a heat exchanger located in the second diffuser downstream of the fan. The fan operates at constant speed while the test section Mach number is controlled by adjusting the pitch of the blades. The test-section inlet flow is conditioned through a 7.18-to-1 contraction containing a honeycomb flow straightener and three turbulence-reduction screens.

The 72-in.- (1.83-m-) chord NACA 23012 airfoil model was mounted vertically in the test section as shown in Figure 22. The model had a span of 137.5 in. (3.49 m) and was mounted in the floor force balance. Small gaps between the bottom of the model and the test-section floor as well as the top of the model and the test-section ceiling were maintained so as not to cause mechanical hysteresis in the force-balance measurements. The model had a main chordwise row of 72 pressure taps located at 43-percent span measured from the test-section floor. In addition, there was a row of 20 taps oriented spanwise at $x/c = 0.70$ on the upper surface. The model was designed and built with full-span removable, interchangeable leading-edge sections. The baseline leading edge had the clean NACA 23012 profile, whereas the alternate leading edge had a truncated nose geometry. The latter design facilitated mounting of the various ice-shape casting simulations. Accommodations were also made in the pressure tapping to allow for rapid connection of pressure instrumentation in the cast ice shapes. Also shown in Figure 22 is the wake rake located one chord length downstream of the model trailing edge. The wake rake had 100 stagnation pressure probes spaced 0.79 in. (20 mm) apart and was located at a fixed spanwise station at 57-percent span above the test-section floor.

Data acquisition runs were performed in angle-of-attack sweeps for increasing and then decreasing angle of attack at a constant sweep rate of 0.1°/sec. In addition, data were acquired at a fixed angle of attack for selected angles over the range of the sweep, and repeat runs were performed to ensure data precision. The data shown in this report are for increasing angle-of-attack sweeps that were averaged to the nearest 0.5°

in postprocessing. The averaging method divided the data into 0.5° bins and averaged the results. For example, data from $\alpha = 2.75°$ to 3.25° were averaged to create a data point close to $\alpha = 3.0°$. The actual angle of attack was the arithmetic mean of the angles of attack collected in that bin. During the sweeps, data were acquired from analog transducers for the force balance and tunnel conditions. The model-surface, test-section sidewall, and wake-rake pressures were acquired using an electronically scanned pressure system. The acquisition of these data was synchronized in time corresponding to the angle-of-attack sweep rate.

Lift and pitching-moment coefficients were calculated from the force balance and from the integration of the surface-pressure measurements. Good agreement between the integrated-pressure data and the force-balance data was obtained. In this report, the lift and pitching moment data reported for the clean configuration were obtained from the surface pressures, whereas the data reported for the iced configurations were obtained from the force balance. The force-balance data are reported because, in many cases, the stall of the iced-airfoil configurations was characterized by unsteady flow. The available signal conditioning for the force-balance data allowed for more effective filtering of these unsteady effects. The drag coefficient was calculated from the wake pressures using standard momentum-deficit methods, and these values are reported in this paper for all configurations. The performance coefficients provided in this report were corrected for wind-tunnel wall effects using the methods of Allen and Vincenti (Ref. 42). Moëns (Ref. 49) performed more detailed analysis of the tunnel wall effects. The angle-of-attack sweeps were performed for a large range of Reynolds numbers and Mach numbers as shown in Table 9. The matrix was designed to isolate the independent effects of these parameters. Therefore, Reynolds number variations were performed at constant M = 0.10 and 0.20, and a Mach number variation was performed at a constant nominal $Re = 12\times10^6$. Because of operational constraints, the Reynolds number was not maintained exactly constant for each of these conditions, and therefore Table 9 indicates the variation over the course of the entire test campaign.

TABLE 9.—MATRIX OF REYNOLDS AND MACH NUMBER CONDITIONS FOR FULL-SCALE AERODYNAMIC TESTING

Reynolds number range	Mach number		
	0.10	0.20	0.28
4.5×10^6 to 4.6×10^6	X		
8.0×10^6 to 9.1×10^6	X	X	
12.0×10^6 to 12.3×10^6	X	X	X
15.8×10^6 to 16.0×10^6		X	

The experimental uncertainty in the performance coefficients was estimated using the methods of Kline and McClintock (Ref. 50) and of Coleman and Steele (Ref. 51) for 20:1 odds. Table 10 lists these uncertainties for both integrated-pressure and force-balance measurements. The values were calculated for the clean model configuration at $Re = 9.1\times10^6$ and M = 0.20. These values were analyzed before the wall corrections were applied. The absolute uncertainties in Table 10 are inversely proportional to the dynamic pressure (except angle of attack). This condition was selected because it corresponds to the average dynamic pressure over the range of conditions (Table 9). Therefore, Reynolds and Mach number combinations having lower dynamic pressure would have slightly larger uncertainties, whereas combinations with higher dynamic pressure would have slightly lower uncertainties. All of these uncertainties were acceptable for the purposes of this investigation. The relative uncertainties in pitching moment (both pressure and balance) seem large for this example because of the small reference value. For cases where the pitching moments were larger—for example, in the iced-airfoil case—the absolute uncertainty would be similar, therefore resulting in a lower relative uncertainty. This was also the case for the uncertainty in drag coefficient. Several repeat runs were performed for both clean and iced configurations, and these run-to-run variations in the coefficients were much smaller than the uncertainties listed in Table 9. The good agreement between the integrated-pressure and force-balance data provided further assurances of data quality.

TABLE 10.—ESTIMATED EXPERIMENTAL UNCERTAINTIES FOR AERODYNAMIC DATA FROM FULL-SCALE MODEL TESTING IN ONERA F1 WIND TUNNEL

Aerodynamic quantity	Reference value	Absolute uncertainty	Relative uncertainty, percent
Angle of attack, α	8.01°	±0.02°	±0.25
Lift coefficient, C_l balance	1.095	±0.010	±0.93
Pitching moment coefficient, C_m balance	–0.0144	±0.00071	±4.9
Pressure coefficient, C_p	–1.057	±0.015	±1.4
Lift coefficient, C_l pressure	1.096	±0.0070	±0.64
Pitching moment coefficient, C_m pressure	–0.0148	±0.0024	±16.5
Drag coefficient, C_d wake	0.0086	±0.00048	±5.5

Flow visualization also was performed during the test campaign. Fluorescent minitufts made from 5-lb test nylon monofilament having a diameter of 0.006 in. (0.15 mm) were applied to the top portion of the model span on both the upper and lower surfaces. The tufts were illuminated with ultraviolet black light, and the motion was video recorded during all of the data-acquisition runs. Surface-oil flow visualization was also performed for selected cases. These runs were performed at atmospheric pressure and M = 0.20, and the corresponding nominal Re was 8×10^6. CassouDeSalle and Gilliot (Ref. 52) and CassouDeSalle et al. (Ref. 53) provide more information about the experimental arrangement and procedures.

For each ice accretion, a set of casting simulations was fabricated for aerodynamic testing. The castings were made from a hard, two-part polyurethane-type material of the very low viscosity needed for it to flow into the intricate details of the ice molds. The moldings of the ice accretions were limited to a span of 15 in. (0.38 m) at the center of the IRT model. This was of sufficient length to reproduce the spanwise variation in all of the ice-accretion geometries. Therefore, multiple sections of casting were fabricated for each ice shape to cover the 137.48-in. (3.49-m) span of the NACA 23012 model. A total of 10 sections were used, each having a finished length of 13.75 in. (0.349 m). The sections were bolted onto the alternate leading edge of the model, and the interfaces were sealed with silicone. Figure 23 shows a completed installation. One casting section was instrumented with surface pressure taps. This was located at the same spanwise station as the main chordwise row on the model (43-percent span measured from the test-section floor). The orifices were drilled directly into the casting and were located in areas where previous research had indicated they would be conducive to good surface pressure measurements (Refs. 36 and 41). The number of pressure taps on the entire removable section ranged from 29 to 36 with some ice shapes requiring higher resolution. The tracings of Figure 16 to Figure 21 indicate the locations of the pressure orifices. These tracings were obtained from the casting of the ice shape instead of from the tunnel ice accretion.

Figure 23.—Completed installation of EG1164 horn ice-shape casting sections on the leading edge of the NACA 23012 airfoil model (upper surface view).

7.3 Results and Discussion

7.3.1 Clean- Versus Iced-Airfoil Aerodynamics

The NACA 23012 airfoil model was tested in the baseline configuration to establish the clean performance over the given range of Reynolds and Mach numbers. Extensive validation of the clean airfoil performance was performed against archival and computational data. Broeren et al. (Refs. 54 and 55) provide detailed discussion of the clean model validation that yielded a high degree of confidence in these measurements. Of primary interest in this program was the effect of the ice shapes on the airfoil performance. This is also covered in detail in Broeren et al. (Refs. 54 and 55), from which the following discussion was taken.

The ice-casting simulations applied to the NACA 23012 airfoil caused a large range of detrimental performance effects because of the differences in the ice-accretion geometries and roughness levels. Figure 24 illustrates the general range in performance degradation for four of the six artificial ice shapes at $\mathrm{Re} = 15.9\times10^6$ and M = 0.20. For this Reynolds and Mach number condition, the clean airfoil $C_{l,\max}$ was 1.85 and α_{stall} was 18.1°. The EG1162 streamwise and EG1126 roughness shapes had a very similar effect on lift, drag, and pitching moment. The effect of the EG1162 ice simulation was to reduce $C_{l,\max}$ to 1.16 and α_{stall} to 11.9°. The EG1126 roughness shape caused a slightly larger lift penalty, yielding $C_{l,\max} = 1.09$ at $\alpha_{stall} = 11.4°$. Both of these ice shapes caused a significant redistribution of surface pressure resulting in an increase in the pitching-moment slope. The stall characteristics and surface pressure distribution indicated that there was likely some boundary-layer separation on the aft portions of the airfoil. The plot of drag coefficient shows that the EG1162 and EG1126 shapes also had a similar effect, with the former having a slightly higher C_d up to $\alpha \approx 8.5°$, where there was a crossover. At higher angles of attack, the EG1162 streamwise ice shape caused a lower drag coefficient in comparison to the EG1126 shape, which was consistent with the higher lift coefficients.

The performance results with the streamwise (EG1162) and roughness (EG1126) shapes sharply contrast the effect of the horn (EG1164) and spanwise-ridge (EG1159) shapes. The size and location of the latter two ice shapes on the airfoil caused large upper surface separation bubbles that significantly altered

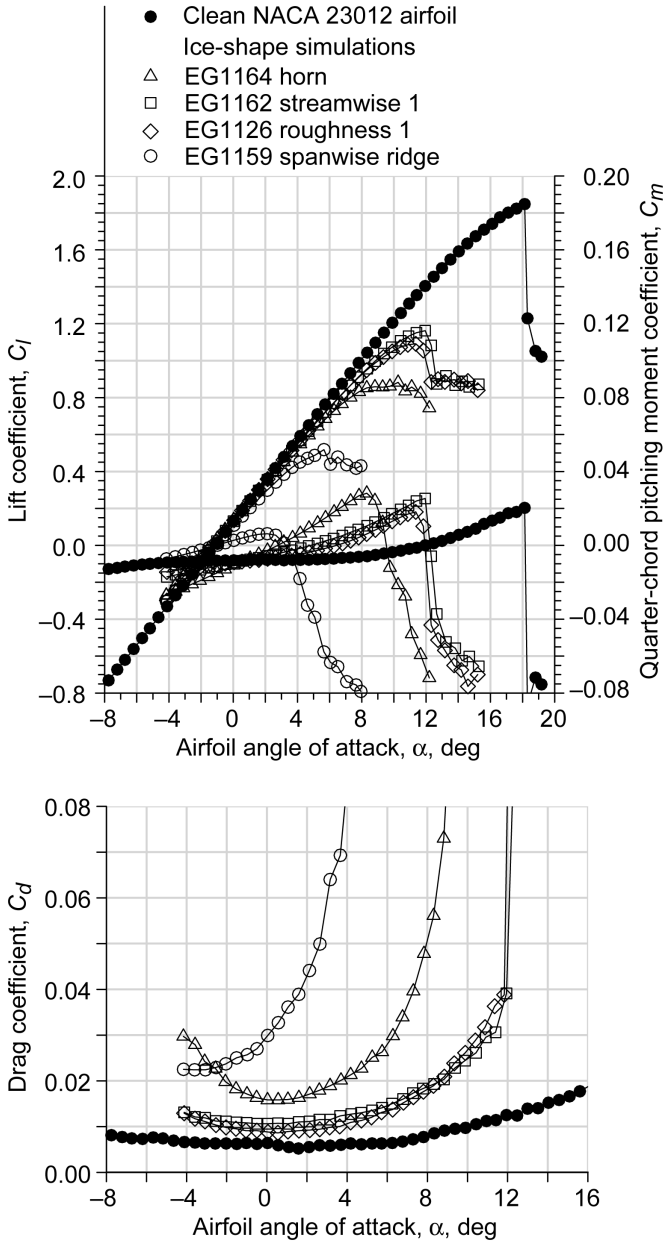

Figure 24.—Comparison of performance effects of simulated ice configurations on the NACA 23012 airfoil at a Reynolds number of 15.9×10^6 and a Mach number of 0.20.

the flowfield and the subsequent performance. The resulting $C_{l,\max}$ for the EG1164 horn shape was 0.86 at $\alpha_{stall} = 8.8°$, which amounted to a 54-percent reduction in $C_{l,\max}$ from the clean airfoil at this Reynolds and Mach number condition. The effect of the EG1159 spanwise-ridge shape was even more severe with $C_{l,\max} = 0.52$ at $\alpha_{stall} = 5.6°$. The plot of drag coefficient in Figure 24 further illustrates the significant impact of the separation bubble for the EG1164 and EG1159 ice-shape simulations. It is interesting to note that C_d for the EG1159 spanwise ridge is lower than C_d for the EG1164 horn shape for $\alpha < \sim -2.5°$. This most likely occurred because, at low angles of attack, drag coefficient is affected primarily by ice accretion on the airfoil lower surface (Refs. 46 and 47). A comparison of Figure 16 and Figure 19 clearly shows that, for the horn shape, the ice accretion on the lower surface was higher and extended farther, albeit it was closer to the leading edge. This effect of lower and upper surface ice accretion on drag is described by Bragg et al. (Ref. 23) and in much more detail by Kim (Ref. 46). For $\alpha > -2.5°$, C_d for the spanwise-ridge shape was much larger, which was consistent with the lower $C_{l,\max}$. The fact that the spanwise-ridge ice simulation resulted in the largest performance degradation was likely due to the location of the upper surface ridge. As depicted in Figure 16 and Figure 19, the horn height was larger than the upper surface ridge, but the ridge was located at $x/c \approx 0.06$. Lee and Bragg (Ref. 31) showed that, for the NACA 23012 airfoil, the most sensitive location for ice accretion (of this size) in terms of loss in maximum lift was downstream of the leading edge and upstream of the maximum adverse pressure gradient for the clean airfoil. This is also illustrated in Figure 24 for the streamwise shape that formed on the airfoil leading edge, since the performance penalty was not nearly as severe as for the spanwise ridge.

Figure 25 further illustrates the effect of leading-edge ice accretion on the NACA 23012 airfoil performance. These data are for the EG1125 and EG1134 streamwise and roughness ice shapes compared with the streamwise and roughness shapes plotted in Figure 24. Of these, it is interesting to note that the lowest iced-airfoil $C_{l,\max}$ occurred with the EG1126 roughness shape. The drag penalty was also largest for this shape for $\alpha > 9°$. Note that there is a scale change between Figure 24 and Figure 25 in the C_d versus α plot to facilitate the comparisons. The fact that the two streamwise ice simulations (EG1162 and EG1125) had a nearly identical effect on $C_{l,\max}$ and C_d (for $\alpha > 9°$) as did the EG1126 roughness shape reveals an important characteristic about leading-edge ice accretion on the NACA 23012 section. A comparison of the ice-accretion characteristics in Figure 17, Figure 18, and Figure 20 and icing environment in Table 8, shows a wide range of icing conditions and resulting sizes and shapes. The obvious implication is that the basic ice height or thickness for these types of accretions is not a strong driver of the stall performance behavior. A similar effect has been observed in previous testing of a subscale

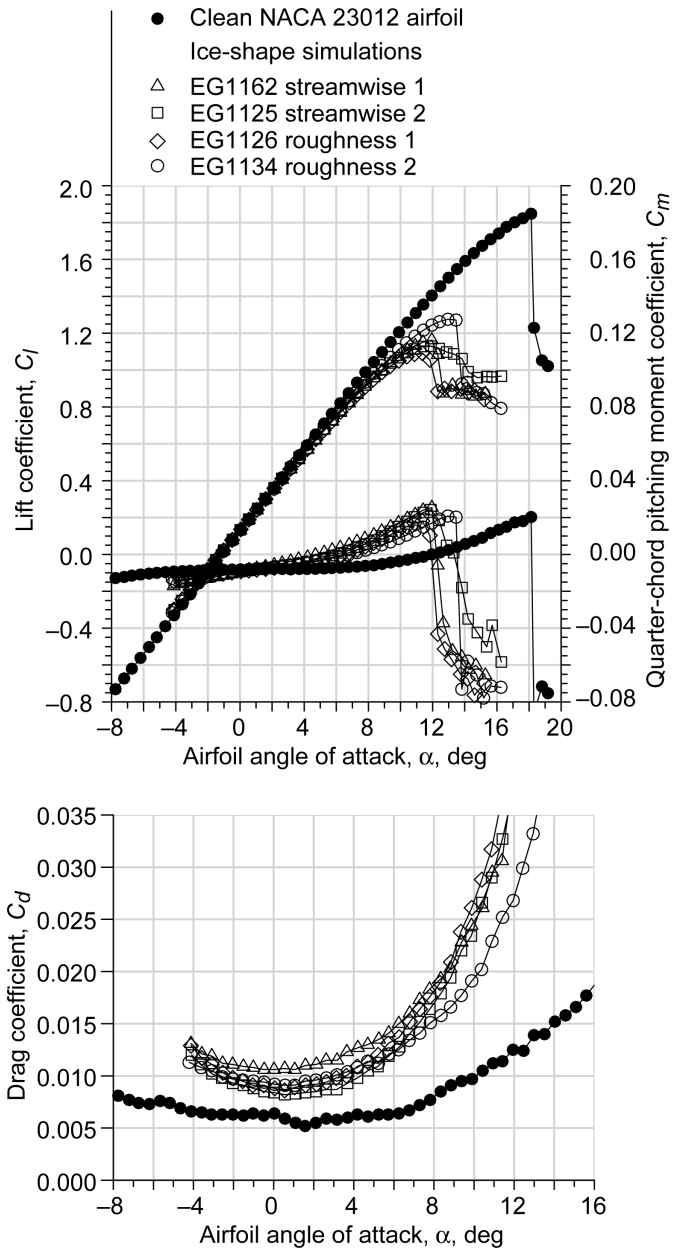

Figure 25.—Comparison of performance effects of roughness and streamwise ice simulations on the NACA 23012 airfoil at a Reynolds number of 15.9×10^6 and a Mach number of 0.20.

NACA 23012 airfoil with larger geometric quarter-round ice simulations located at the leading edge (i.e., $x/c = y/c = 0$). Lee and Bragg (Ref. 31) showed that the iced-airfoil $C_{l,\max}$ only varied from about 1.01 to 0.97 as the ice height (or thickness) varied from $k/c = 0.006$ to 0.014. A similar $C_{l,\max}$ range was observed in Figure 25: 1.09 for the EG1126 simulation to 1.16 for the EG1162 simulation. Despite the similarity in the maximum lift coefficients, there is a difference in the stalling characteristics, with the EG1162 and EG1126 simulations having a sharper stall and the EG1125 simulation resulting in a more gradual stall. This implies that significant flowfield differences remain among the various artificial ice shapes despite the alignment of the maximum lift coefficient. These effects are addressed further later in this section.

The data for the EG1134 simulation illustrate the smallest maximum lift penalty measured for the given set of artificial ice shapes. The $C_{l,\max}$ of 1.28 was about 10 percent higher than for the other three ice simulations in Figure 25. The drag coefficient on the interval $-1.5° < \alpha < 4.7°$ was slightly higher than, but most similar to, the drag coefficient for the other roughness simulation, EG1126. It is interesting that the lift performance of the NACA 23012 section with the EG1134 simulation was very similar to that of the 80-grit sandpaper ($k/c = 0.00023$) reported by Broeren et al. (Ref. 10) on the 36-in. chord model of the same airfoil. For that case, $C_{l,\max}$ was about 1.30 at $\mathrm{Re} = 7.5\times10^6$ and $\mathrm{M} = 0.21$. The minimum C_d for the airfoil with the 80-grit sandpaper was 0.010, about 10 percent higher than for the EG1134 roughness simulation in the present data. The comparison of the EG1134 performance effects to the 80-grit sandpaper on the 36-in.-chord model is useful because the latter is roughly equivalent to 40-grit sandpaper on a full-scale wing, which is often used in aircraft certification flight testing applications (Ref. 35).

The trends in the drag coefficient variation with angle of attack for the iced-airfoil configurations in Figure 25 may be interpreted in terms of the icing environment from which these simulations were obtained. For example, in the case of the two streamwise ice simulations, C_d for the EG1162 configuration was higher than that for the EG1125 configuration in the range $-4° \le \alpha \le 8°$. This is somewhat surprising given that the EG1162 ice shape was more conformal to the airfoil leading edge than the EG1125 ice shape was. However, the EG1162 ice shape was accreted with a larger MVD drop size and, therefore, the downstream roughness covered a larger surface extent. This may be at least partially responsible for the larger drag over this range. It was noted in the preceding paragraph that the drag coefficient for the EG1134 roughness configuration was slightly higher than for the EG1126 roughness configuration over the interval $-1.5° < \alpha < 4.7°$. This may have occurred because the rime roughness EG1134 was accreted with a larger MVD drop size resulting in the ice roughness covering a larger surface extent.

For $\alpha > 4.7°$, it is likely that a larger extent of trailing-edge separation developed for the EG1126 configuration, thus the

drag coefficient grew larger than for the EG1134 configuration corresponding to the lower stalling angle.

Since an accurate subscale ice-accretion simulation relies on appropriately representing the key flowfield features contributing to the aerodynamics, it was important to understand these features and the stalling characteristics, in particular. Because detailed flowfield measurements were not performed, this analysis relies primarily on interpretation of surface pressure distributions, flow visualizations and past research.

Figure 26 compares the surface pressure distributions at a matched angle of attack for each of the configurations shown in Figure 24. These are divided into two plots for clarity. In the upper plot, it is noteworthy that the iced-airfoil pressure distributions for the streamwise and roughness configurations do not differ significantly from the clean data. Consistent with the definitions provided in Phase I, the performance effects are chiefly manifest through the boundary layer with minimal flow separation. This explains, in part, the small increase in drag from the clean configuration for this angle of attack. This situation is clearly in contrast to the lower plot, which compares the horn and spanwise-ridge shapes.

For these cases, there was a large deviation from the clean data owing to the large extent of separated flow. For the EG1164 configuration, the flow separated near the tip of the horn, resulting in a region of nearly constant pressure from $x/c = -0.02$ to 0.03 on the upper surface. There was significant pressure recovery downstream of $x/c = 0.03$, but the pressure coefficient did not approach that of the clean airfoil until $x/c = 0.20$. For the EG1159 configuration, the separated flow region was much larger, as indicated by the region of nearly constant pressure from $x/c = 0.04$ to 0.30 on the upper surface. This region was followed by a very gradual pressure recovery. The pressure data for this case also reveal the effect of the lower surface ridge, which also had a small separation bubble associated with it. The large extent of separated flow for the EG1159 configuration is consistent with the large degradation in the performance coefficients in Figure 24. The surface-oil flow visualization performed at this angle of attack indicated a time-averaged separation-bubble reattachment zone from $x/c = 0.64$ to 0.68. As discussed in Phase I, the separation bubble associated with horn and spanwise-ridge shapes is known to have large-scale unsteady characteristics. Time-averaged flow information can be very useful, but it must be interpreted carefully.

The stalling characteristics of the iced-airfoil configurations tested in this study are of key interest because in a subscale simulation it is important to maintain the stalling characteristics in addition to any one parameter such as the maximum lift coefficient or stalling angle. The development of airfoil stall classifications relates back to the early research of B. Melvill Jones (Ref. 56), among others. McCullough and Gault (Ref. 43) built upon the foundations of this early work and conducted a systematic series of airfoil section tests to establish the commonly accepted stall-type definitions in use today.

Trailing-edge stall is preceded by movement of the turbulent boundary-layer separation point forward from the trailing edge with increasing angle of attack.

Leading-edge stall has abrupt flow separation near the leading edge generally without subsequent reattachment. The abrupt separation usually results from the bursting of a small laminar separation bubble that results in a sharp decrease in lift.

Thin-airfoil stall is preceded by flow separation at the leading edge with reattachment (a laminar separation bubble) at a point that moves progressively downstream with increasing angle of attack.

Stall type is a function of several variables such as Reynolds number, surface roughness, or free-stream turbulence. Therefore, any particular airfoil may exhibit a combination of stall types, or its stall type may change over various flow regimes or conditions.

Over the range of Reynolds and Mach numbers in this study, the clean NACA 23012 airfoil clearly exhibited the leading-edge stall type. The abrupt flow separation at stall was evident from the flow visualization and pressure distributions and was manifested in the sharp drop in lift coefficient. Both Haines (Ref. 57) and Tani (Ref. 58) conducted extensive reviews of airfoil stall research and noted that the abrupt flow separation associated with leading-edge stall can result from either the bursting of a small laminar separation bubble (as reported by McCullough and Gault (Ref. 43)) or from reseparation of the turbulent boundary layer downstream of the bubble reattachment location. Haines (Ref. 57) makes the case that the latter separation mechanism is probably more likely for moderate- to high-Reynolds-number flows. So the bursting of the laminar separation bubble is not a necessary prerequisite for leading-edge stall. In either case, there is no question about the basic stall type of the clean NACA 23012 section.

The application of the simulated ice shapes to the NACA 23012 airfoil section alters the stall type in some cases. It is clear that the main stall mechanism for the EG1164 horn and EG1159 spanwise-ridge shapes was the growth (with angle of attack) of a large upper surface separation bubble. Thus, an airfoil with these ice shapes would be classified as having the thin-airfoil stall type. This conclusion is based on lift performance data in Figure 24 and is corroborated by the corresponding pressure distributions and flow visualization. These flowfield physics are fairly well documented (Refs. 22 and 23). However, the stalling characteristics of the streamwise and roughness ice simulations on the NACA 23012 airfoil are not as well understood and were investigated further.

What is of primary interest here is that for three of the four roughness and streamwise ice simulations tested on the NACA 23012 airfoil, the presence of the simulated ice did not appear to significantly alter the leading-edge stall type. This observation

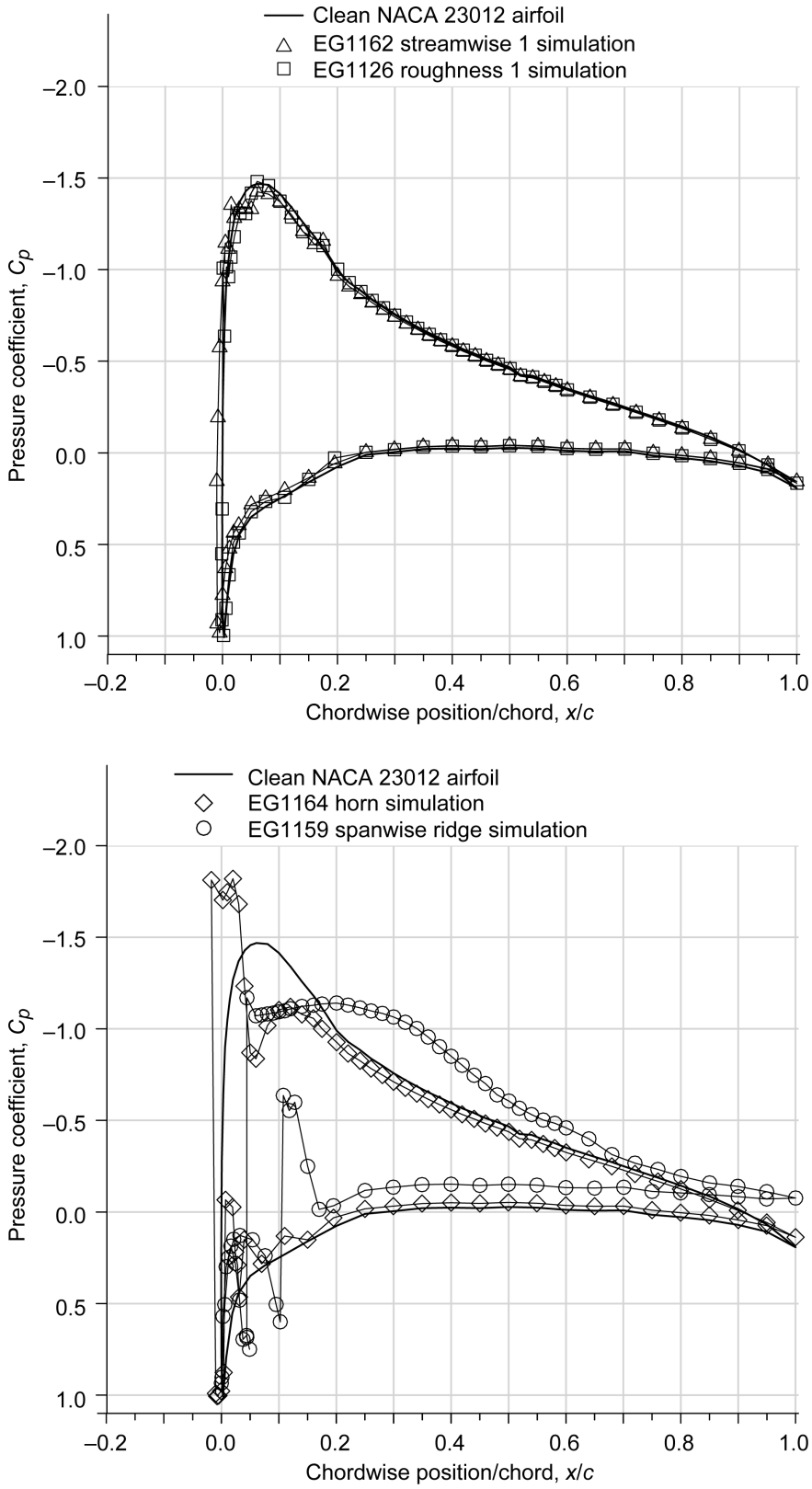

Figure 26.—Comparison of clean and iced NACA 23012 airfoil pressure distribution for various high-fidelity, ice-casting simulations at an angle of attack of 4.2°, a Reynolds number of 15.9×10^6, and a Mach number of 0.20.

is based on the abrupt loss in lift at stall for the EG1162, EG1126, and EG1134 configurations (see Figure 25). Only the EG1125 configuration resulted in a more gradual loss of lift poststall. Analysis of the pressure distributions and flow visualizations by Broeren et al. (Refs. 54 and 55) for the EG1125 configuration showed that there was likely a small leading-edge separation bubble that altered the pressure distribution from the clean case such that the tendency to leading-edge stall was altered. In fact, the EG1125 configuration could be classified as having trailing-edge stall, since lift was reduced because the turbulent boundary-layer separation moved forward as angle of attack increased. Although a small separation bubble was present because of the ice shape, this bubble did not grow significantly in chordwise extent leading up to the stall. This partly explains the classification of this ice shape as streamwise ice, according to the descriptions in Phase I. This behavior is contrasted with the EG1164 and EG1159 configurations that had the thin-airfoil stall type. The stall mechanism for the EG1125 configuration was very different from that for the EG1164 and EG1159 configurations even though they shared a more gradual decrease in lift at stall. This is consistent with the characteristics of thin-airfoil and trailing-edge stall as defined by McCullough and Gault (Ref. 43). The fact that the leading-edge stall characteristics of the NACA 23012 airfoil were not significantly altered by the presence of one streamwise and two roughness ice shapes is important for subscale simulations and computational modeling. As mentioned in this discussion, leading-edge stall is defined as abrupt flow separation near the leading edge of the airfoil without subsequent reattachment. With the ice shapes in question, there were likely small areas of boundary-layer separation present on the scale of the ice roughness. Research reported by Kerho and Bragg (Ref. 59) showed that leading-edge roughness can lead to a "transitional" boundary layer instead of acting as a "trip" with energetic transition to turbulence. The transition process due to ice-type roughness develops over a large part of the airfoil chord, up to 30 to 50 percent in some cases. The present data indicate that the transitional nature of the boundary layer was still susceptible to abrupt separation for the three ice simulations. In contrast, the larger size of the other ice shapes caused larger scale separation and alteration of the transition process as well as of the pressure distribution, thus leading to an alteration of the stall type.

7.3.2 Reynolds and Mach Number Effects

The pressurization capability of the F1 facility was fully exploited for the independent exploration of Reynolds and Mach number effects on the airfoil performance. The performance results for the clean NACA 23012 followed classic airfoil behavior. This is illustrated in Figure 27, which shows the effect on performance of increasing Re from 4.6×10^6 to 12.3×10^6 at constant M = 0.10. For these conditions, the lift data show that $C_{l,\max}$ increased from 1.76 to 1.88 with commensurate increases in α_{stall}. The variation of C_m with α

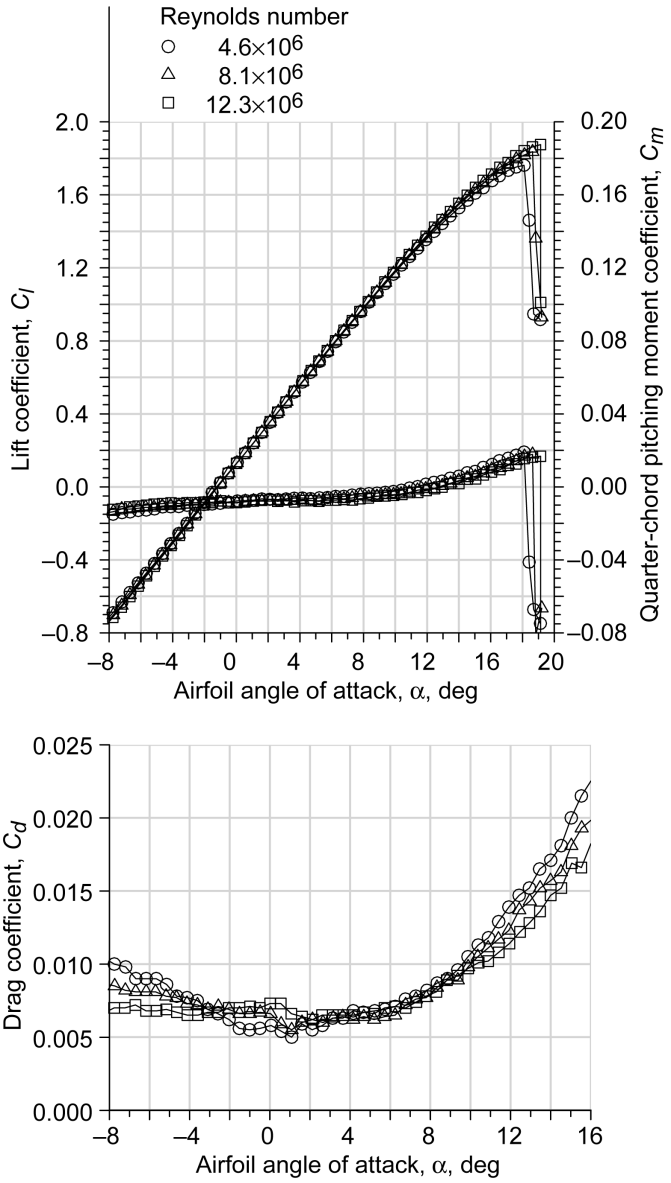

Figure 27.—Effect of Reynolds number at constant Mach 0.10 on the performance of the clean NACA 23012 airfoil.

also decreased slightly with increasing Re. The variation in drag coefficient with Reynolds number for $\alpha < 3°$ and $\alpha > 10°$ also followed historical trends for the NACA 23012 airfoil, with C_d decreasing with increasing Re (Ref. 60). The data for $3° \le \alpha \le 10°$ are more difficult to interpret. The uncertainty in C_d for these cases was higher than that reported in Table 10 because the dynamic pressure was lower for the data at M = 0.10. This illustrates a significant challenge with performing drag measurements in a pressurized wind tunnel because of the large range in dynamic pressure. However, highly accurate measurement of drag coefficient on the clean airfoil at low dynamic pressure was not a chief objective of this work. Reynolds number effects were also investigated over the range of $Re = 9.1\times10^6$ to 15.9×10^6 at constant M = 0.20. These data (Figure 28) show that there was very little variation in the airfoil performance over this Reynolds number range. Here the drag coefficient data are more well behaved thanks, in part, to the larger dynamic pressures associated with the conditions in Figure 28.

The effects of compressibility were also documented for the clean NACA 23012 airfoil section by varying M from 0.10 to 0.28 at a constant $Re = 12.1\times10^6$, and these data are given in Figure 29. Classic airfoil behavior was observed in the characteristic increases in the lift-curve slope and pitching-moment slope just before stall for increasing Mach number. Here $C_{l,\max}$ and α_{stall} both decreased with increasing Mach number as expected: $C_{l,\max}$ was 1.88 at M = 0.10 versus 1.78 at M = 0.28, and α_{stall} was reduced from 19.1° to 17.2°. Comparisons in drag coefficient were again more challenging to discern; however, there was the expected increase in C_d with increasing M for $\alpha > 10°$. These data are analyzed in more detail by Broeren et al. (Refs. 54 and 55), and the overall trends compare favorably with Haines's (Ref. 57) review of scale and Reynolds number effects on airfoil stalling characteristics.

Similar comparison plots were generated for each of the ice-shape configurations. The effect of Reynolds number variation at constant M = 0.10 is shown in Figure 30 for the EG1162 streamwise shape. In contrast to the clean airfoil, the lift and pitching moment data remained virtually unchanged despite a nearly three-fold increase in Re from 4.5×10^6 to 12.1×10^6. Note that the scales on the plots were changed to better illustrate any Reynolds number effects. Over this range of Reynolds number, $C_{l,\max}$ and α_{stall} were unchanged. The drag data show slightly more dependence, with the drag coefficient generally decreasing with increasing Reynolds number. The reason for this trend was not investigated in detail, but this effect on drag has been observed in other iced-airfoil studies (Refs. 10 and 11). Here, the absolute uncertainty in C_d was larger than that given in Table 10 as described in Section 7.2 for M = 0.10, but since the overall values of C_d were increased from the clean data, the relative uncertainties would be lower. Since there was very little or no variation in

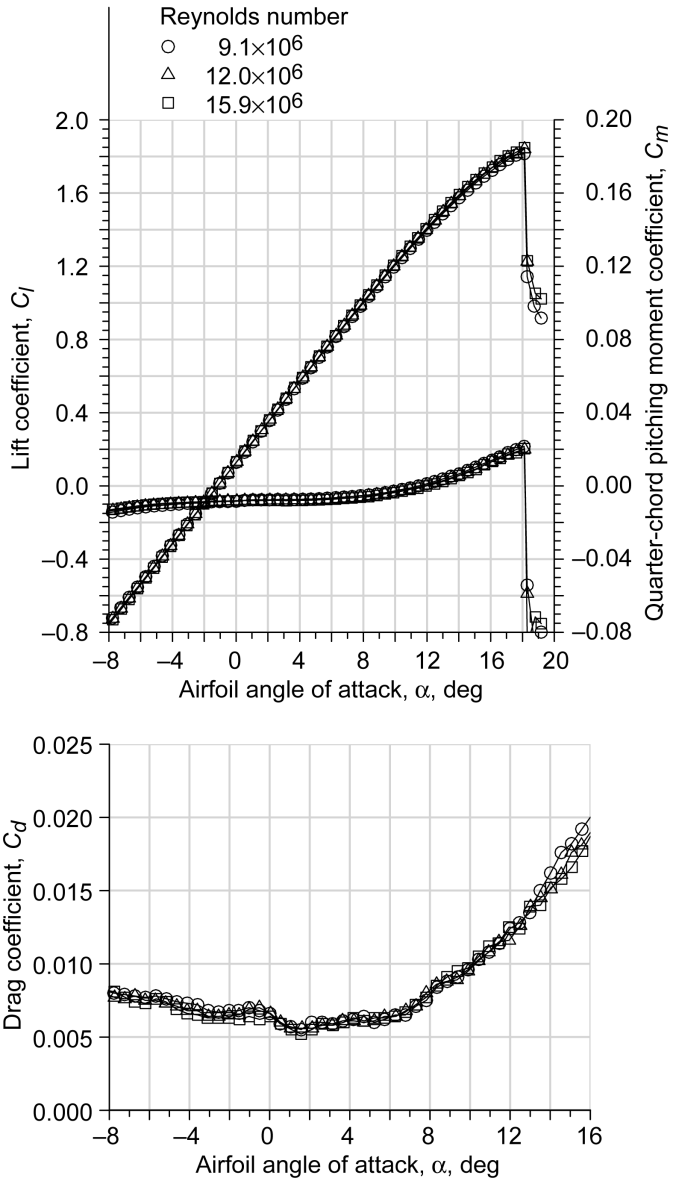

Figure 28.—Effect of Reynolds number at constant Mach 0.20 on the performance of the clean NACA 23012 airfoil.

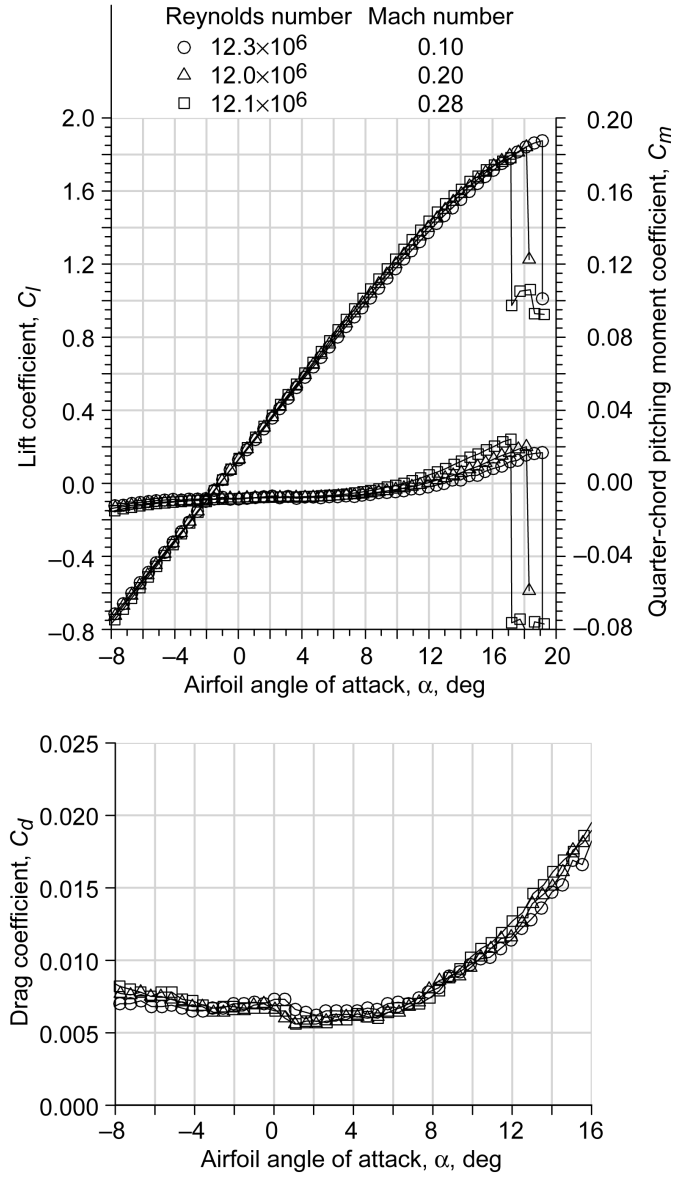

Figure 29.—Effect of Mach number at an approximately constant Reynolds number of 12.1×10^6 on the performance of the clean NACA 23012 airfoil.

the airfoil performance with the EG1162 ice shape from $Re = 4.5\times10^6$ to 12.1×10^6, it was expected that further increases in Reynolds number would continue to show no dependence on that parameter. This was, in fact, true as shown in Figure 31 for $Re = 9.0\times10^6$ to 15.9×10^6 at $M = 0.20$. As for the clean data, drag coefficient was well behaved mostly because of the larger dynamic pressures associated with the conditions in Figure 31. These data also indicate that the Reynolds number dependence of iced-airfoil drag coefficient decreased significantly for $Re > 9.0\times10^6$.

Figure 32 shows the effect of compressibility on iced-airfoil performance for the EG1162 configuration with $0.10 \le M \le 0.28$ at $Re = 12.1\times10^6$. The overall effects were similar to that described for the clean NACA 23012 airfoil, but the magnitudes of the effects were reduced. The effect of Mach number on maximum lift was similar among all of the iced-airfoil configurations and is described in more detail later in this section.

The data shown here for the EG1162 configuration are representative of all of the ice simulations tested in this study. This is particularly true for the lift and pitching moment variations with Reynolds number, even for the small roughness shapes. Changes in Reynolds number over this range did not substantially change the character of the stall either. That is, iced configurations with an abrupt, leading-edge stall character maintained this over the Reynolds number range. The effect on maximum lift coefficient for all of the simulations tested is summarized in Figure 33. Here, the clean NACA 23012 airfoil $C_{l,\max}$ showed more variation with Reynolds number than did the iced-airfoil configurations as expected from the previous discussion. Broeren et al. (Ref. 54) provide further comparison of NACA 23012 $C_{l,\max}$ variation along with data from other airfoils down to $Re = 2.0\times10^6$. That data showed that airfoil $C_{l,\max}$ was much more dependent on $Re < 4.5\times10^6$, the lower limit in this study, with Reynolds number independence being achieved for most (clean) airfoils at approximately $Re = 6.0\times10^6$ (Refs. 19 and 57). For the iced-airfoil configurations in this study, the noneffect of Reynolds number was consistent with the previous data compiled by Broeren et al. (Ref. 54). However, that data showed some Reynolds number dependence from $Re = 2.0\times10^6$ to 3.5×10^6 for certain ice shapes. It is also known from other work (e.g., Lee et al. (Ref. 61)) that drag coefficient (in the iced configuration) can depend on Reynolds number much more strongly for $Re < 2.0\times10^6$. Bragg et al. (Ref. 23) argue that the presence of ice contamination on the airfoil governs the boundary-layer behavior such that the influence of Reynolds number is reduced to lower order effects unlike the clean case. The present data continue to support this conclusion.

Mach number performance sweeps conducted for the other iced-airfoil configurations yielded similar results to those for the EG1162 configuration shown in Figure 32. The effect of Mach number on maximum lift coefficient is summarized in Figure 34 for all of the ice shapes tested in this study.

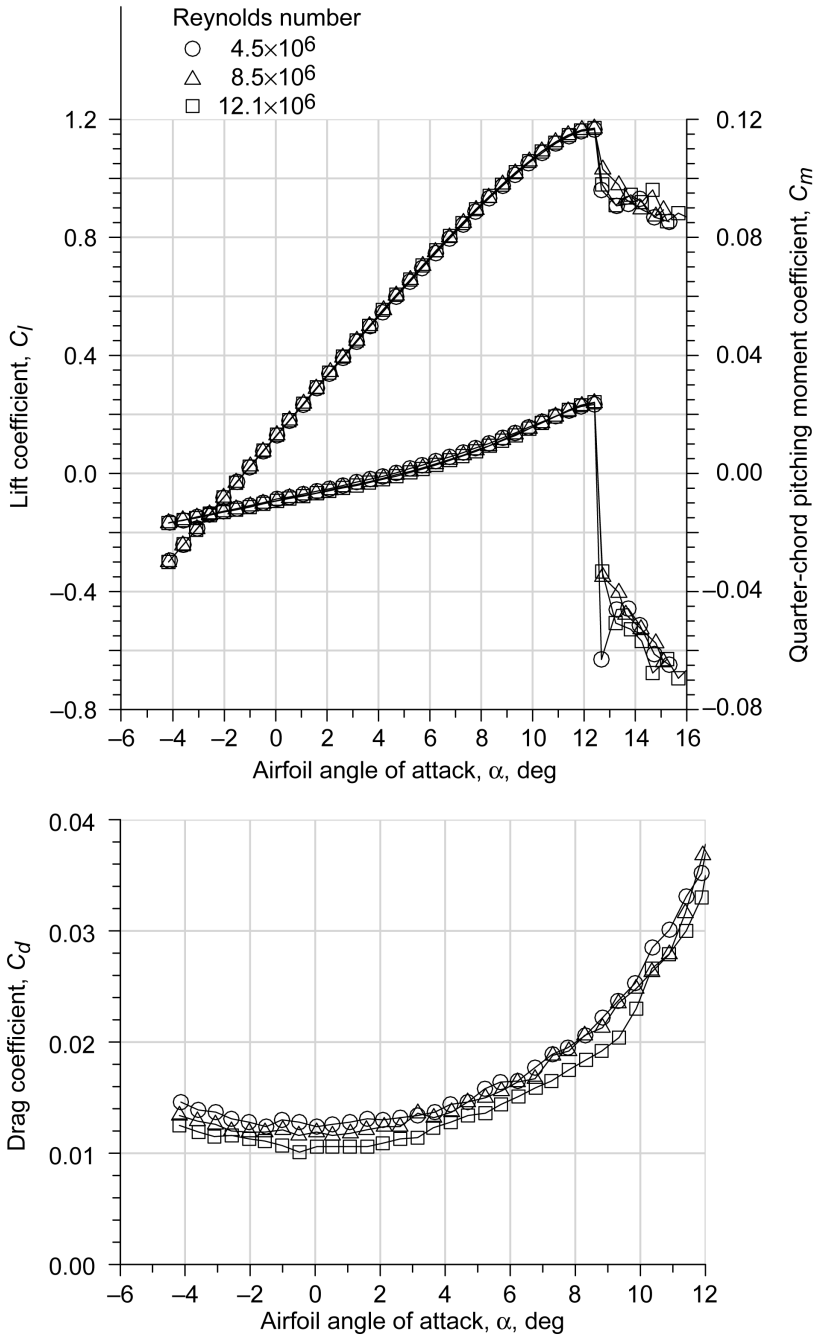

Figure 30.—Effect of Reynolds number at constant Mach 0.10 on the performance of the NACA 23012 airfoil with the EG1162 streamwise ice shape.

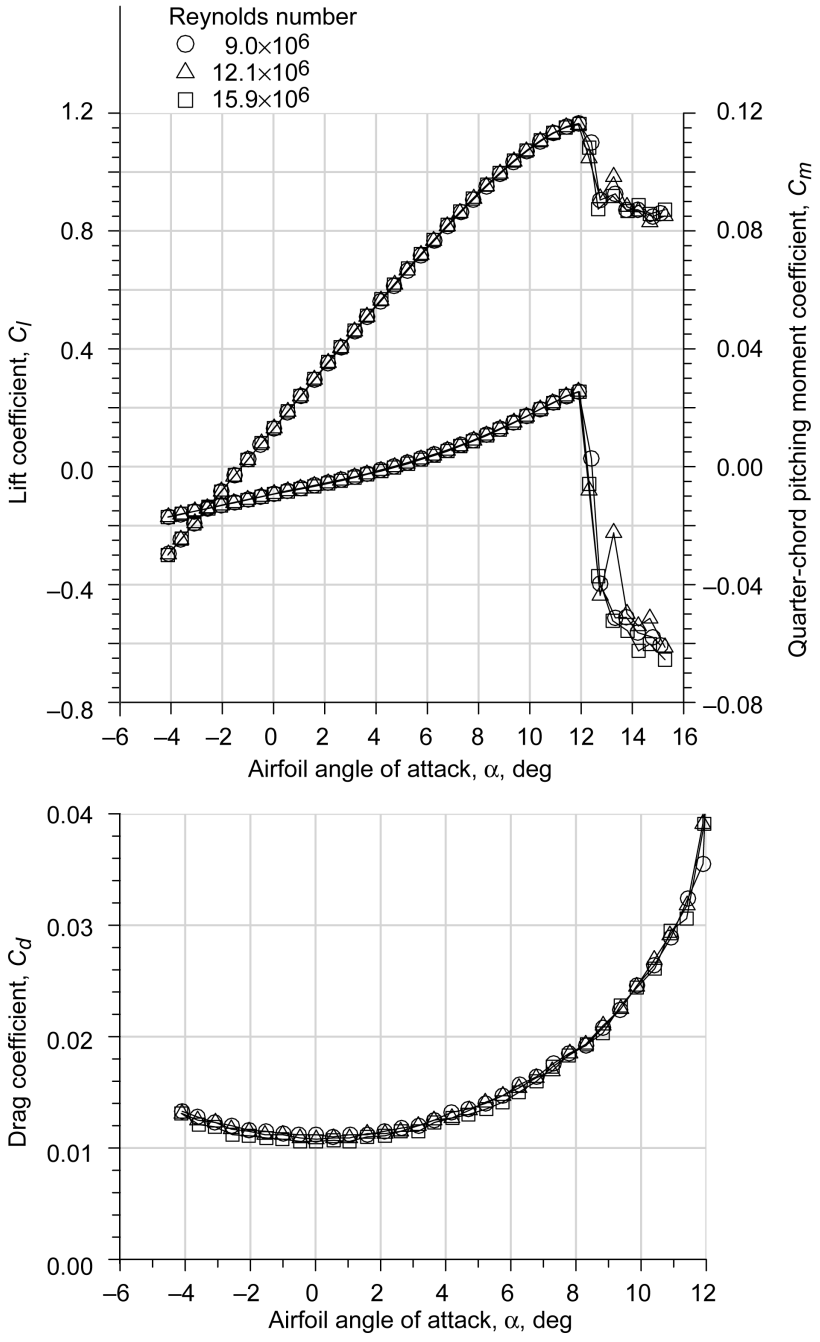

Figure 31.—Effect of Reynolds number at constant Mach 0.20 on the performance of the NACA 23012 airfoil with the EG1162 streamwise ice shape.

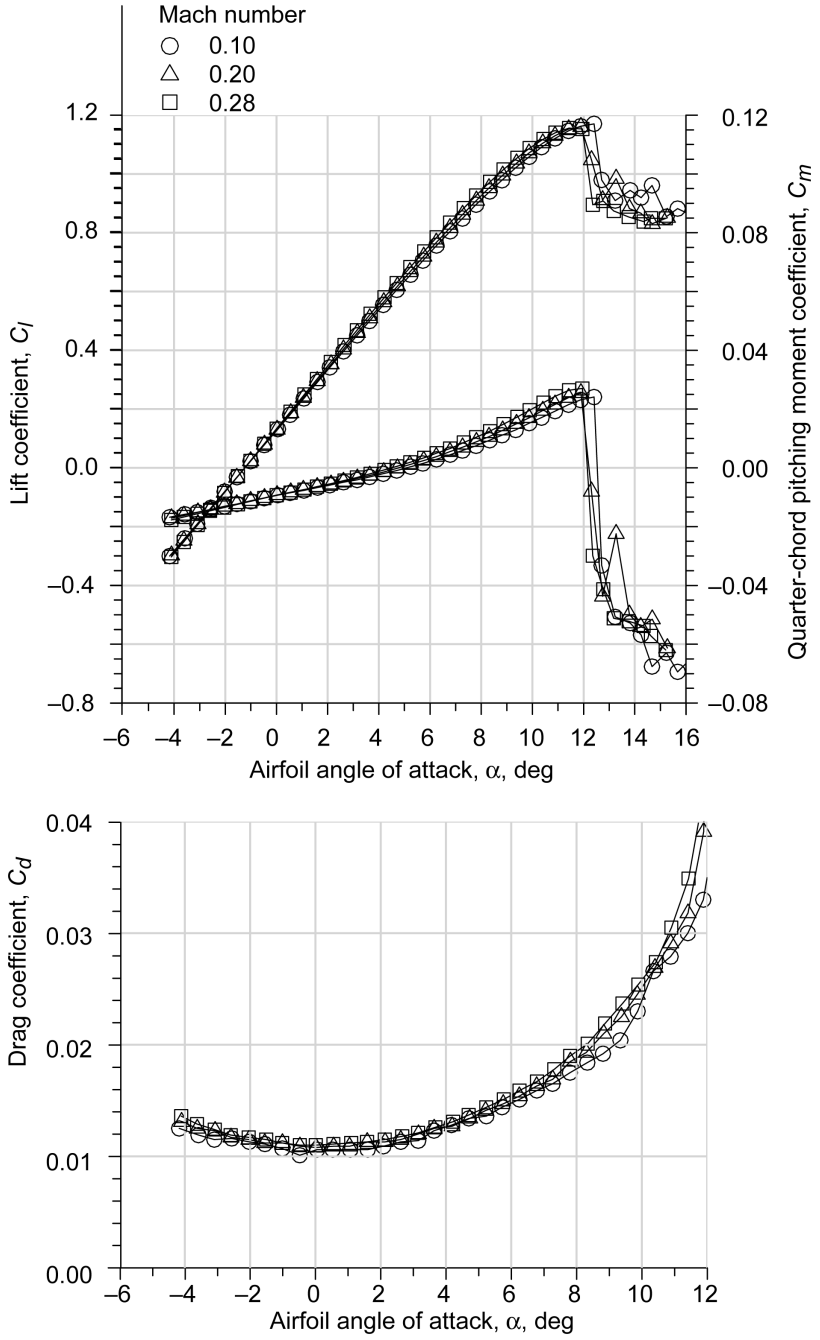

Figure 32.—Effect of Mach number at constant Reynolds number of 12.1×10^6 on the performance of the NACA 23012 airfoil with the EG1162 streamwise ice shape.

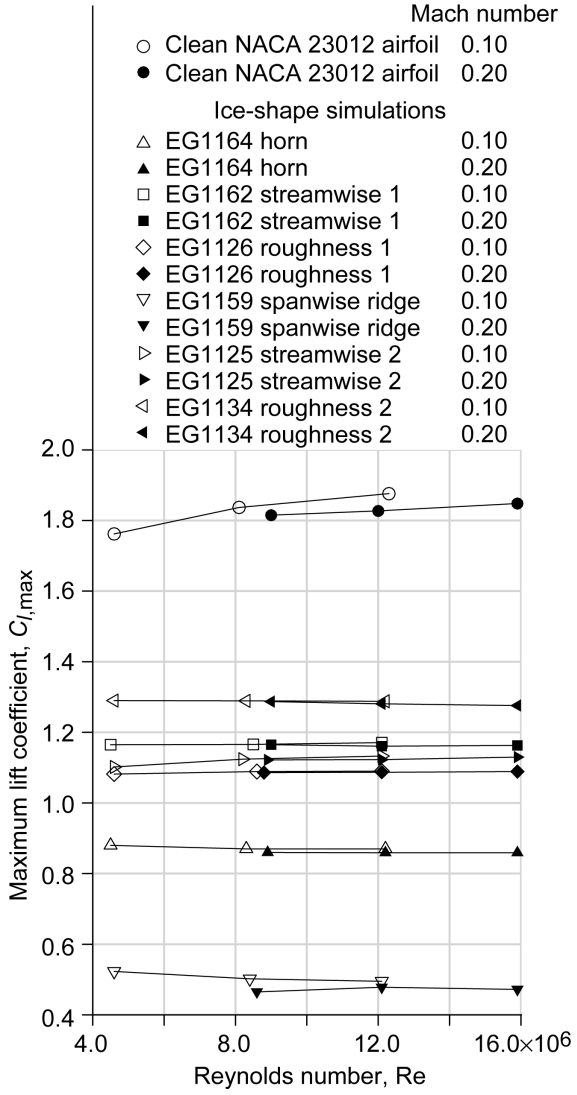

Figure 33.—Effect of Reynolds number on maximum lift coefficient for the clean NACA 23012 airfoil and for an airfoil with simulated ice shapes.

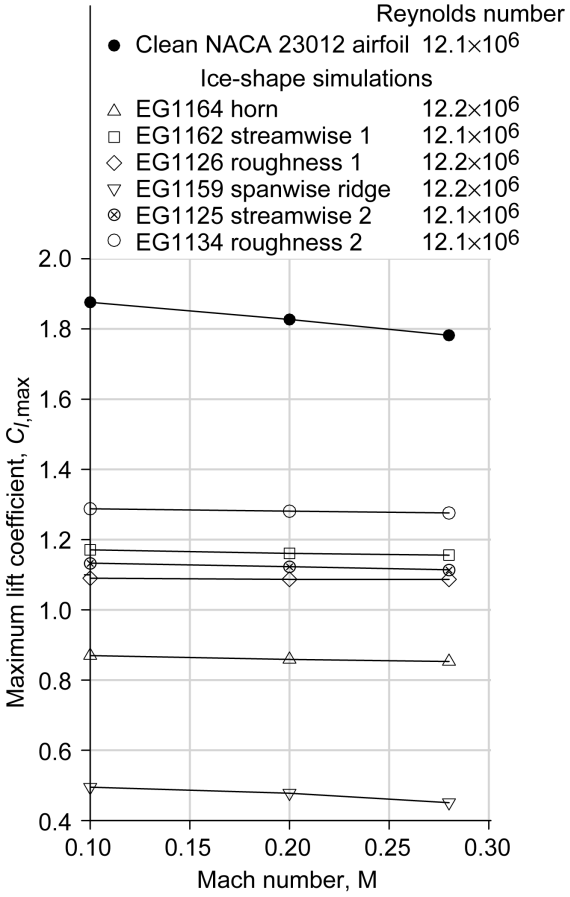

Figure 34.—Effect of Mach number on maximum lift coefficient for the clean NACA 23012 airfoil and for an airfoil with simulated ice shapes.

For the clean NACA 23012 airfoil, $C_{l,\max}$ showed the most significant dependence on Mach number over the range tested. For the iced-airfoil configurations, the horn shape (EG1164) and the spanwise-ridge shape (EG1159) exhibited the most significant decrease in $C_{l,\max}$ over this range, with the smaller ice shapes having much less dependence of $C_{l,\max}$ on Mach number. This trend involving smaller ice simulations and Mach number effects on maximum lift coefficient has been observed in other studies. For example, Broeren et al. (Ref. 10) report data for two sandpaper roughness configurations and four intercycle ice configurations on the NACA 23012 section. For the two sandpaper roughnesses, there was a very slight decrease in $C_{l,\max}$ for one case and an increase in $C_{l,\max}$ for the other case over $0.12 \le M \le 0.28$. In contrast, the much larger, ridge-type intercycle ice configurations resulted in $C_{l,\max}$ variations with Mach number similar to that shown in Figure 34 for the EG1164 and EG1159 simulations. Addy and Chung (Ref. 15) performed Mach number sensitivity testing for three-dimensional cast-ice simulations on an NLF–0414 airfoil section. The $C_{l,\max}$ variation for the smaller, 6-minute ice-accretion simulation showed significantly less sensitivity to Mach number for $0.12 \le M \le 0.29$ than did the larger, 22.5-minute ice-accretion simulation. The decrease in $C_{l,\max}$ with increasing Mach number for larger ice shapes appears to be related to an increase in the size of the separated flow region and is described in more detail by Bragg et al. (Ref. 23) and Broeren et al. (Ref. 30). Broeren et al. (Ref. 54) provide more detailed comparisons to other iced-airfoil data.

8.0 Phase VI: Simulation Validation Testing

The full-scale model aerodynamic testing described in Phase V provided a substantial validation data set for the final phase of this program. In Phase VI, the three-dimensional ice castings used in the full-scale test were represented with scaled, lower fidelity simulations for testing on the subscale model using the University of Illinois low-speed facility described in Phase III. These results provide full-scale to subscale comparisons of iced-airfoil aerodynamics under tightly controlled conditions and effectively "close the loop" by quantifying the accuracy of two-dimensional and simple-geometry simulations for subscale iced-airfoil aerodynamic testing at low Reynolds numbers. The comparisons of the subscale results to the full-scale validation database show the accuracy to which the iced-airfoil aerodynamics can be simulated on a subscale model at a low Reynolds number. This takes into account the previously described uncertainties associated with the ice-accretion geometry and Reynolds and Mach number effects. The comprehensive Phase VI results are reported in two papers by Busch et al. (Refs. 20 and 44) and in the dissertation by Busch (Ref. 62). The key results are summarized here.

8.1 Experimental and Ice-Shape Simulation Methods

The experimental facility and NACA 23012 model described in Phase III were utilized again in Phase VI. All aspects relative to the experimental methodology remained the same, except that that the ice-shape simulations were based on the three-dimensional castings described in Phase IV and V. Busch et al. (Refs. 20, 44, and 62) used two-dimensional smooth and simple-geometry shapes with and without added roughness to simulate the three-dimensional casting geometry on the subscale model. The two-dimensional smooth simulations were based on a pencil tracing of the three-dimensional castings with no further smoothing. This cross-sectional geometry was extruded across the span of the subscale model. Stereolithography was used to fabricate shapes that included pressure taps. The simple-geometry simulations were fabricated with off-the-shelf materials that were attached to the clean, baseline airfoil geometry. The grit roughness used to simulate the ice roughness consisted of various sizes of silicon carbide and aluminum oxide grains and glass microbeads. Depending on the ice shape being simulated, double-sided adhesive vinyl film was used to apply grains or microbeads to the two-dimensional smooth, simple-geometry shapes or to the airfoil surface. Details of the lower fidelity simulations for each of the iced-airfoil configurations are given in the following section.

8.2 Results and Discussion

8.2.1 Clean Model Comparison

In Phase V, the effect of Reynolds number on the clean NACA 23012 airfoil performance was investigated from $Re = 4.6\times10^6$ to 15.9×10^6. Although the airfoil performance changes were significant over this range, a greater effect was observed in extending the lower limit of Re to 1.8×10^6 for the subscale model in the University of Illinois wind tunnel. Figure 35 summarizes the effect of Reynolds number on the NACA 23012 airfoil performance for the entire Reynolds number range of interest in this program, $1.8\times10^6 \le Re \le 15.9\times10^6$, at approximately matched Mach numbers, M= 0.18 and 0.20, respectively. At $Re = 15.9\times10^6$, the lift-curve slope in the linear range was very close to the value of 2π rad^{-1} derived from thin-airfoil theory (Ref. 60). At $Re = 1.8\times10^6$, the lift-curve slope was reduced to approximately 1.87π rad^{-1} in the linear range. In addition, $C_{l,\max}$ was reduced by about 20 percent, from 1.85 to 1.48, with a corresponding reduction in α_{stall}, from 18.1° to 14.4°. At the lower Reynolds number condition, the pitching moment coefficient exhibited a slightly stronger angle-of-attack dependence. In terms of drag

coefficient, the values for each Reynolds number were similar in the low-drag "bucket" evident at $Re = 1.8\times10^6$ for $0° \le \alpha \le 6°$. Outside of this range, the drag coefficient was significantly lower at the higher Reynolds number. These differences in drag were not explored in detail, but they are consistent with previously measured results for the NACA 23012 airfoil section (Ref. 60). The significant effects of Reynolds number make the subscale model a poor simulation of the full-scale model performance in the clean configuration. The opposite is largely true for the iced-airfoil configurations because of the aforementioned lack of significant Reynolds number effects. This is illustrated in the Sections 8.2.2 to 8.2.5 for the different ice accretion shapes.

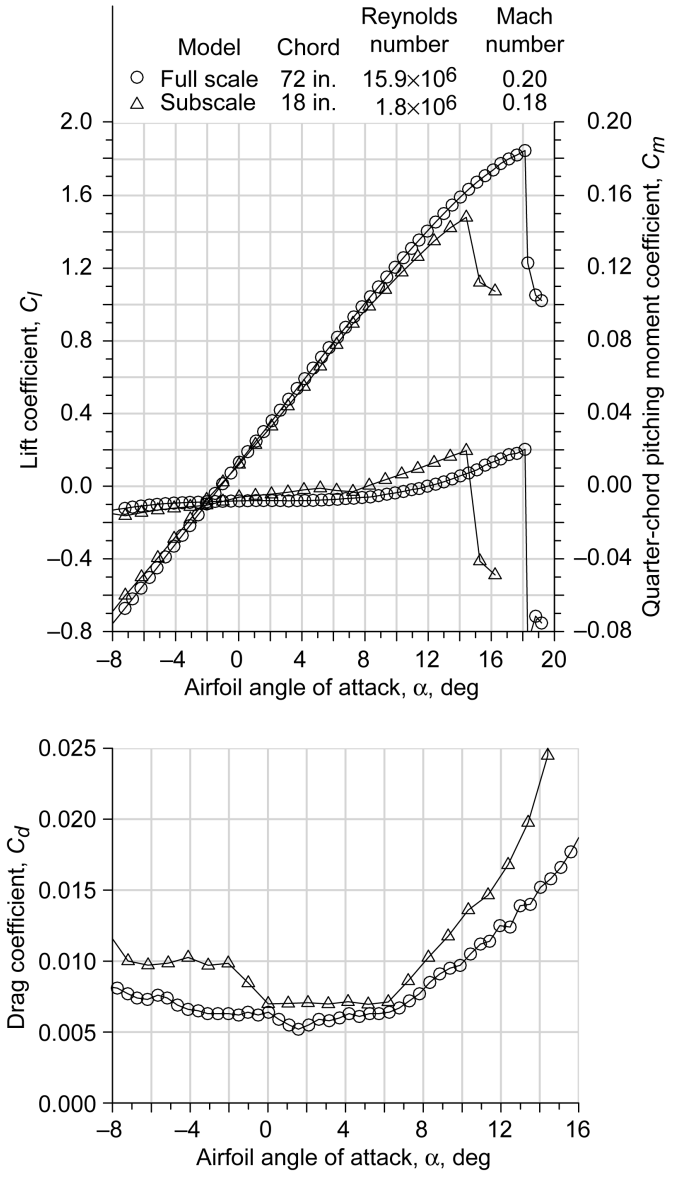

Figure 35.—Comparison of performance full-scale and subscale models of the clean NACA 23012 airfoil.

8.2.2 Horn Ice Simulation

The EG1164 horn shape was simulated with a two-dimensional smooth extrusion and with simple geometry as illustrated in Figure 36. In the latter case, the upper and lower surface horns were simulated with rectangular "spoilers" attached to the clean model surface. The two-dimensional smooth simulation was based on the pencil tracing of the EG1164 casting shown in Figure 16. These simulations were geometrically scaled according to a factor of 4 reduction in chord length between the full-scale and subscale models.

The subscale model was outfitted with these lower fidelity simulations for aerodynamic testing, and the results are shown in Figure 37. The full-scale clean and EG1164 three-dimensional casting data were acquired at $Re = 15.9\times10^6$ and $M = 0.20$. Also shown are data for the two-dimensional smooth simulation and simple-geometry simulation on the subscale model at $Re = 1.8\times10^6$ and $M = 0.18$. The scales on the plots were adjusted to highlight the comparisons in the iced-airfoil data. The data for the full-scale, three-dimensional casting configuration are considered to give the "true" iced-airfoil aerodynamics. The results show that both of the subscale simulations effectively reproduced the lift and pitching-moment characteristics of the full-scale three-dimensional casting configuration. The two-dimensional smooth configuration yielded a slightly higher maximum lift coefficient and stalling angle relative to the three-dimensional

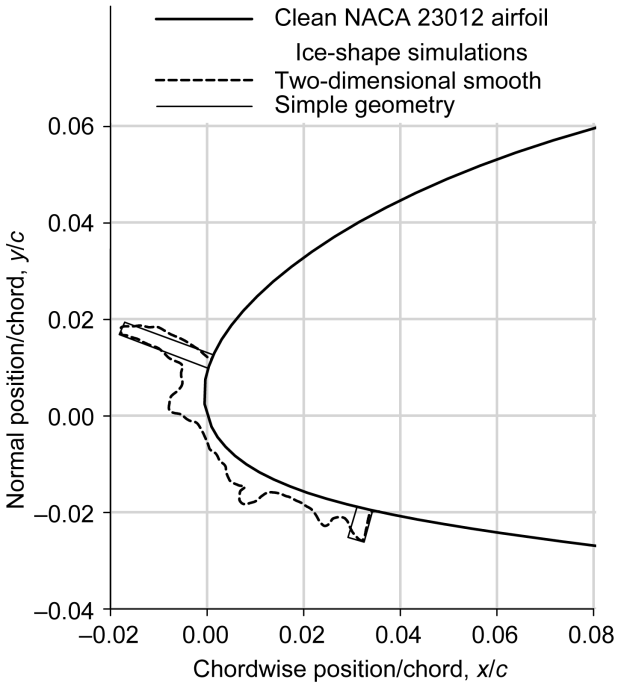

Figure 36.—Geometry comparison of two-dimensional smooth and simple-geometry simulations for the EG1164 horn ice.

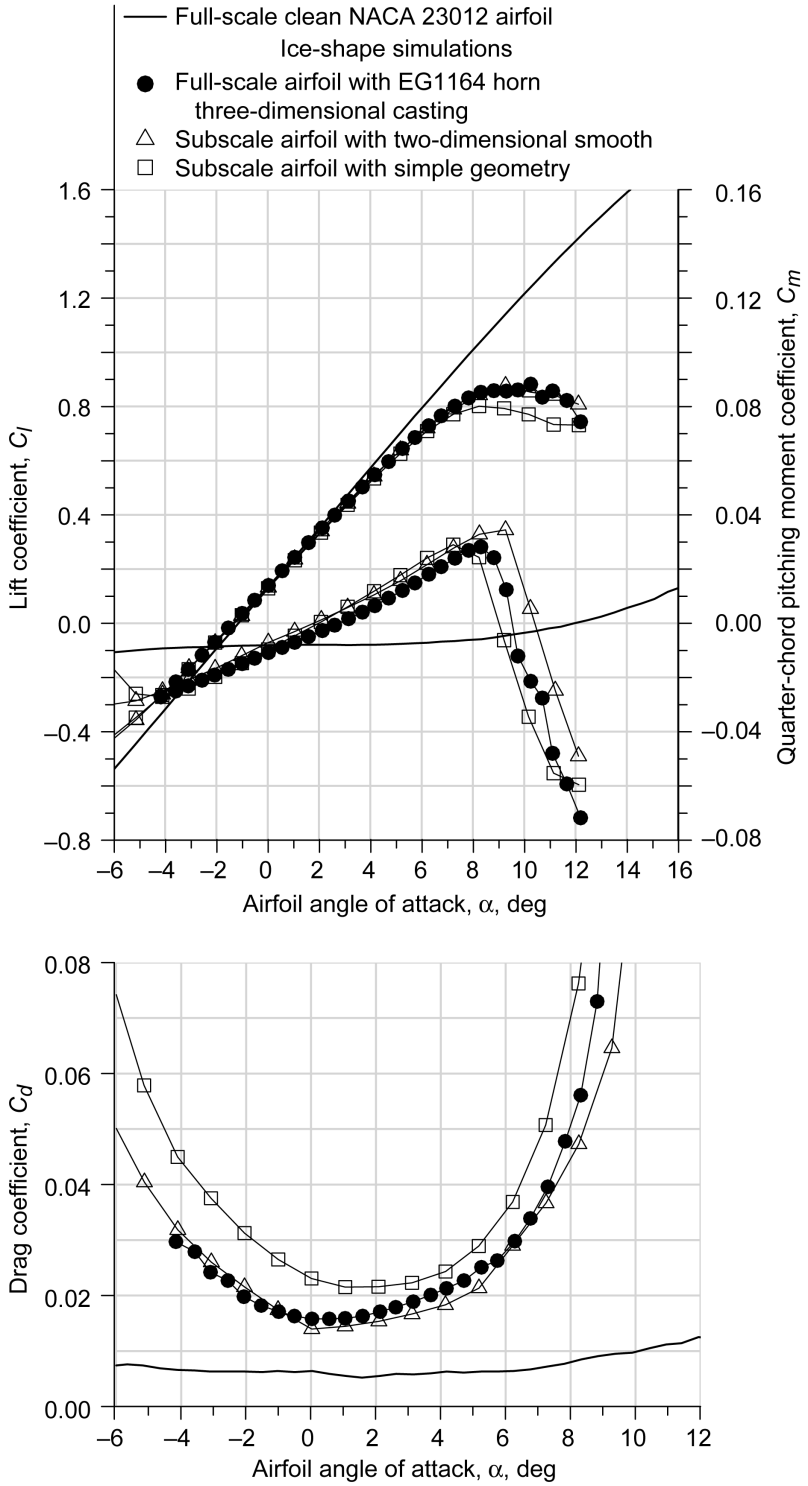

Figure 37.—Aerodynamic performance comparison of the EG1164 horn ice simulations. Full-scale data were acquired at a Reynolds number of 15.9×10^6 and a Mach number of 0.20; subscale data were acquired at a Reynolds number of 1.8×10^6 and a Mach number of 0.18.

casting configuration. In contrast, the simple-geometry simulation resulted in more conservative estimates. Busch et al. (Refs. 44 and 62) note that there was some small uncertainty in the surface location of the simple-geometry simulation, which may have contributed to the differences in the stall performance. Other research (Refs. 20, 23, and 62) has shown that maximum lift coefficient decreases with increasing horn ice-shape distance from the leading edge. Comparison of the drag coefficient shows that the simple-geometry simulation resulted in higher drag relative to the three-dimensional casting over the angle-of-attack range. This is also consistent with the lower maximum lift coefficient and the associated uncertainty of the upper surface spoiler location. The agreement in drag coefficient for the two-dimensional smooth simulation was significantly better—keeping in mind that Busch et al. (Refs. 20, 27, and 62) document significant spanwise variation in drag coefficient for horn ice shapes. Such variations could significantly affect the drag coefficient comparisons. However, extensive spanwise drag measurements were beyond the scope of this project.

Figure 38 further compares the simulation effectiveness in terms of surface pressure distribution at a matched $\alpha = 6.2°$. The full-scale clean and EG1164 configuration data were at $Re = 15.9\times10^6$ and $M = 0.20$, whereas the subscale data were at $Re = 1.8\times10^6$ and $M = 0.18$. The iced-airfoil upper surface pressure signatures were consistent with the presence of a separation bubble downstream of the horn. There was fairly good agreement between the full-scale three-dimensional casting data and that of the two-dimensional smooth simulation. For the simple-geometry case, the pressure recovery region was noticeably shifted downstream relative to the other two. This is again consistent with possible misalignment of the upper surface spoiler in the downstream direction and the resulting lower maximum lift coefficient and higher drag coefficient relative to the three-dimensional casting configuration.

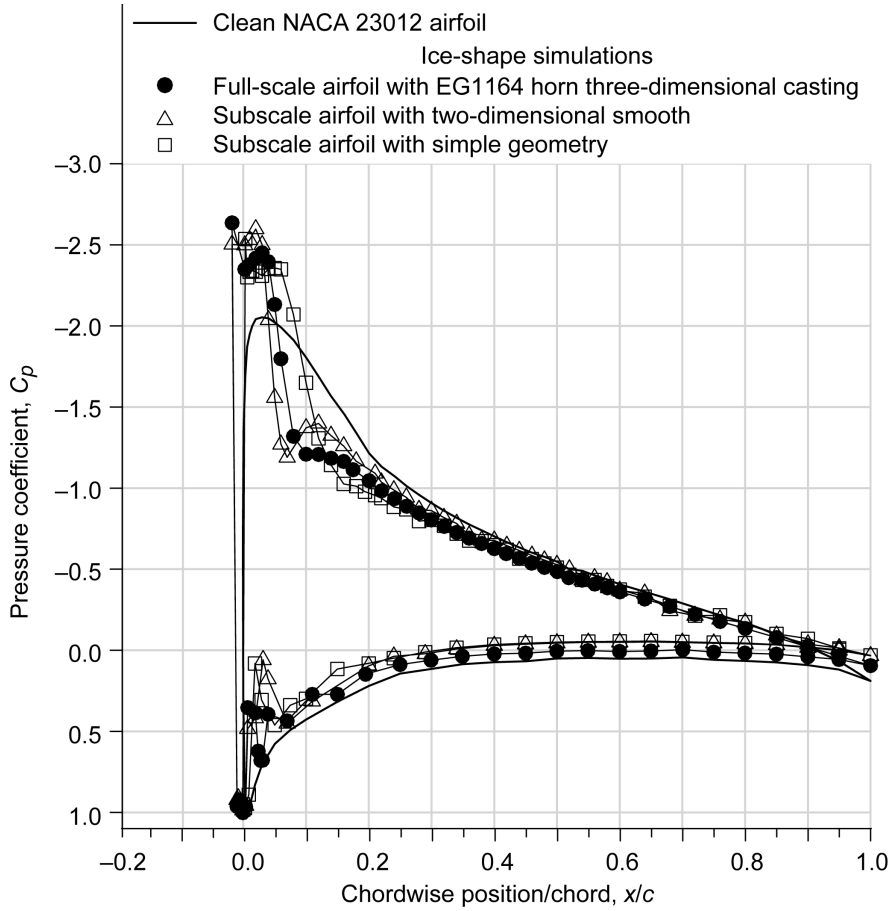

Figure 38.—Surface pressure distribution comparison of the EG1164 horn ice simulations at an angle of attack of 6.2°. Full-scale data were acquired at a Reynolds number of 15.9×10^6 and a Mach number of 0.20; subscale data were acquired at a Reynolds number of 1.8×10^6 and a Mach number of 0.18.

TABLE 11.—EFFECTIVENESS OF EG1164 HORN SHAPE SIMULATIONS ON THE SUBSCALE MODEL

[$C_{l,\max}$, maximum lift coefficient; α_{stall}, stalling angle; $\Delta C_{d,rms}$, root-mean-square percent difference in drag coefficient; α, angle of attack.]

Simulation	Simulation $C_{l,\max}$ – casting $C_{l,\max}$	Simulation α_{stall} – casting α_{stall}, deg	$\Delta C_{d,rms}$, percent ($-4° \le \alpha \le 8°$)
Two-dimensional smooth	0.03 (2.9 percent)	1.0	10.3
Simple geometry	–0.05 (–6.0 percent)	–0.1	35.7

Table 11 summarizes the effectiveness of the EG1164 subscale simulations. As in Phase III, the performance comparisons were summarized in terms of three parameters: $C_{l,\max}$, α_{stall}, and $\Delta C_{d,rms}$. Note that some of these values are slightly different from the values reported previously by Busch et al. (Refs. 44 and 62). The main reason for this is that Busch et al. (Refs. 44 and 62) used Phase V data at $Re = 12.2\times10^6$ and $M = 0.20$ as the basis of comparison instead of data at $Re = 15.9\times10^6$ and $M = 0.20$, as used here. In other instances, the authors' interpretation of α_{stall} and $C_{l,\max}$ may have been slightly different. The data in Table 11 represent the range of uncertainty in aerodynamic simulation of a horn ice shape on a subscale model.

As noted earlier in this section, the aerodynamics of the two-dimensional smooth simulation matched the full-scale iced aerodynamics very closely in terms of maximum lift and drag coefficient ($\Delta C_{d,rms}$). For the simple-geometry simulation, α_{stall} was matched to within 0.1°, whereas there were larger differences in $C_{l,\max}$ and $\Delta C_{d,rms}$. These results confirm that a successful subscale horn ice simulation ultimately depends on the ability to represent the proper size, angle, and location of the horn(s), with the detailed surface geometry and roughness being less important.

8.2.3 Ice Roughness Simulation

In the case of the ice-roughness shapes, EG1126 and EG1134, only simple-geometry simulations were developed because of the lack of a gross ice shape. That is, a two-dimensional smooth simulation (on the subscale model) would essentially be just the clean airfoil. The simple-geometry simulations were constructed by applying various sizes of grit roughness to a clean airfoil surface via strips of double-sided adhesive vinyl film. Busch et al. (Refs. 20, 44, and 62) estimated the roughness size from the three-dimensional castings used in Phase V. For the EG1126 shape, the upper surface roughness extended from $x/c = 0.000$, with height $k/c = 0.0016$, to $x/c = 0.026$, with zero height. The lower surface roughness extended from $x/c = 0.004$, with height $k/c = 0.0011$, to $x/c = 0.041$, with zero height. The roughness height and concentration gradually tapered off in the downstream direction.

Busch et al. (Refs. 20, 44, and 62) developed a geometrically scaled simulation (summarized in Table 12) that utilized several different roughness sizes. The roughness locations are reported as surface distances s/c, which is a better parameter for describing locations near the airfoil leading edge. Because of the definition of the NACA 23012 airfoil coordinates, there are negative x/c values for positive ordinates (Ref. 60). This means that there are two points at $x/c = 0$, one corresponding to $y/c = 0$ and the other to $y/c = 0.009$. Using surface arc-length with $s/c = 0$ at $x/c = y/c = 0$ eliminates any ambiguity in this regard. Furthermore, a negative s/c corresponds to the lower surface, whereas a positive s/c corresponds to the upper surface. Table 12 indicates that no roughness was applied in the range $-0.007 \le s/c \le 0.007$, which represents the smooth stagnation zone depicted in Figure 18. There are two roughness concentrations listed in the table. In this research, roughness concentration is defined as the ratio of the total planform area of the roughness elements to the total surface area on which the roughness is applied. For full concentration, roughness grains saturated the entire surface of the adhesive strip. For reduced concentration, an attempt was made to match the concentration of roughness on the three-dimensional casting. However, roughness concentration on the casting was very difficult to measure, so the simulation concentration was only qualitatively matched.

TABLE 12.—ROUGHNESS SIZE DISTRIBUTION USED TO REPRESENT THE GEOMETRICALLY SCALED EG1126 THREE-DIMENSIONAL CASTING ON THE SUBSCALE MODEL

Roughness height,[a] k/c	Concentration	Surface location,[b] s/c
Upper surface		
0.0005	Reduced	0.031 to 0.048
0.0009	Reduced	0.017 to 0.031
0.0006	Full	0.012 to 0.017
0.0013	Full	0.007 to 0.012
Leading edge—smooth, no roughness		–0.007 to 0.007
Lower surface		
0.0009	Full	–0.007 to –0.012
0.0006	Full	–0.012 to –0.017
0.0009	Reduced	–0.017 to –0.031
0.0003	Reduced	–0.031 to –0.048

[a]Ice roughness height per chord.
[b]Surface distance per chord.

Figure 39 shows aerodynamic data for various EG1126 ice-roughness simulations on the subscale model. As in Figure 37, the full-scale data for the clean and EG1126 three-dimensional casting configurations are plotted for $Re = 15.9 \times 10^6$ and $M = 0.20$. The first subscale simulation is that described earlier in this section. It is an approximately geometrically scaled simulation of the three-dimensional casting. This combination of roughness sizes, concentration, and surface extent (see Table 12) represents a typical approach to subscale simulation without any a priori knowledge of the full-scale aerodynamics. The lift and pitching-moment data show reasonable agreement with the three-dimensional casting data up to stall, where the subscale simulation had a lower α_{stall} and $C_{l,max}$. The subscale simulations do result in an abrupt stall—indicative of the leading-edge stall type observed with the three-dimensional casting configuration. In some circumstances, this could be of equal or more importance than simulating the exact values of maximum lift or stalling angle. The drag coefficient for this simulation was significantly higher than that for the three-dimensional casting, except in the range $6° \le \alpha \le 10°$.

Figure 39 shows test results for another subscale simulation that modeled the initial roughness of the EG1126 ice-roughness case. This simulation, summarized in Table 13, consisted of a narrow grit strip with upper and lower surface roughness heights equal to that of the largest and most upstream roughness of the casting. In terms of lift and pitching moment, this simulation had results nearly identical to that of the approximately geometrically scaled roughness simulation. This suggests that the roughness downstream of the initial roughness does not have a large effect on these parameters. The same cannot be said of the drag coefficient, which was significantly closer to the full-scale, three-dimensional casting results. Conversely, this suggests that the chordwise distribution of ice roughness is important for accurate drag simulation.

Finally, a third simulation was constructed with the specific intention of matching the maximum lift coefficient and stalling angle of the three-dimensional casting. For this case, $k/c = 0.0003$ roughness was applied to the upper and lower surfaces over the same chordwise extents as the ice roughness on the three-dimensional casting. As shown in Figure 39, this did have the effect of matching $C_{l,max}$ and α_{stall} almost exactly to that of the casting. However, no improvement was seen in the drag coefficient comparison relative to the geometrically scaled initial roughness simulation. For these latter two simulations, there is a distinct tradeoff in drag penalty between the height of the initial roughness and the larger chordwise extent of the smaller roughness. The drag coefficient values for each simulation were very similar up to about 2° prior to stall. These data illustrate the importance of size, concentration, and surface extent and/or location in ice-roughness simulation.

These results are summarized in Table 14 for the three performance parameters, quantifying the aforementioned observations. The $k/c = 0.0003$ roughness simulation applied over the casting extents (chordwise extent of roughness over the casting) resulted in the best match of $C_{l,max}$ and α_{stall}, as it was designed to do. But it was the geometrically scaled initial roughness simulation that best matched the drag performance with the lowest $\Delta C_{d,rms}$. These results indicate that it may be very difficult to find one roughness size and extent that performs the best across all three parameters. The data further suggest that simple geometric scaling may not be adequate for ice roughness over this range of model scale and Reynolds number. The geometrically scaled simulations are conservative relative to the full-scale results, and this may be advantageous for safety-related testing.

TABLE 13.—ROUGHNESS SIZE DISTRIBUTION USED TO REPRESENT THE GEOMETRICALLY SCALED INITIAL ROUGHNESS OF EG1126 THREE-DIMENSIONAL CASTING ON THE SUBSCALE MODEL

Roughness height,[a] k/c	Concentration	Surface location,[b] s/c
Upper surface		
0.0013	Full	0.007 to 0.013
Leading edge—smooth, no roughness		–0.007 to 0.007
Lower surface		
0.0009	Full	–0.007 to –0.013

[a]Ice roughness height per chord.
[b]Surface distance per chord.

TABLE 14.—EFFECTIVENESS OF EG1126 ROUGHNESS SIMULATIONS ON THE SUBSCALE MODEL
[$C_{l,max}$, maximum lift coefficient; α_{stall}, stalling angle; $\Delta C_{d,rms}$, root-mean-square percent difference in drag coefficient; α, angle of attack; k/c, ice roughness height per chord length.]

Simulation	Simulation $C_{l,max}$ – casting $C_{l,max}$	Simulation α_{stall} – casting α_{stall}, deg	$\Delta C_{d,rms}$, percent ($-4° \le \alpha \le 9°$)
Approximately geometrically scaled (see Table 12)	–0.04 (–3.5 percent)	–1.0	28.6
Geometrically scaled initial roughness (see Table 13)	–0.03 (–3.0 percent)	–1.0	13.1
$k/c = 0.0003$ roughness with casting extents[a]	–0.01 (–0.6 percent)	–0.1	19.4

[a]Chordwise extent of roughness over the casting.

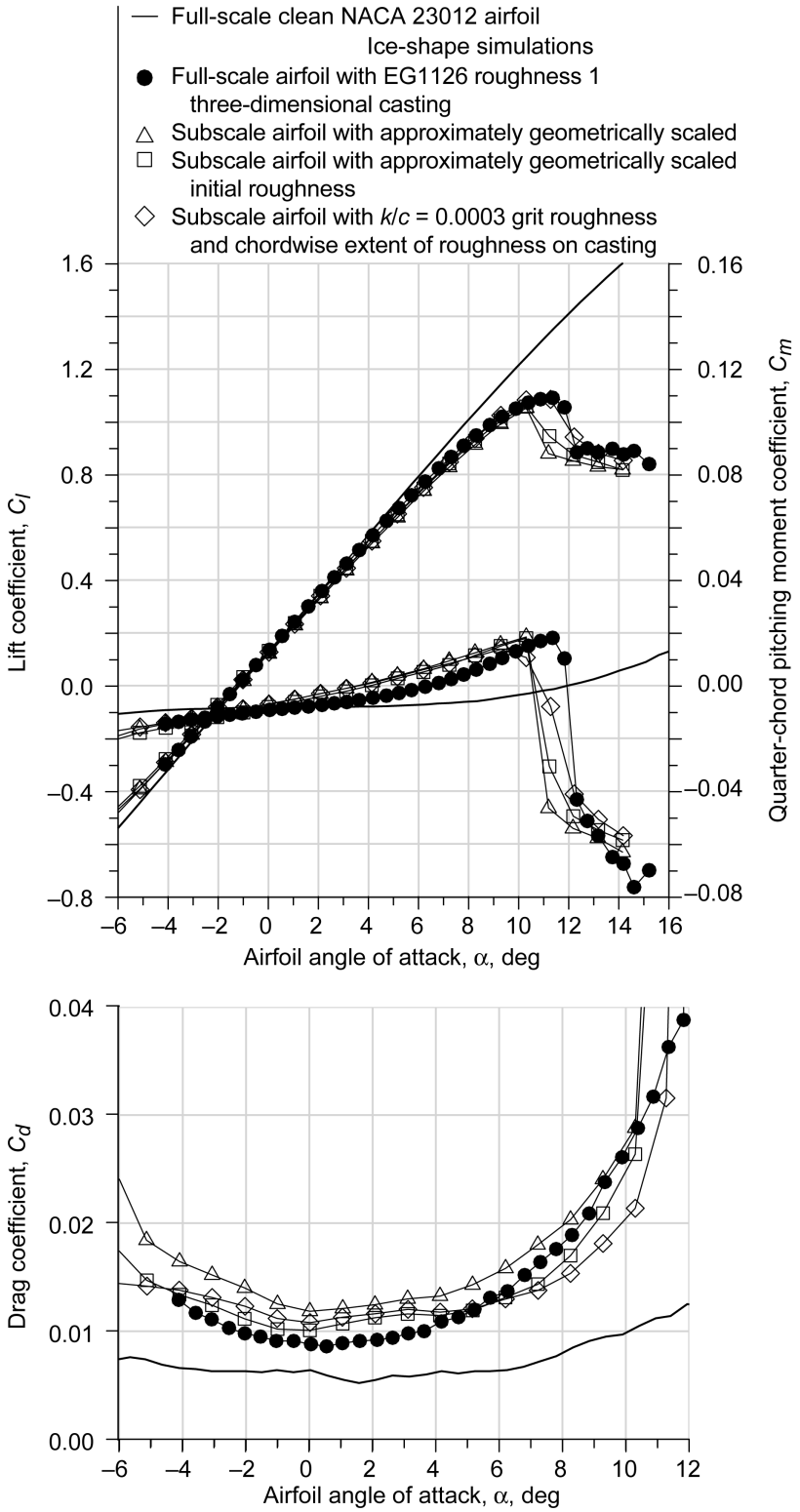

Figure 39.—Aerodynamic performance comparison of the EG1126 ice-roughness simulations. Full-scale data were acquired at a Reynolds number of 15.9×10^6 and a Mach number of 0.20; subscale data were acquired at a Reynolds number of 1.8×10^6 and a Mach number of 0.18; k/c, roughness height per chord length.

Alternative scaling methods, such as boundary-layer-based scaling has been proposed in other work (Ref. 63). Boundary-layer-based scaling methods match the roughness size k based on the boundary-layer thickness δ. So the ratio k/δ would be equal between the full and subscale roughness. Boundary-layer thickness decreases as Reynolds number increases, which means that the boundary-layer thickness is larger on the subscale model. This leads to roughness simulations based on k/δ that are larger than roughness simulations based on k/c. On the basis of the data shown here, larger roughness on the subscale model would lead to larger differences in performance between the full-scale model and a geometrically scaled simulation.

In the aggregate, the data for these three roughness cases broadly illustrate the nature of roughness effects on aerodynamics. As expected from Phase I and Phase III, the size, concentration, and chordwise location and/or extent all play a role in determining the aerodynamic effect. This prompted Busch et al. (Refs. 44 and 62) to conduct a detailed study of these parameters on the subscale NACA 23012 airfoil, using the EG1126 three-dimensional casting as a baseline. The authors found that for a fixed roughness size of $k/c = 0.0018$, $C_{l,\max}$ decreased with increasing concentration up to a critical value of about 20 percent, above which $C_{l,\max}$ did not decrease significantly. These results are consistent with the roughness applied to streamwise ice simulations discussed in Phase III and in an earlier airfoil study by Jackson (Ref. 64). For drag coefficient, the authors found no such critical value. The $\Delta C_{d,\mathrm{rms}}$ between the roughness simulation and the three-dimensional casting tended only to increase as concentration was increased. Busch et al. (Refs. 44 and 62) also studied the effect of roughness size on the NACA 23012 airfoil. These cases were applied at full concentration to minimize any effects of concentration. They found that $C_{l,\max}$ decreased significantly from 1.48 on the clean model to 1.09 for $k/c = 0.0003$. For larger roughness sizes, the reduction in $C_{l,\max}$ was more modest, with $C_{l,\max} = 0.90$ for $k/c = 0.0037$. The reduced sensitivity of $C_{l,\max}$ for $k/c \geq 0.0003$ is consistent with the Phase III ED0762 ice-roughness results, as well as for larger ice shapes located on the leading edge as discussed in Phase V. The drag results, however, showed that C_d (or at least $\Delta C_{d,\mathrm{rms}}$ relative to the three-dimensional casting) tended to increase approximately proportionally with increases in roughness size.

These results confirm the finding of the Phase I study that understanding the aerodynamic effects of roughness size and concentration is important to accurate subscale simulation. Geometric scaling of ice roughness was found to produce conservative aerodynamic performance penalties for the range of model scale and Reynolds number used in this research. Because of the tradeoffs in aerodynamic effect among size, concentration, and surface extent and/or location, more research is needed to understand how to design more accurate subscale-model ice-roughness simulations.

These ice-roughness effects were investigated further for the EG1134 shape, which was also tested in Phase V. This configuration had a much larger chordwise extent of roughness than did the previous EG1126 configuration, from $x/c = -0.002$ to 0.080 on the upper surface and from approximately $x/c = 0.000$ to 0.200 on the lower surface. The maximum height was about $k/c = 0.0003$ on each surface, occurring nearest the leading edge and gradually tapering off downstream. The approximately geometrically scaled simulation for this case was identical to the $k/c = 0.0003$ roughness case used for the EG1126 experiments described earlier and in Table 15. This simulation matched the height of the initial roughness on the EG1134 three-dimensional casting, but not the entire surface extent. The aerodynamic results are compared in Figure 40. This roughness simulation on the subscale model resulted in significantly lower $C_{l,\max}$ and α_{stall} and higher C_d for $\alpha < \sim 4°$. On the basis of the research conducted for the EG1126 configuration, increasing the chordwise extent of the roughness on the subscale simulation to better match the EG1134 ice-roughness geometry would likely not have a measurable impact on the stalling characteristics while most likely increasing drag. Since this would not improve the comparison with the three-dimensional casting aerodynamics, higher fidelity, geometrically scaled roughness simulations were not considered. However, it is reasonable to consider the $k/c = 0.0003$ roughness to be an approximately geometrically scaled simulation since the height of the initial roughness was geometrically scaled from the full-scale, EG1134 three-dimensional casting. These results are consistent with the EG1126 simulation results in that geometrically scaled roughness simulations yield conservative estimates of the full-scale iced-airfoil performance. Such a subscale configuration is often selected without any knowledge of the full-scale aerodynamics.

TABLE 15.—ROUGHNESS SIZE DISTRIBUTION USED TO REPRESENT THE GEOMETRICALLY SCALED EG1134 THREE-DIMENSIONAL CASTING ON THE SUBSCALE MODEL

Roughness height,[a] k/c	Concentration	Surface location,[b] s/c
Upper surface		
0.0003	Full	0.007 to 0.048
Leading edge—smooth, no roughness		–0.007 to 0.007
Lower surface		
0.0003	Full	–0.007 to –0.048

[a]Ice roughness height per chord.
[b]Surface distance per chord.

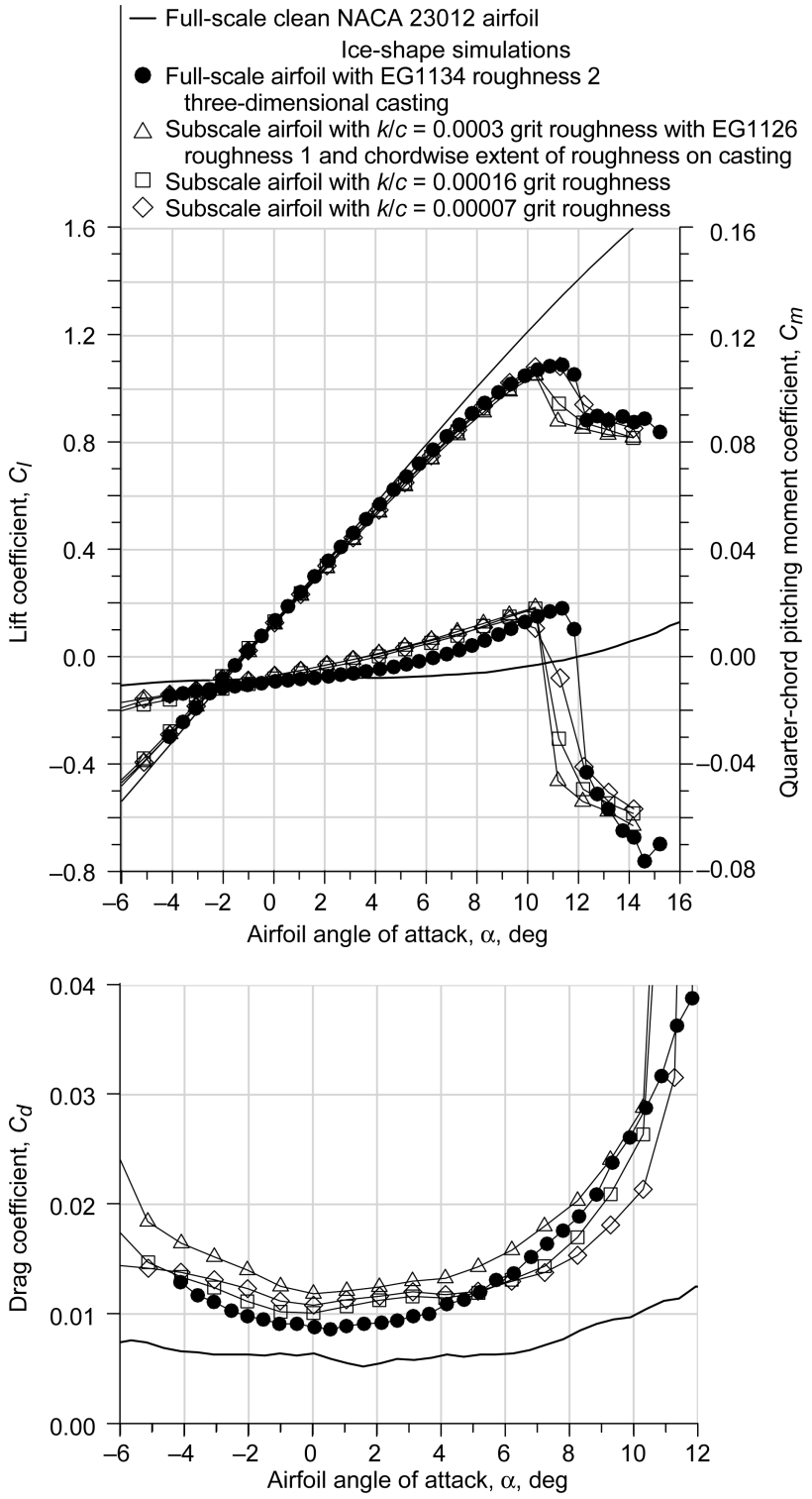

Figure 40.—Aerodynamic performance comparison of the EG1134 ice-roughness simulations. Full-scale data were acquired at a Reynolds number of 15.9×10^6 and a Mach number of 0.20; subscale data were acquired at a Reynolds number of 1.8×10^6 and a Mach number of 0.18; *k*/*c*, roughness height per chord length.

TABLE 16.—EFFECTIVENESS OF EG1134 ROUGHNESS SIMULATIONS ON THE SUBSCALE MODEL
[k/c, ice roughness height per chord length; $C_{l,\max}$, maximum lift coefficient; α_{stall}, stalling angle; $\Delta C_{d,\mathrm{rms}}$, root-mean-square percent difference in drag coefficient; α, angle of attack.]

Simulation k/c roughness	Simulation $C_{l,\max}$ – casting $C_{l,\max}$	Simulation α_{stall} – casting α_{stall}, deg	$\Delta C_{d,\mathrm{rms}}$, percent ($-4° \le \alpha \le 10°$)
0.0003 with EG1126 extents	–0.19 (–15.0 percent)	–1.7	16.4
0.00016	–0.05 (–3.8 percent)	–0.6	13.5
0.00007	0.02 (1.5 percent)	–0.1	7.8

Two other roughness sizes were applied to the subscale model for comparison to the EG1134 three-dimensional casting configuration. The roughness sizes tested were approximately one-half and one-quarter of the height of the approximately geometrically scaled roughness. These aerodynamic results are compared in Figure 40, and data show that the $k/c = 0.00007$ roughness best matched the performance of the full-scale, three-dimensional casting simulation. The simulation effectiveness is summarized in Table 16. The significant improvement in $C_{l,\max}$ between roughnesses of $k/c = 0.0003$ and 0.00007 further illustrates the sensitivity to roughness height in this range, which was discussed earlier in this section. Contrast this effect to roughness sizes larger than $k/c = 0.0003$, which had reduced $C_{l,\max}$ sensitivity (see Figure 39 and Table 14). Significant improvements were also observed in α_{stall} and $\Delta C_{d,\mathrm{rms}}$ comparisons with the three-dimensional casting. The results for the $k/c = 0.00007$ roughness simulation of the EG1134 casting were only possible because the full-scale aerodynamics were known. An appropriate scaling length or method that would lead to this result without any knowledge of the full-scale aerodynamics is unknown.

8.2.4 Streamwise Ice Simulation

There were two full-scale streamwise ice shapes tested in Phase V: EG1162 and EG1125. The latter, depicted in Figure 20, was characterized by a gross ice shape that protruded from the airfoil leading edge, with significant geometric slope discontinuities at the ice-to-airfoil junction and large roughness. The EG1162 shape, depicted in Figure 17, was more conformal to the leading edge of the NACA 23012 airfoil. This ice shape also had large roughness immediately downstream of the smooth stagnation point region. Busch et al. (Refs. 44 and 62) report that the upper surface roughness extended from $x/c = -0.008$ to 0.065 with a maximum height of $k/c = 0.0014$. The lower surface roughness extended from $x/c = -0.005$ to 0.060 with a maximum height of $k/c = 0.0011$. Both of these streamwise ice shapes were geometrically scaled and simulated on the subscale model by using two-dimensional smooth and simple-geometry shapes with and without added roughness.

The cross-section geometries for the lower fidelity simulations of the EG1162 shape are shown in Figure 41. The two-dimensional smooth simulation was based on a pencil tracing of the full-scale three-dimensional casting with no further smoothing. It was fabricated using stereolithography. The simple-geometry simulation was built up on the clean leading edge of the subscale model. Spanwise-running spacers were used to replicate the "high points" of the ice cross section and a thin-film covering was applied over the top of the spacers (Ref. 62). This resulted in a smoothly wrapped surface. Both of these artificial ice shapes were geometrically scaled according to a factor of 4 reduction in chord length between the full-scale and subscale models. Various sizes of grit roughness were also applied to the two-dimensional smooth and simple-geometry configurations at chordwise locations and extents similar to the casting. Roughness was applied in a fully saturated concentration to minimize possible variations due to differences in concentration.

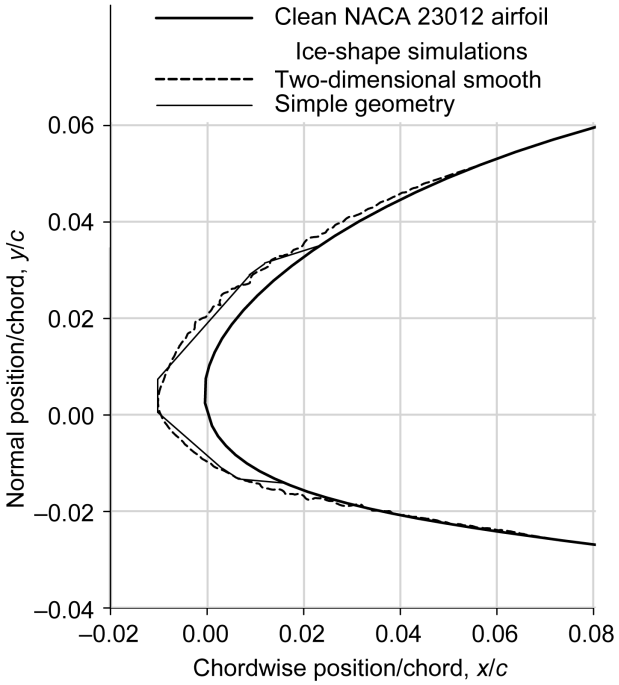

Figure 41.—Geometry comparison of two-dimensional smooth and simple-geometry simulations for streamwise ice shape EG1162.

Figure 42 illustrates the effectiveness of the subscale, lower fidelity simulations of the EG1162 streamwise shape. As before, the full-scale data were acquired at Re = 15.9×10^6 and M = 0.20, and the subscale data were acquired at Re = 1.8×10^6 and M = 0.18. The data for the three-dimensional casting simulation are considered to give the "true" iced-airfoil aerodynamic performance. For lift and pitching moment, the subscale simulations resulted in reasonable agreement with the three-dimensional casting data up to stall. The subscale simulations had an abrupt, leading-edge stall that accurately represented the full-scale behavior. However, both subscale simulations yielded a $C_{l,\max}$ that was too high, whereas α_{stall} for the two-dimensional smooth configuration was lower than that of the three-dimensional casting, and α_{stall} for the simple-geometry configuration was higher than that of the three-dimensional casting. In terms of drag, both subscale simulations matched the full-scale three-dimensional casting data very well up to about $\alpha = 4°$, where the data started to diverge. It is interesting to note the striking similarities in these results to the Phase III experiments with the ED0730 streamwise shape. The aerodynamic performance data for the two-dimensional smooth and simple-geometry configurations relative to the three-dimensional casting shown in Figure 11 were nearly identical to those observed here. More accurate simulation thus required representation of the ice roughness in addition to the gross ice geometry.

Numerous trials were conducted with grit roughness added to the two-dimensional smooth and simple-geometry representations of the EG1162 streamwise shape. The roughness was applied to the subscale simulations at the appropriate locations according to where it was found on the three-dimensional casting. Figure 43 shows an example of the aerodynamic results for roughness added to the two-dimensional smooth simulation. Two roughness sizes are shown, $k/c = 0.0013$ and 0.0003. The former corresponds to approximately geometrically scaled roughness, whereas the latter was determined empirically to give the best agreement with the three-dimensional casting data. Therefore, the two-dimensional smooth simulation with the $k/c = 0.0013$ roughness could be considered to be the highest fidelity subscale simulation without a priori knowledge of the three-dimensional casting configuration aerodynamics. The performance data plotted in Figure 43 indicate that this subscale configuration results in very conservative performance penalties relative to the full-scale three-dimensional casting configuration. In contrast, $k/c = 0.0003$ roughness improves the simulation fidelity of the two-dimensional smooth simulation. This conundrum is identical to that faced in the ice-roughness simulations discussed in the previous section. It is not clear which length scale would lead to the selection of $k/c = 0.0003$ roughness without advanced knowledge of the full-scale, iced-airfoil aerodynamics.

The aerodynamic comparisons of the subscale simulation effectiveness of the full-scale EG1162 streamwise shape are summarized in Table 17 in terms of $C_{l,\max}$, α_{stall}, and $\Delta C_{d,\mathrm{rms}}$. The first three simulations that were geometrically scaled required no a priori knowledge of the full-scale iced-airfoil aerodynamics. An interesting result is that, overall, more accurate simulation was achieved by neglecting to add roughness. However, the uncertainty is biased toward the nonconservative side, with overestimates of $C_{l,\max}$ and α_{stall} and an underestimate of drag relative to the three-dimensional casting data. Adding geometrically scaled roughness to either subscale simulation produced much more conservative results as indicated in the table for the two-dimensional smooth case. The addition of $k/c = 0.0003$ roughness to the two-dimensional smooth simulation did not change the resulting $C_{l,\max}$, but it did improve the α_{stall} comparison. Although $\Delta C_{d,\mathrm{rms}}$ is very similar for the two cases, inspection of Figure 43 shows that the addition of roughness resulted in slightly higher drag than for the three-dimensional casting configuration, whereas for the two-dimensional smooth configuration the drag coefficient was lower. It is also important to note that the leading-edge stall character of the full-scale iced airfoil was adequately represented with each of the subscale simulations.

The other streamwise ice shape tested in Phase V, EG1125, was less conformal to the airfoil leading edge with large rime-feather roughness as shown in Figure 20. Busch et al. (Refs. 44 and 62) report that the upper surface roughness extended from $x/c = -0.008$ to 0.019 and had a maximum height of $k/c = 0.0018$. On the lower surface, roughness extended from $x/c = -0.006$ to 0.029 and had a maximum height of $k/c = 0.0012$. Geometrically scaled, lower fidelity simulations were fabricated using methods similar to the EG1162 configuration described earlier in this section, including the addition of grit roughness. Figure 44 depicts the cross-sectional geometries of the two-dimensional smooth and simple-geometry simulations. Busch et al. (Refs. 44 and 62) note that there was a key difference in these two simulations for the EG1125 shape. Cross sections of upper and lower surface rime feathers recorded during the tracing process resulted in small, spanwise-running ridges in the two-dimensional smooth extrusion located near the ice/airfoil junction as shown in Figure 44. Since these rime feathers were fundamentally three-dimensional features of the ice accretion, the resulting spanwise-running ridges on the two-dimensional smooth simulation were not the best representation of the ice accretion. These ridges were faired into the main ice shape by covering the entire simulation with an adhesive film. This is similar to the method used to fabricate the simple-geometry simulation, except that, in this case, the two-dimensional smooth geometry was used as the substrate instead of the spanwise-running spacers.

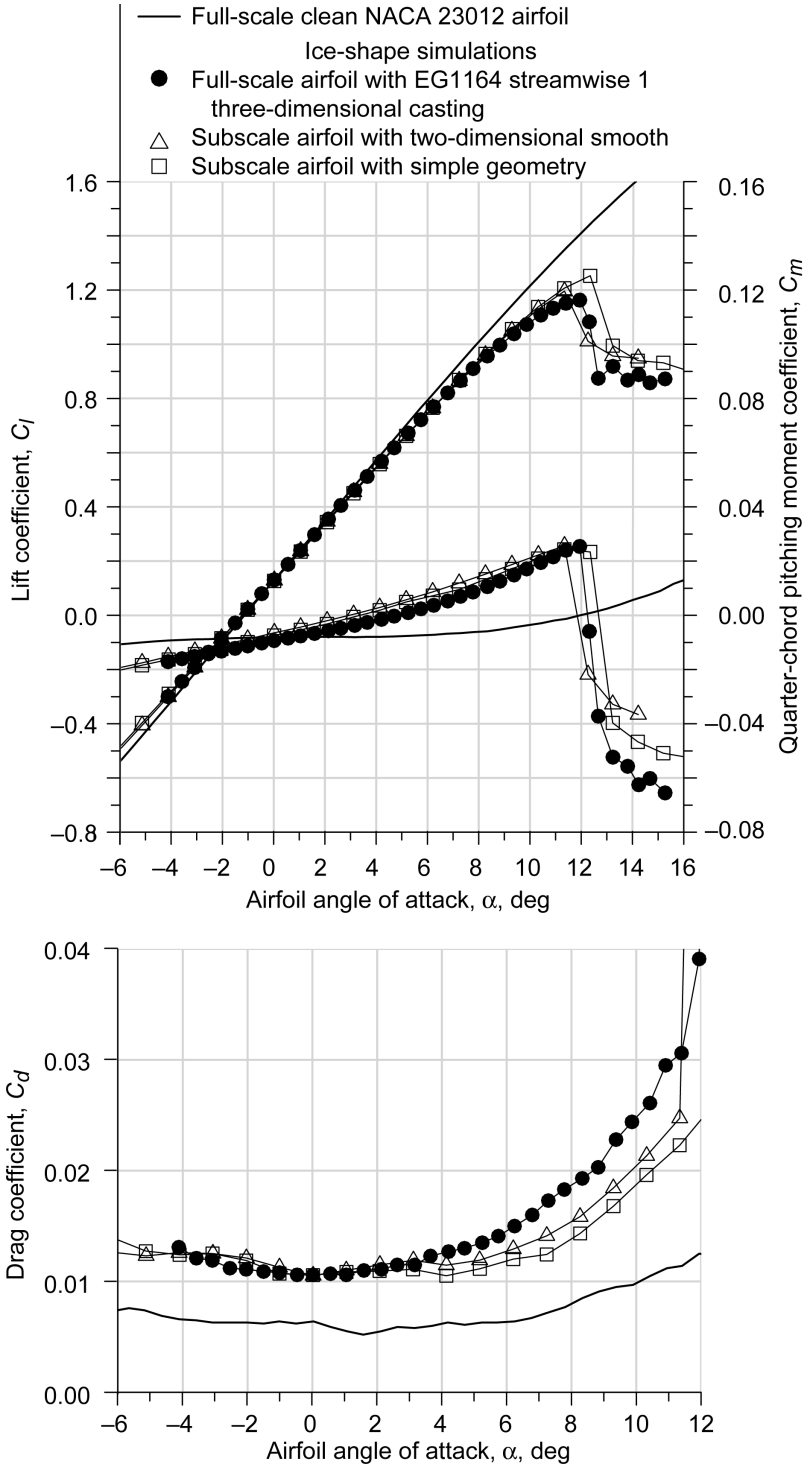

Figure 42.—Aerodynamic performance comparison of the EG1162 streamwise ice simulations. Full-scale data were acquired at a Reynolds number of 15.9×10^6 and a Mach number of 0.20; subscale data were acquired at a Reynolds number of 1.8×10^6 and a Mach number of 0.18.

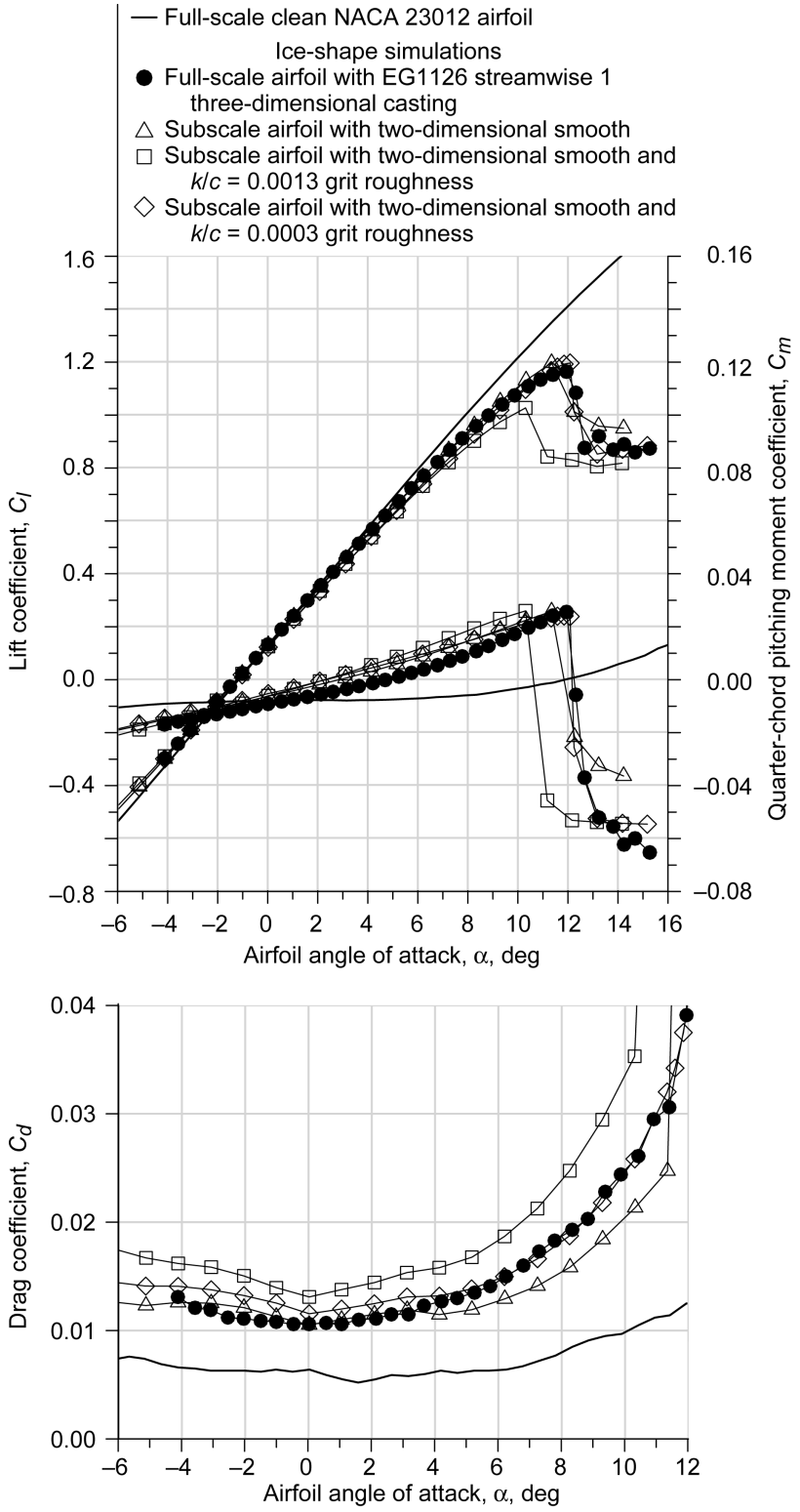

Figure 43.—Aerodynamic performance comparison of the EG1162 streamwise ice simulations with added roughness. Full-scale data were acquired at a Reynolds number of 15.9×10^6 and a Mach number of 0.20; subscale data were acquired at a Reynolds number of 1.8×10^6 and a Mach number of 0.18; *k*/*c*, roughness height per chord length.

TABLE 17.—EFFECTIVENESS OF EG1162 STREAMWISE ICE SIMULATIONS ON THE SUBSCALE MODEL
[$C_{l,\max}$, maximum lift coefficient; α_{stall}, stalling angle; $\Delta C_{d,rms}$, root-mean-square percent difference in drag coefficient; α, angle of attack; k/c, ice roughness height per chord length.]

Simulation	Simulation $C_{l,\max}$ – casting $C_{l,\max}$	Simulation α_{stall} – casting α_{stall}, deg	$\Delta C_{d,rms}$, percent ($-4° \le \alpha \le 10°$)
Two-dimensional smooth	0.03 (2.8 percent)	–0.6	11.4
Simple geometry	0.09 (7.7 percent)	0.4	16.1
Two-dimensional smooth with k/c = 0.0013 roughness	–0.14 (–11.8 percent)	–1.6	28.8
Two-dimensional smooth with k/c = 0.0003 roughness	0.03 (2.8 percent)	0.1	10.3

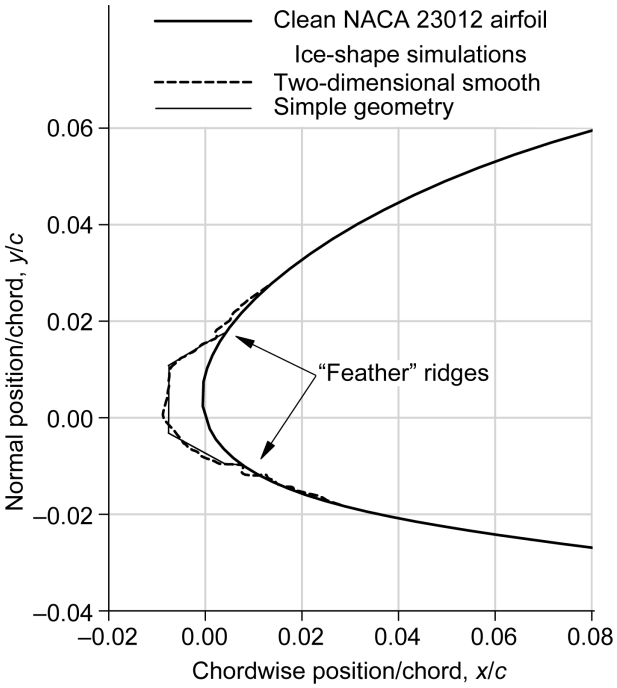

Figure 44.—Geometry comparison of two-dimensional smooth and simple-geometry simulations for EG1125 streamwise ice shape.

The aerodynamic effect of these subscale, lower fidelity simulations for the full-scale EG1125 shape are illustrated in Figure 45, using the same Reynolds and Mach number combinations as in the previous plots. The data show that the simple-geometry simulation had the best overall agreement with the performance results for the three-dimensional casting. For C_l and C_m in the stall region, the gradual, trailing-edge stall characteristics were preserved, but $C_{l,\max}$ and α_{stall} were slightly higher for the simple-geometry configuration. The comparison in drag coefficient is very good over the entire angle-of-attack range shown, resulting a very low value of $\Delta C_{d,rms}$ = 7.6 percent. For the two-dimensional smooth simulation, the comparison was not as good, particularly in that the drag coefficient was higher than for the three-dimensional casting over the entire angle-of-attack range shown in Figure 45. However, the performance results clearly show the effect of fairing the feather ridges that were inadvertently incorporated into the two-dimensional smooth simulation. Busch et al. (Refs. 44 and 62) gauged this effect by fairing the ridges and greatly improved the comparison to the three-dimensional casting data over the baseline two-dimensional smooth simulation. There was only a slight overestimation of $C_{l,\max}$ and α_{stall}, and C_d was only slightly underestimated for $\alpha > \sim 6°$. These trends relative to the three-dimensional casting data are very similar to those observed for the two-dimensional smooth simulation of the EG1162 shape (see Figure 42).

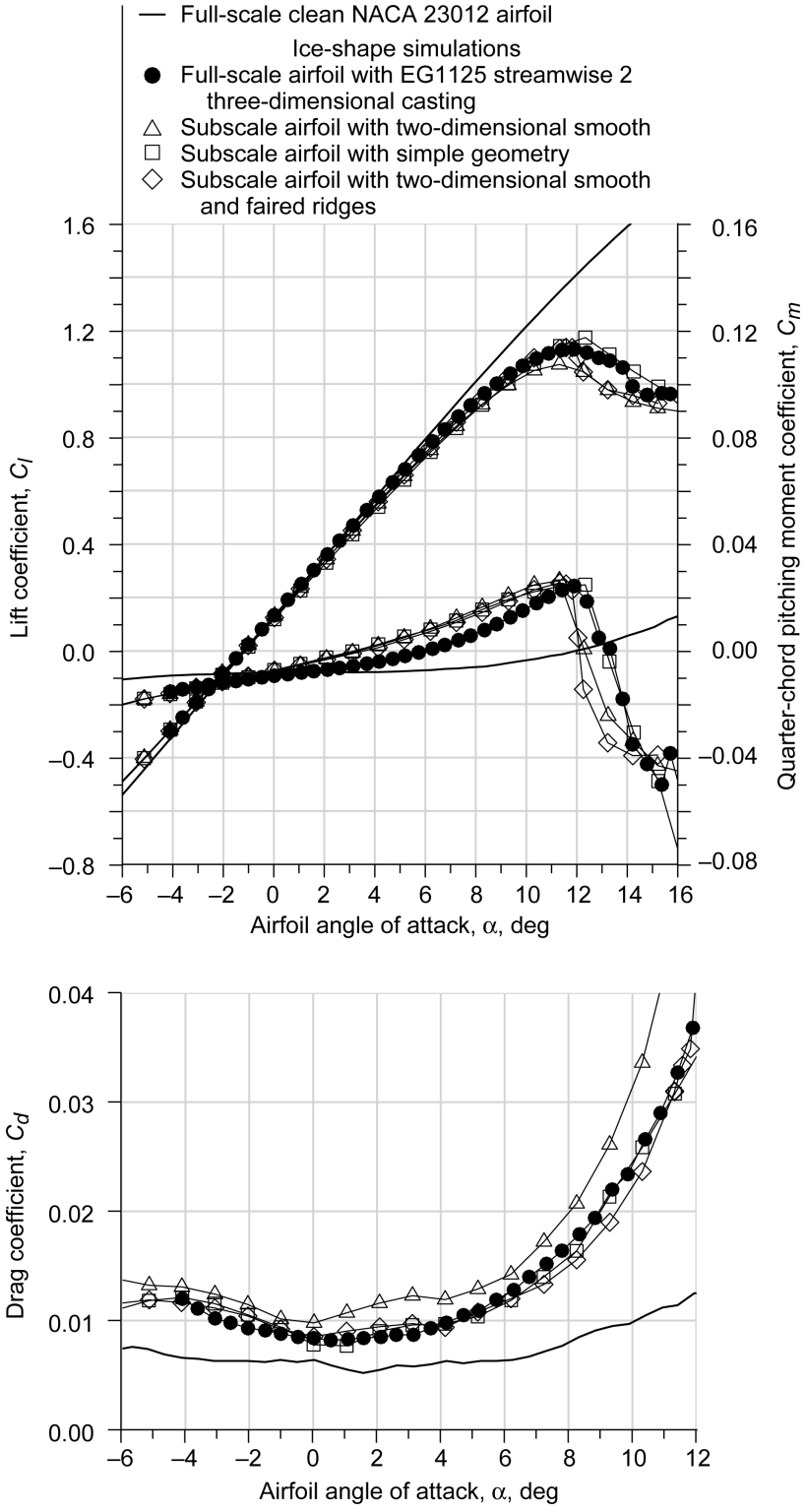

Figure 45.—Aerodynamic performance comparison of the EG1125 streamwise ice simulations. Full-scale data were acquired at a Reynolds number of 15.9×10^6 and a Mach number of 0.20; subscale data were acquired at a Reynolds number of 1.8×10^6 and a Mach number of 0.18.

Figure 46 summarizes the effect of roughness added to the EG1125 two-dimensional smooth simulation. Since the grit roughness was applied using double-sided adhesive films, the film substrate had the effect of fairing the feather ridges. Therefore, that configuration was an appropriate basis for comparison as plotted in the figure. The first roughness variation shown was approximately geometrically scaled roughness applied to the two-dimensional smooth simulation. It consisted of $k/c = 0.0015$ roughness on the upper surface and $k/c = 0.0012$ and 0.0009 roughness on the lower surface. This was the highest fidelity subscale simulation constructed without a priori knowledge of the full-scale data. The results are very similar to those for the geometrically scaled roughness ($k/c = 0.0013$) applied to the two-dimensional smooth simulation of the EG1162 shape shown in Figure 43. The roughness was clearly too large for adequate aerodynamic representation of the three-dimensional casting because of the lower $C_{l,\max}$ and α_{stall} and higher C_d over the entire angle of attack range. Several empirical trials were conducted for roughness of various sizes in order to improve the matching with the three-dimensional casting aerodynamic performance. The best result was for $k/c = 0.00007$ roughness, as indicated in Figure 46. For this configuration, the stalling characteristics in terms of $C_{l,\max}$ and α_{stall} were adequately matched to the casting, whereas the C_d of the subscale simulation was higher up to $\alpha = 6°$, where there was a crossover. These results are very analogous to those observed for the EG1162 case. This suggests that the aerodynamic results for subscale simulation of the full-scale streamwise ice shapes may be applicable to a broader range of streamwise ice accretions as classified by the chief aerodynamic characteristics described in Phase I.

Further comparisons between the EG1162 and EG1125 simulation effectiveness can be drawn in terms of $C_{l,\max}$, α_{stall}, and $\Delta C_{d,rms}$ shown in Table 18 for subscale simulations of the latter relative to the full-scale, three-dimensional casting results. The first three simulations listed were geometrically scaled and required no a priori knowledge of the full-scale, iced-airfoil aerodynamics. Note that the two-dimensional smooth simulation, listed last, was also geometrically scaled. However, this was not used for comparison because of the inadvertent inclusion of the spanwise-running ridges resulting from tracing a fundamentally three-dimensional ice feature. As for the EG1162 configuration, more accurate simulation was achieved without added roughness, with the caveat that the results are biased toward nonconservative performance penalties. Even in the case of the $k/c = 0.00007$ roughness, which was specifically selected to improve the comparison, only modest improvement is observed in $C_{l,\max}$ and α_{stall}, whereas $\Delta C_{d,rms}$ increased by nearly a factor of 2 from the two-dimensional smooth with faired feathers and simple-geometry configurations. The simulations without roughness did have a slightly sharper stalling characteristic than did the full-scale EG1125 case, which may be important in some cases.

8.2.5 Spanwise-Ridge Ice Simulation

The final type of ice shape investigated in Phase VI was the spanwise ridge represented by the EG1159 shape described in Phase V. This ice shape was simulated with a two-dimensional smooth extrusion and simple geometry as illustrated in Figure 47. As for the other ice shapes, the two-dimensional smooth simulation was based on a pencil tracing of the EG1159 three-dimensional casting shown in Figure 19 and was fabricated using stereolithography. The simple-geometry simulation was constructed using rectangular spoilers attached to the clean model surface at the appropriate locations, as indicated in Figure 47. Both of these artificial ice shapes were geometrically scaled according to a factor of 4 reduction in chord length between the full-scale and subscale models.

The subscale model was outfitted with these lower fidelity simulations for aerodynamic testing, and the results are provided in Figure 48. The full-scale clean and EG1159 three-dimensional casting data were acquired at $Re = 15.9\times10^6$ and $M = 0.20$. Also shown are data for the two-dimensional smooth simulation and the simple-geometry simulation on the subscale model at $Re = 1.8\times10^6$ and $M = 0.18$. The data for the three-dimensional casting configuration are considered to give the "true" iced-airfoil aerodynamics. The results show that both of the subscale simulations effectively reproduced the lift and pitching-moment characteristics of the three-dimensional casting configuration. For both subscale ice configurations, the

TABLE 18.—EFFECTIVENESS OF EG1125 STREAMWISE ICE SIMULATIONS ON THE SUBSCALE MODEL
[$C_{l,\max}$, maximum lift coefficient; α_{stall}, stalling angle; $\Delta C_{d,rms}$, root-mean-square percent difference in drag coefficient; α, angle of attack; k/c, ice roughness height per chord length.]

Simulation	Simulation $C_{l,\max}$ – casting $C_{l,\max}$	Simulation α_{stall} – casting α_{stall}, deg	$\Delta C_{d,rms}$, percent ($-4° \le \alpha \le 9°$)
Two-dimensional smooth with faired ridges	0.01 (0.6 percent)	–0.3	8.9
Simple geometry	0.04 (3.8 percent)	0.4	7.6
Two-dimensional smooth with geometrically scaled roughness	–0.13 (–11.1 percent)	–0.6	46.3
Two-dimensional smooth with $k/c = 0.00007$ roughness	0.0 (–0.2 percent)	–0.6	15.9
Two-dimensional smooth	–0.06 (–5.1 percent)	–0.6	21.9

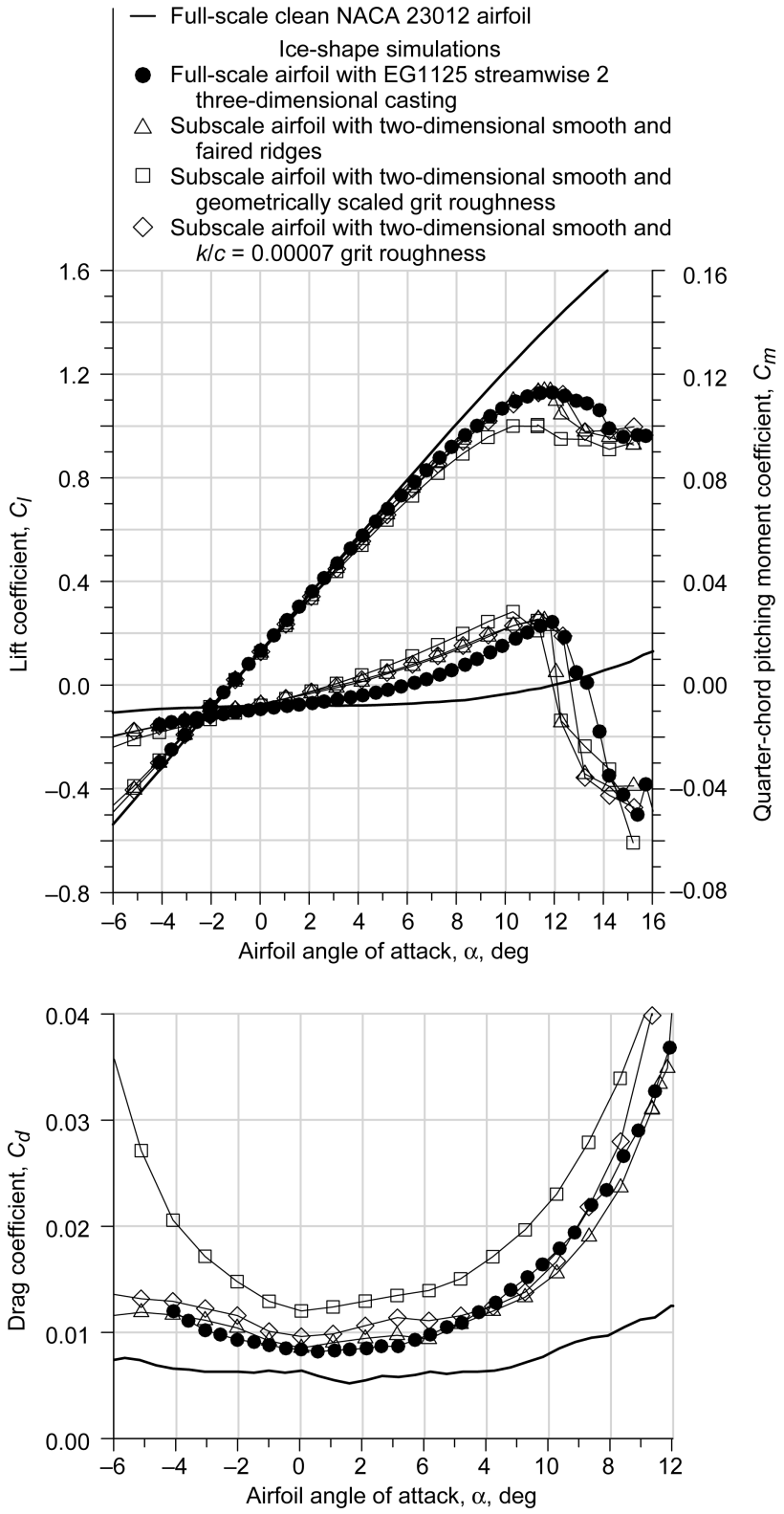

Figure 46.—Aerodynamic performance comparison of the EG1125 streamwise ice simulations with added roughness. Full-scale data were acquired at a Reynolds number of 15.9×10^6 and a Mach number of 0.20; subscale data were acquired at a Reynolds number of 1.8×10^6 and a Mach number of 0.18; *k*/*c*, roughness height per chord length.

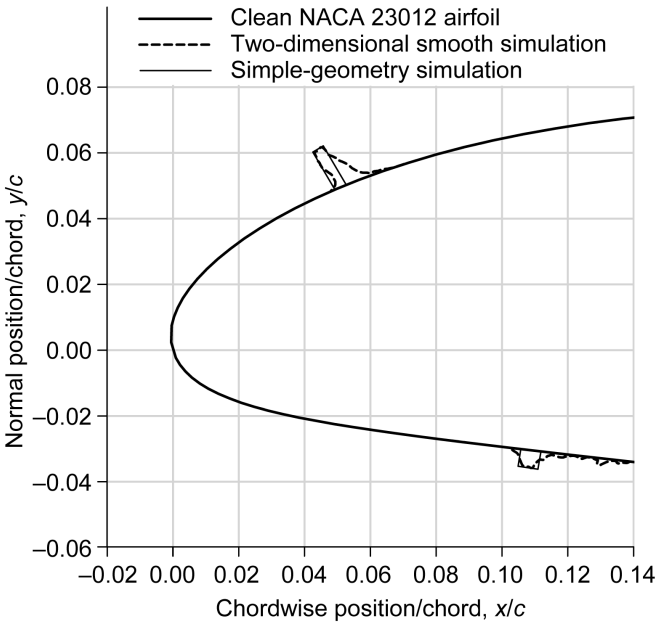

Figure 47.—Geometry comparison of two-dimensional smooth and simple-geometry simulations for EG1159 spanwise-ridge ice shape.

stall characteristics were slightly more benign relative to the full-scale, three-dimensional casting, and the former had slightly higher stalling angles. This is better illustrated by the stall break in the pitching-moment coefficient variation with angle of attack. The drag data indicated that the subscale simulations resulted in higher drag values up until about $\alpha = 3°$. This may have resulted from the fact that the ridge geometry of the three-dimensional casting had significant spanwise variation, particularly on the lower surface. As the angle of attack increased to stall, the lower surface ice geometry had less of an impact on the measured drag coefficient. Since the subscale simulations had more benign stall characteristics as observed in the lift and pitching moment, the relative change in drag coefficient was consistent. Overall, the two-dimensional smooth simulation matched more closely the drag coefficient of the three-dimensional casting.

The effectiveness of these subscale simulations is summarized in Table 19 in terms of $C_{l,\max}$, α_{stall}, and $\Delta C_{d,rms}$. The data for the two-dimensional smooth and simple-geometry ice shapes are very similar to that presented in Table 11 for the horn ice shape. The two-dimensional smooth simulation provided better overall matching in terms of the three parameters, but with slightly nonconservative results for $C_{l,\max}$ and α_{stall}. The simple-geometry case was not as accurate of a simulation, but it provided conservative estimates for $C_{l,\max}$ and C_d. Busch et al. (Refs. 44 and 62) did experiment with applying grit roughness to the two-dimensional smooth simulation. The results are summarized in Table 19 for approximately geometrically scaled roughness applied to both the upper and lower surface ridges. Similar to what has been already been discussed, this resulted in more conservative estimates of $C_{l,\max}$ and C_d.

The minimal effect of the applied roughness was attributable to the main flowfield feature described in Phase I: the large separation bubble associated with the upper surface ridge at angles of attack preceding stall. An important aspect of accurate subscale simulation is the representation of such key flowfield features in addition to good comparisons in aerodynamic performance parameters. The presence of the upper surface separation bubble results in a distinct pressure signature as described in connection with Figure 10. This is further illustrated in Figure 49 for the full-scale, three-dimensional casting compared with the subscale two-dimensional smooth simulation at $\alpha = 3.1°$. The upper surface pressure data for the latter case had a higher suction plateau ($C_p \approx -1.5$), followed by a more rapid pressure recovery relative to the three-dimensional casting data. This indicates that the separation bubble generated by the upper surface ridge was likely smaller on the subscale model. The performance data were consistent with this observation, since at $\alpha = 3.1°$ the subscale two-dimensional smooth ice shape had a drag coefficient that was lower than for the three-dimensional casting, with stall being slightly delayed. The stall type in this case was that of thin airfoils, with the separation bubble increasing in size with increasing angle of attack. So, a smaller separation bubble implies an earlier stage in the stall progression. The size comparison of the separation bubble was further corroborated with surface-oil flow-visualization results.

TABLE 19.—EFFECTIVENESS OF EG1159 SPANWISE-RIDGE ICE SIMULATIONS ON THE SUBSCALE MODEL
[$C_{l,\max}$, maximum lift coefficient; α_{stall}, stalling angle; $\Delta C_{d,rms}$, root-mean-square percent difference in drag coefficient; α, angle of attack; k/c, ice roughness height per chord length.]

Simulation	Simulation $C_{l,\max}$ – casting $C_{l,\max}$	Simulation α_{stall} – casting α_{stall}, deg	$\Delta C_{d,rms}$, percent ($-4° \le \alpha \le 4°$)
Two-dimensional smooth	0.01 (2.1 percent)	0.5	11.4
Simple geometry	–0.02 (–4.6 percent)	0.4	20.0
Two-dimensional smooth with geometrically scaled roughness	–0.04 (–7.5 percent)	0.4	12.3

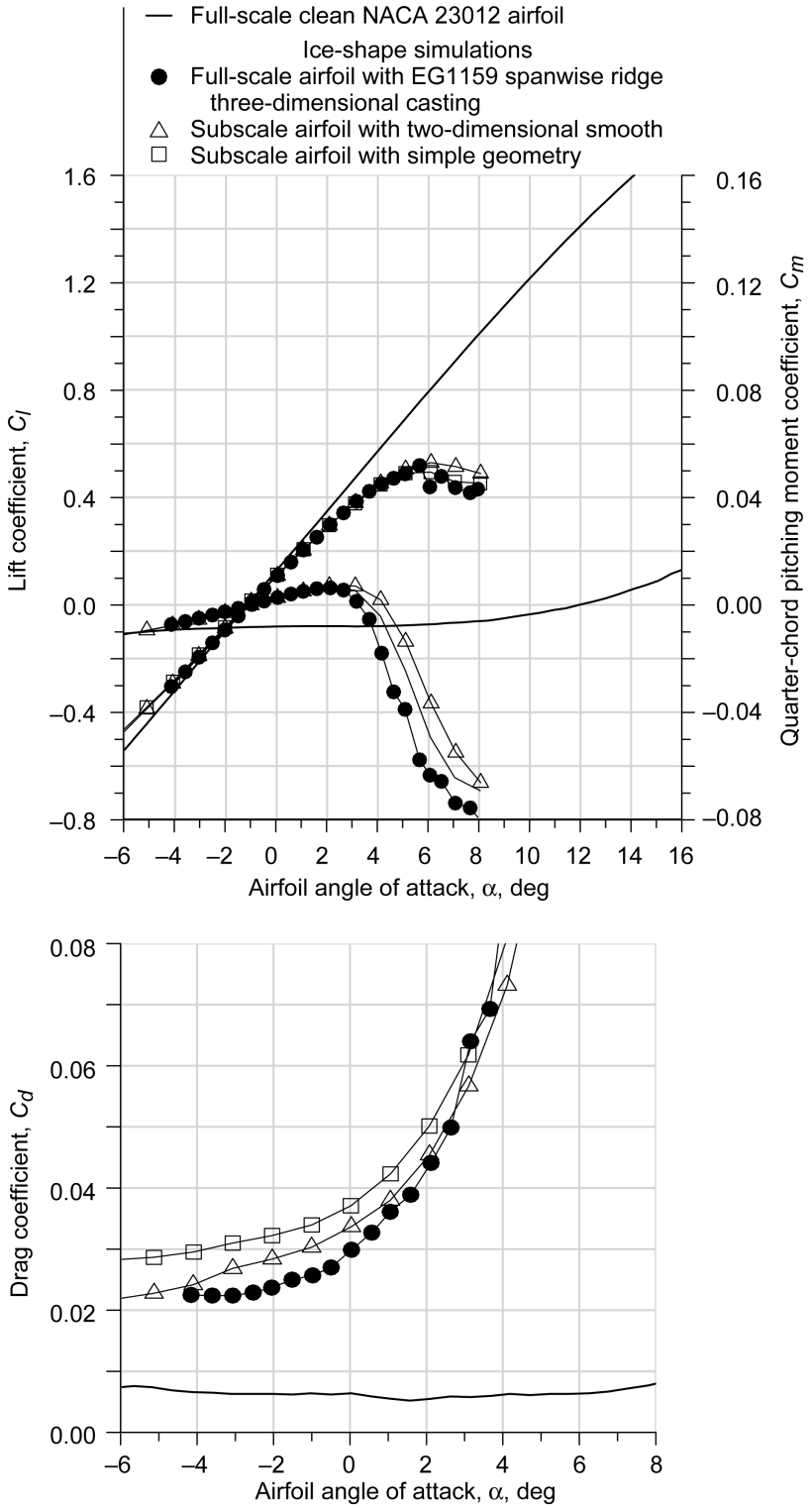

Figure 48.—Aerodynamic performance comparison of the EG1159 spanwise-ridge ice simulations. Full-scale data were acquired at a Reynolds number of 15.9×10^6 and a Mach number of 0.20; subscale data were acquired at a Reynolds number of 1.8×10^6 and a Mach number of 0.18.

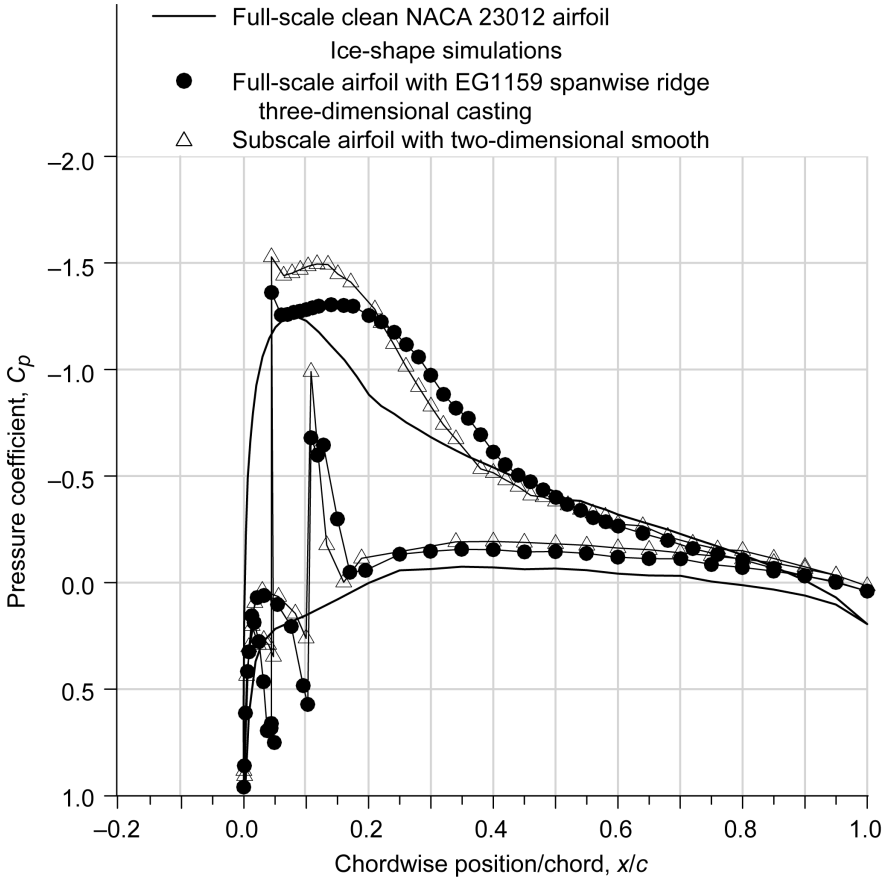

Figure 49.—Surface pressure distribution comparison of the EG1159 spanwise-ridge ice simulations at an angle of attack of 3.1°. Full-scale data were acquired at a Reynolds number of 15.9×10^6 and a Mach number of 0.20; subscale data were acquired at a Reynolds number of 1.8×10^6 and a Mach number of 0.18.

Busch et al. (Refs. 44 and 62) present and describe a comparison of flow-visualization images, one taken from the full-scale model testing in Phase V and one taken from the subscale model testing in Phase VI. Figure 50 compares these images, which were acquired at $\alpha = 3.1°$, corresponding to the pressure coefficient data in Figure 49. Since the full-scale model flow visualization was performed at atmospheric pressure, Re was reduced to 7.8×10^6 at M = 0.20. The effect of Reynolds number was so small in the iced-airfoil case, that it is likely that there was no significant change in the pressure data shown in Figure 49. In Figure 50(a), for the EG1159 three-dimensional casting on the full-scale model, flow is from left to right, with the casting visible on the far left of the image. The estimated mean separation bubble reattachment location has been highlighted and is positioned at approximately $x/c = 0.44$. Downstream of this line, the flow moved toward the airfoil trailing edge. Upstream of this line, the flow moved upstream, indicative of the recirculation region aft of the ridge. In Figure 50(b), for the two-dimensional smooth simulation on the subscale model, flow is also from left to right, with the upper surface ridge visible at the far left of the image. The estimated mean separation bubble reattachment location, which is highlighted in this image, was positioned at approximately $x/c = 0.33$. The subscale flowfield was qualitatively similar to the full-scale case with the recirculation region upstream of the mean reattachment location. The fact that the separation bubble was smaller in the subscale case is also consistent with the pressure data described in Figure 49. This provides some confidence that the subscale simulation was not only reasonable in terms of lift, pitching moment, and drag, but also in terms of the proper flowfield characteristics.

Unlike the spanwise-ridge ice shape considered in Phase III (i.e., ED0760), the present spanwise ridge (EG1159) definitely matched the "tall" ridge characteristics described in Phase I. The large separation bubble dominated the iced-airfoil aerodynamics, leading to stall at the lowest $C_{l,\max}$ and α_{stall} of all of the Phase V ice shapes. As a result, the subscale simulation proved to be very effective in reproducing the full-

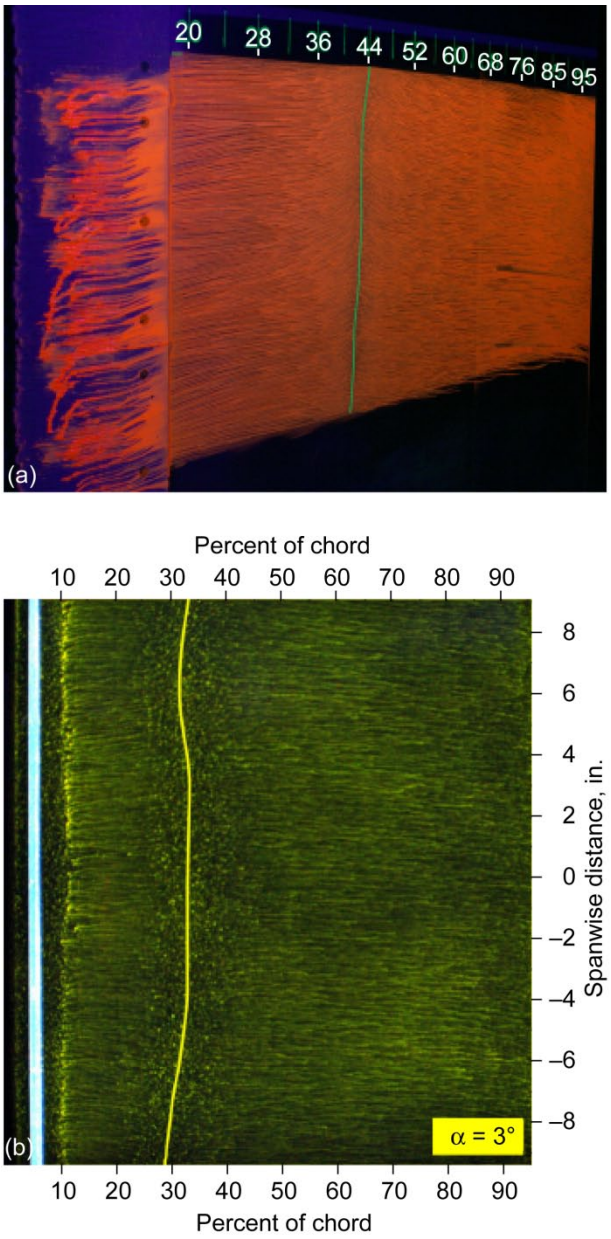

Figure 50.—Comparison of surface-oil flow visualization images of EG1159 spanwise-ridge ice simulations on the NACA 23012 airfoil at an angle of attack of 3.1°. Flow is from left to right with the approximate mean separation bubble reattachment location highlighted in each frame. (a) Full-scale, three-dimensional casting configuration at a Reynolds number of 7.8×10^6 and a Mach number of 0.20. (b) Subscale, two-dimensional smooth configuration at a Reynolds number of 1.8×10^6 and a Mach number of 0.18.

scale results. This explains why the simulation effectiveness listed in Table 19 is better than that listed in Table 6 for the Phase III spanwise ridge. As alluded to earlier, these results suggest that a subsclassification of spanwise-ridge ice shapes is needed as put forth by Broeren et al. (Refs. 32 and 33).

8.3 Summary of Simulation Effectiveness for Phase VI

The ice-accretion simulation methods developed in Phase III were used here in Phase VI to determine the accuracy to which the full-scale, high-Reynolds number iced-airfoil aerodynamics could be obtained on the subscale model at low-Reynolds number. In all cases the performance of the NACA 23012 airfoil with the full-scale, three-dimensional casting simulations from Phase V was taken as the benchmark, and all other results were compared to it. The aerodynamic data were summarized in Table 11, Table 14, and Table 16 to Table 19 for each of the ice shapes tested in Phase VI. Following the method of Busch et al. (Refs. 44 and 62), the effectiveness of the geometrically scaled simulations of each of the six Phase V ice shapes was compiled in Table 20. The geometrically scaled simulations were selected for comparison because these were designed without any a priori knowledge of the full-scale aerodynamics. Thus, these results account for uncertainties in geometric simulation fidelity, model scale, and Reynolds number.

The combined experimental uncertainty in lift coefficient from the subscale and full-scale experiments can be estimated from the data provided in Table 2 and Table 10. The uncertainty in the subscale experiments was very small, ±0.00019 (see Table 2). For the full-scale experiments, the C_l uncertainty was approximately a factor of 2 smaller than the value of ±0.01 shown in Table 10 because of the increased dynamic pressure at $\mathrm{Re} = 15.9\times10^6$ and $\mathrm{M} = 0.20$. Therefore, the combined experimental uncertainty in C_l was approximately ±0.005. According to Table 20, the simulation effectiveness in terms of $C_{l,\max}$ was larger than the experimental uncertainty for all of the ice shapes. The experimental uncertainty was potentially a significant contribution for only the EG1159 ice shape. This means that the primary source of simulation uncertainty (or simulation ineffectiveness) in $C_{l,\max}$ was likely due to the infidelities in the geometric representation and Reynolds number effects. Even though Reynolds number effects on $C_{l,\max}$ have been shown to be small—the lower limit of Reynolds number in the full-scale model tests was $\mathrm{Re} = 4.5\times10^6$ to 4.7×10^6—it is difficult to estimate the amount of simulation uncertainty in $C_{l,\max}$ due to Reynolds number variations down to $\mathrm{Re} = 1.8\times10^6$ used in the subscale testing.

TABLE 20.—SUMMARY OF SIMULATION EFFECTIVENESS FOR GEOMETRICALLY SCALED SIMULATIONS FOR EACH OF THE FULL-SCALE MODEL THREE-DIMENSIONAL CASTINGS

[Re, Reynolds number; M, Mach number; $C_{l,\max}$, maximum lift coefficient; α_{stall}, stalling angle; $\Delta C_{d,rms}$, root-mean-square percent difference in drag coefficient; α, angle of attack; k/c, ice roughness height per chord length.]

Ice shape of full-scale, three-dimensional casting (Re = 15.9×10^6, M = 0.20)		Geometrically scaled simulation (Re = 1.8×10^6, M = 0.20)	Simulation $C_{l,\max}$ – casting $C_{l,\max}$	Simulation α_{stall} – casting α_{stall}, deg	$\Delta C_{d,rms}$, percent (linear α range)
Classification	Configuration				
Horn	EG1164	Two-dimensional smooth	0.03 (2.9 percent)	1.0	10.3
Roughness 1	EG1126	Approximately geometrically scaled (see Table 12)	–0.04 (–3.5 percent)	–1.0	28.6
Roughness 2	EG1134	k/c = 0.0003 roughness with EG1126 extents	–0.19 (–15.0 percent)	–1.7	16.4
Streamwise 1	EG1162	Two-dimensional smooth with k/c = 0.0013 roughness	–0.14 (–11.8 percent)	–1.6	28.8
Streamwise 2	EG1125	Two-dimensional smooth with geometrically scaled roughness	–0.13 (–11.1 percent)	–0.6	46.3
Spanwise ridge	EG1159	Two-dimensional smooth	0.01 (2.1 percent)	0.5	11.4

The simulation effectiveness in terms of α_{stall} for all of the ice shapes was an order of magnitude larger than for the combined experimental uncertainty for both the subscale and full-scale experiments (see Table 2 and Table 10). However, the angle-of-attack resolution at which the data were acquired may play a larger role. Generally this was 0.5° for the full-scale data and 1.0° for the subscale data. So $\alpha < 1.0°$ in Table 20 could be due to a combination of all effects: angle-of-attack resolution, experimental uncertainty, and simulation uncertainty. Only the EG1134 and EG1162 configurations had absolute $\alpha_{stall} > 1.0°$ in Table 20. Depending on the objective of scaled simulation experiments, these kinds of differences in stalling angle may be acceptable. Often the character of the stall behavior (e.g., abrupt stall vs. gradual stall), may be more important than the exact values of stalling angle of attack. Such metrics are unfortunately difficult to quantify and summarize in tables.

For the comparisons of $\Delta C_{d,rms}$ in Table 20, determining the individual contribution due to experimental uncertainty is nontrivial. There is the added uncertainty because potential spanwise variations in drag were not quantified. However, visual inspection of the drag comparison plots has shown that $\Delta C_{d,rms} \le 10$ percent represents a reasonable simulation of drag performance over the linear range. For the six ice shapes in Table 20, only two—EG1162 and EG1159—had $\Delta C_{d,rms}$ values close to 10 percent. There was a large range among the others. As described in the previous discussions, drag coefficient is affected by the simulation details, such as roughness size, concentration, and location. Clearly, high-fidelity simulations and more closely matched Reynolds numbers are required for a more accurate drag coefficient simulation.

Busch et al. (Refs. 44 and 62) also used as a basis for comparison the subscale simulations that were constructed to best match the full-scale aerodynamics. These were labeled "most-accurate" simulations and are listed in Table 21. For the EG1164 and EG1159 shapes, the most-accurate simulation was the two-dimensional smooth, geometrically scaled simulation. For these ice shapes, the dominate driver of the iced-airfoil aerodynamics was the large separation bubble emanating from the horn (EG1164) or spanwise ridge (EG1159). The geometric details of the ice shape and roughness did not play a primary role in the resulting aerodynamic performance. For the other four ice shapes (EG1126, EG1134, EG1162, and EG1125), there were significant improvements in the simulation effectiveness relative to the geometrically scaled simulations summarized in Table 20. In terms of $C_{l,\max}$, the simulation uncertainty (see Table 21) was still larger than the combined experimental uncertainty (±0.005), indicating that geometry and Reynolds number effects played a role. The opposite was true in terms of α_{stall}, where the simulation uncertainty (see Table 21) was less than the angle-of-attack resolution used in acquiring the data. Significant improvements in $\Delta C_{d,rms}$ were also observed. These data for the "most-accurate" simulations provide a lower limit of the total simulation uncertainty that is realistically achievable over this range of model scale and Reynolds number. It is interesting to note that the some of the values in Table 21 were larger than the values in Table 7. (There were some notable exceptions, particularly in terms of α_{stall}.) These differences were at least partly attributable to model scale and Reynolds number effects.

TABLE 21.—SUMMARY OF SIMULATION EFFECTIVENESS FOR MOST-ACCURATE SUBSCALE SIMULATIONS FOR EACH OF THE FULL-SCALE MODEL THREE-DIMENSIONAL CASTINGS

[Re, Reynolds number; M, Mach number; $C_{l,\max}$, maximum lift coefficient; α_{stall}, stalling angle; $\Delta C_{d,rms}$, root-mean-square percent difference in drag coefficient; α, angle of attack; k/c, ice roughness height per chord length.]

Ice shape of full-scale, three-dimensional casting (Re = 15.9×10^6, M = 0.20)		Most accurate subscale simulation (Re = 1.8×10^6, M = 0.20)	Simulation $C_{l,\max}$ – casting $C_{l,\max}$	Simulation α_{stall} – casting α_{stall}, deg	$\Delta C_{d,rms}$, percent (linear α range)
Classification	Configuration				
Horn	EG1164	Two-dimensional smooth	0.03 (2.9 percent)	1.0	10.3
Roughness 1	EG1126	k/c = 0.0003 roughness with casting extents[a]	–0.01 (–0.6 percent)	–0.1	19.4
Roughness 2	EG1134	k/c = 0.00007 roughness	0.02 (1.5 percent)	–0.1	7.8
Streamwise 1	EG1162	Two-dimensional smooth with k/c = 0.0003 roughness	0.03 (2.8 percent)	0.1	10.3
Streamwise 2	EG1125	Two-dimensional smooth with faired ridges	0.01 (0.6 percent)	–0.3	8.9
Spanwise ridge	EG1159	Two-dimensional smooth	0.01 (2.1 percent)	0.5	11.4

[a]Chordwise extent of roughness over the casting.

9.0 Subscale Iced-Airfoil Aerodynamic Simulation Methodology

The objectives of this study as presented in the Introduction were to provide high-fidelity, full-scale, iced-airfoil aerodynamic data and validated subscale simulation methods that produce the essential full-scale aerodynamic characteristics. Busch (Ref. 62) presents the following method where the subscale Re = 1.8×10^6 and the model scale is one-fourth of the full-scale geometry. This analysis was based on the results of Phase VI together with the current understanding of iced-airfoil flowfield characteristics described in this report and in more detail by Busch (Ref. 62). It is anticipated that these methods should provide results within the accuracies presented (see Table 20) for scales and Reynolds numbers at least to these levels. The following was adapted from Busch (Ref. 62).

(1) Given the ice accretion to be simulated, classify it as ice roughness, streamwise ice, horn ice, or tall or short spanwise-ridge ice.
(2) For the appropriate classification, document the ice-shape geometric features that have been identified as having a significant effect on the iced-airfoil flowfield. The size, shape, location, and other attributes of these important features may be quantified from icing-tunnel tests, flight-tests, computational methods like LEWICE, or other sources.
(3) Depending on the ice-shape type, construct simple-geometry or two-dimensional smooth simulations that geometrically scale the gross ice geometry.
(4) For shapes in which roughness is important, add geometrically scaled grit roughness of the appropriate concentration. This was shown to generally yield conservative performance estimates. To bracket the "true" iced-airfoil performance, the authors recommend that the simulation be tested both with and without the grit roughness.

Each type of iced-airfoil flowfield is different and is, thus, affected by different geometric features. The following summaries identify these features on the basis of the aerodynamics for each of the known ice-accretion types. After the geometric features have been determined, steps (2) to (4) can be completed.

9.1 Ice Roughness

Roughness elements on the airfoil leading edge often cause regions of localized separation, increasing skin friction and extraction of momentum from the flow, and may cause the boundary layer to undergo early transition, causing premature trailing-edge stall, reduced maximum lift coefficient, and increased drag coefficient. Therefore, it is important for an ice-roughness simulation to reproduce these effects at each angle of attack in the range of interest. Geometric features that affect the iced-airfoil performance are roughness height, concentration, location, and chordwise extent. Roughness height affects both airfoil maximum lift coefficient and drag coefficient. As roughness height increases (for constant roughness concentration, location, and chordwise extent), $C_{l,\max}$ decreases and C_d increases. The maximum lift coefficient is most sensitive to changes in roughness height for very small heights and becomes less sensitive at larger heights. Roughness concentration also affects airfoil maximum lift coefficient and drag coefficient. As roughness concentration increases, $C_{l,\max}$ decreases up to a critical concentration (which depends on roughness height), beyond which $C_{l,\max}$ becomes much less sensitive to changes in concentration. As roughness concentration increases, C_d increases, even beyond the critical concentration at which $C_{l,\max}$ becomes insensitive. Roughness extent affects mainly the drag coefficient, but large changes may affect the maximum lift coefficient. Decreases in chordwise extent of only a few percent chord caused measurable reductions in iced-airfoil C_d. Multiple combinations of roughness height and concentration may

provide accurate modeling of iced-airfoil aerodynamics over an angle-of-attack range.

9.2 Streamwise Ice

A short separation bubble often forms because of discontinuities in the ice geometry or at the interface between the ice and airfoil. This separation bubble removes momentum from the reattached boundary layer, increasing the likelihood of early separation. Therefore, it is important for a subscale simulation to generate a short separation bubble of similar size at a similar location, which requires a modification of the airfoil leading-edge geometry. To model the maximum lift coefficient, this modification does not have to exactly match that of the original ice shape as long as an appropriate separation bubble is generated. Further compounding the effect of the short separation bubble is the presence of roughness on the ice, which acts in a manner similar to that described for ice roughness. Accordingly, it is important to represent the height, concentration, location, and extent of surface roughness on streamwise ice. Streamwise ice may also be more three-dimensional than other types of ice shapes because of the presence of ice feathers and nodules. If one uses a two-dimensional smooth simulation to model the iced-airfoil aerodynamics, these features should not be included in the geometry used to make the simulation since they would be extruded into two-dimensional ridgelike features, causing a different effect on the flowfield than did the feathers on the original ice shape.

9.3 Horn Ice

The horn ice flowfield is dominated by a long separation bubble generated from the tip of the horn. The aerodynamics of a horn ice shape can be accurately modeled by reproducing the size of this separation bubble and the point at which separation occurs. Features shown to affect the size of the separation bubble and the airfoil maximum lift and drag coefficients are horn height, location, angle, and sometimes tip radius. With all other parameters equal, for horns located on the upper surface of the airfoil, increasing horn height usually reduces $C_{l,\max}$ and increases C_d because of the larger separation bubble. Horns located farther aft and with greater angles, up to 90°, also tend to cause larger aerodynamic penalties than those located closer to the leading edge and with lower angles. Surface roughness does not usually have a large effect on the separation bubble size, and it does not need to be included in a horn ice simulation.

9.4 Tall Spanwise-Ridge Ice

Tall spanwise-ridge ice is similar to horn ice in that the flowfield is dominated by a long separation bubble, but it is different in that the boundary layer develops upstream of the ice shape. As with horn ice, it is important to properly represent the long separation bubble generated by the ridge. However, because the boundary layer has formed on the airfoil surface prior to reaching the ridge, surface roughness located upstream of and on the ridge is important to represent as well. Roughness downstream of the ridge, located in the separation bubble, does not have a significant effect on airfoil performance. Ridge features affecting the airfoil maximum lift and drag coefficients are height, location, and surface roughness upstream of the separation point. Increasing ridge height causes a larger separation bubble, reduces airfoil $C_{l,\max}$, and increases C_d. Ridges on the upper surface between the locations of maximum local air velocity (minimum C_p) and maximum adverse pressure gradient of the clean airfoil cause the largest reductions in $C_{l,\max}$, and ridges located near the clean airfoil maximum local air velocity (minimum C_p) cause the largest increases in C_d. The addition of surface roughness decreased $C_{l,\max}$ and increased C_d at most angles of attack.

9.5 Short Spanwise-Ridge Ice

Short spanwise-ridge ice shapes generate short separation bubbles, rather than the long bubbles generated by tall spanwise-ridge ice, and have only a local effect on the airfoil C_p distribution. It is important for a subscale simulation to appropriately represent this separation bubble, and ridge height, location, and geometry have all been shown to be important. Airfoil $C_{l,\max}$ decreases and C_d increases with increasing ridge height for a given location or for more forward locations and a given height. The geometry of the ridge also affects airfoil aerodynamics because different-shaped simulations of identical height and location may yield different performance penalties. As with tall ridges, the boundary layer develops upstream before reaching the short ridge, and surface roughness was shown to have a significant effect on both $C_{l,\max}$ and C_d. The addition of surface roughness caused conservative estimates of aerodynamic performance and worsened simulation accuracy. This may have been due, in part, to Reynolds number effects because no data exist regarding Reynolds number effects in the range $1.8\times10^6 \le \mathrm{Re} \le 4.6\times10^6$ and because effects above $\mathrm{Re} = 4.6\times10^6$ have been shown to be small. More research is required to further develop the short-ridge aerodynamic characteristics.

10.0 Summary, Conclusions, and Recommendations

10.1 Summary

This report presents the results of a six-phase research program designed to study the aerodynamic scaling and simulation of ice accretion on airfoils. The overall goal of this program was to determine the level of geometric fidelity required for artificial ice shapes to yield aerodynamic performance results to within a known level of uncertainty,

thus attempting to answer the question, "How good is good enough?" The research program was organized into six phases, employing both subscale and full-scale model testing. It was important to have a set of full-scale benchmark data and firm knowledge of the full-scale phenomena. This information provided validation data for both the subscale testing and scaling methods developed.

In Phase I: Ice-Shape Classification, previous research was analyzed to classify ice shapes according to the fundamental flowfield physics. Four types of ice were defined: roughness, horn, streamwise, and spanwise ridge. For horn and spanwise-ridge shapes, the flowfield was characterized by a large separation bubble that grew in size with increasing angle of attack. The separation bubble was the dominant flowfield feature contributing to the stall of the iced airfoil. For roughness and streamwise ice, the flow was characterized by local flow separation on the scale of the roughness, but this was not largely affected by angle-of-attack changes. Instead, the aerodynamic effect of these shapes was manifested through the boundary layer such that there was a greater tendency for trailing-edge separation at lower angles of attack for the iced airfoil. There were other important differences among these four types as described in this report. It was these key flowfield features that affected the scaling and simulation carried out in this research and that guided the experiments. Since each of the four types has different fundamental aerodynamics, if techniques can be developed to simulate these four shapes, then most ice accretions can be simulated.

The objective of Phase II: Subscale-Model Ice-Accretion Testing was to obtain high-fidelity ice shapes for the subscale model having the characteristics developed in Phase I. Ice-accretion testing was conducted in the NASA Icing Research Tunnel (IRT) using an 18-in.- (0.46-m-) chord, two-dimensional wing section with an NACA 23012 airfoil profile. Icing conditions were based on the in-flight icing environment that a commuter aircraft might encounter. For selected cases, molds were acquired of the ice accreted on the model under these conditions. Castings were then made from these molds and used as the high-fidelity ice shapes for the tests in Phase III. The purpose here was not to produce scaled ice-accretion geometry but to generate ice accretions that were representative of the four ice classifications to use for aerodynamic simulation development in Phase III.

In Phase III: Subscale-Model Aerodynamic Testing, the high-fidelity ice shapes obtained in Phase II were used to develop aerodynamic simulation methods on the subscale model. Aerodynamic testing was performed in the University of Illinois wind tunnel using an 18-in.- (0.46-m-) chord two-dimensional wing section with NACA 23012 airfoil profile. Airfoil performance was measured at Reynolds number $\mathrm{Re} = 1.8\times10^6$ and Mach number $\mathrm{M} = 0.18$ with artificial ice shapes having various levels of simulation fidelity. The three-dimensional casting simulation was made from a mold of the IRT ice accretion, had the highest geometric fidelity, and was considered to result in the "true" iced-airfoil aerodynamics. Lower fidelity simulations such as two-dimensional smooth and simple geometry were developed to quantify the resulting aerodynamic effect. The ability of the lower fidelity simulations to reproduce the aerodynamics of the airfoil with the three-dimensional casting simulation was quantified in terms of lift, drag, and pitching-moment coefficient (C_l, C_d, and C_m) versus angle of attack (α). In addition, surface pressure distributions and surface-oil flow visualizations were compared. It was important that the lower fidelity simulations reproduce the fundamental flowfield features as well as the integrated performance coefficients. The effectiveness of the most accurate lower fidelity simulation method for each of the four ice-shape types was summarized in Table 7 in terms of $C_{l,\max}$, α_{stall}, and root-mean-square difference in drag coefficient between the lower fidelity simulation and the three-dimensional casting simulation over a given angle-of-attack range $\Delta C_{d,\text{rms}}$. The simulation accuracy ranged from 0.2 to –3.7 percent in $C_{l,\max}$, 0.00° to –1.98° in α_{stall}, and 4.8 to 15.5 percent in $\Delta C_{d,\text{rms}}$. The Phase III results quantified the simulation effectiveness for various levels of fidelity on the subscale model. These simulation methods were then applied to Phase VI of the program.

The objective of Phase IV: Full-Scale-Model Ice-Accretion Testing was to obtain high-fidelity ice shapes for the full-scale model having the characteristics developed in Phase I. Ice-accretion testing was conducted in the NASA IRT using a 72-in.- (1.83-m-) chord, two-dimensional wing section with an NACA 23012 airfoil profile. Test conditions for the full-scale icing tests were selected as indicated in Phase II: that is, icing conditions that a commuter aircraft might encounter in flight, as defined by icing conditions in Appendix C of Code of Federal Regulations (CFR) Part 25, and that would yield an ice accretion falling within the four ice classifications described in Phase I. For selected cases, molds were acquired of the ice accreted on the model under these conditions. Castings were then made from these molds and used as the high-fidelity ice shapes for the tests in Phase V.

In Phase V: Full-Scale Model Aerodynamic Testing, the ice shapes acquired in Phase IV were used for aerodynamic testing on the full-scale model to obtain a benchmark data set for the validation of subscale simulation methods. Aerodynamic testing was performed in the ONERA F1 wind-tunnel using a 72-in.- (1.83-m-) chord, two-dimensional wing section with an NACA 23012 airfoil profile. Airfoil performance was measured from $\mathrm{Re} = 4.5\times10^6$ to 15.9×10^6 and $\mathrm{M} = 0.10$ to 0.28 with high-fidelity, three-dimensional casting simulations attached to the model. Six ice-shape simulations were tested: one horn shape, one spanwise-ridge shape, two streamwise shapes, and two roughness shapes. The artificial ice shapes had a large detrimental effect on the performance of the NACA 23012 airfoil. The spanwise-ridge shape caused the largest reduction in maximum lift, with $C_{l,\max} = 0.52$ compared to the clean value of $C_{l,\max} = 1.85$ at $\mathrm{Re} = 15.9\times10^6$ and

M = 0.20. The two roughness and streamwise ice simulations had a similar range of performance effects on the airfoil. At Re = 15.9×10^6 and M = 0.20, the range of $C_{l,\max}$ was 1.09 to 1.28 and the range of minimum C_d was 0.0082 to 0.0106. The range of performance effects was small relative to the large differences in the size and geometry of the roughness and streamwise ice shapes tested.

The pressurization capability of the ONERA F1 facility was used to document the effects of Reynolds and Mach numbers on the clean and iced performance. The clean airfoil $C_{l,\max}$ increased from 1.76 to 1.88 as Re increased from 4.6×10^6 to 12.3×10^6 at constant M = 0.10. Increasing M from 0.10 to 0.28 at a constant Re = 12.1×10^6 reduced $C_{l,\max}$ from 1.88 to 1.78. The trends in lift and moment slope versus angle of attack and drag coefficient were consistent with classic airfoil behavior. For the airfoil with the ice simulations, there was virtually no measurable change in maximum lift coefficient over the entire Reynolds number range tested. Changes in Mach number had minor effects on maximum lift for the horn and spanwise-ridge shapes, but virtually no effects for the others. This lack of significant Reynolds and Mach number effects was important to Phase VI, the subsequent subscale-model simulation.

In Phase VI: Simulation Validation Testing, the methods developed in Phase III were used to scale and simulate the full-scale ice shapes for testing on the subscale model at lower Reynolds numbers. The objective of this phase was to "close the loop" by using the subscale-model data to reproduce the aerodynamic effects of the ice shapes tested on the full-scale model at high Reynolds numbers. Aerodynamic testing was again performed in the University of Illinois wind tunnel using the 18-in.-chord NACA 23012 airfoil model at Re = 1.8×10^6 and M = 0.18. Scaled, lower fidelity simulations of the three-dimensional ice casting configurations from Phase V were developed and tested on the subscale model. As in Phase III, the ability of the lower fidelity simulations to reproduce the aerodynamics of the airfoil with the three-dimensional casting simulation was quantified in terms of lift, drag, and pitching-moment coefficient versus angle of attack. Surface pressure distributions and surface-oil flow visualizations were also compared. It was important that the lower fidelity simulations reproduced the fundamental flowfield features as well as the integrated performance coefficients.

The effectiveness of the geometrically scaled, lower fidelity simulations for each of the six ice shapes was summarized in Table 20 in terms of $C_{l,\max}$, α_{stall}, and $\Delta C_{d,\mathrm{rms}}$. The simulation accuracy ranged from 2.1 to –15.0 percent in $C_{l,\max}$, 1.0° to –1.7° in α_{stall}, and 10.3 to 46.3 percent in $\Delta C_{d,\mathrm{rms}}$. Note that this range of simulation accuracy was much larger than what was obtained in Phase III. These results account for uncertainties in geometric simulation fidelity, model scale, and Reynolds number. The results for the geometrically scaled simulations represent typical methods used without any knowledge of the full-scale iced-airfoil aerodynamics. Scaled, lower fidelity simulations also were constructed to imitate the full-scale aerodynamics as closely as possible. The effectiveness of these simulations, which was summarized in Table 21, ranged from 2.9 to –0.6 percent in $C_{l,\max}$, 1.0° to –0.3° in α_{stall}, and 7.8 to 19.4 percent in $\Delta C_{d,\mathrm{rms}}$. These data for the "most-accurate" simulations provide a lower limit of the total simulation uncertainty that is realistically achievable over this range of model scale and Reynolds number.

10.2 Conclusions

This program has resulted in a systematic framework for conducting the aerodynamic analysis of iced airfoils on subscale models at low Reynolds numbers. An ice-accretion classification system based on flowfield physics was developed and used to guide the experiments. Methodologies were then developed for defining various levels of geometric fidelity for ice-shape simulations on the basis of the classification. The aerodynamic fidelity of the ice-shape simulations was first quantified through subscale-model iced-airfoil performance. High-quality aerodynamic data were generated for high-fidelity, ice-casting simulations on a full-scale model at high Reynolds numbers. This provided a benchmark database that is directly applicable to airplanes. The Reynolds and Mach number effects on clean- and iced-airfoil performance were also quantified. Thus, the combined results of the full-scale and subscale-model experiments quantified the uncertainty associated with various levels of geometric ice-shape fidelity in terms of lift and drag for a factor of 4 in model scale and a factor of 8 in Reynolds number. The lower limit for these results is Re = 1.8×10^6, and it is likely that more significant aerodynamic effects will occur for even lower Reynolds numbers. Geometric scaling of gross ice-shape features is appropriate for horn ice, streamwise ice, and spanwise-ridge ice. For roughness and streamwise ice, the details of roughness are important for accurate aerodynamic simulation. For horn ice, any roughness details may be important for accurate drag simulation but not for lift. These results showed that geometric scaling of roughness will likely result in conservative performance penalties and thus more accurate roughness simulation requires a different length scale. These conclusions can be directly related to the key flowfield features that govern the iced-airfoil aerodynamics for the four types of ice shapes. This work culminated in the proposed methodology for subscale iced-airfoil aerodynamic simulation described in this report.

10.3 Recommendations

This study addressed a large number of important factors regarding subscale simulation of icing aerodynamics effects. This was accomplished primarily in terms of maximum lift, stalling angle, and drag using an NACA 23012 airfoil. More detailed study of the simulation methods and accuracy in terms of pitching moment and control surface forces and moment is

recommended since these can also be important in some cases. It is also known that the stalling characteristics can be equally important to maximum lift coefficient and stalling angle. Subscale simulation should be evaluated in terms of these effects as well. The effect of airfoil geometry should be considered in future work. Finally, an analogous research program should be implemented for three-dimensional swept wings to better understand how these two-dimensional airfoil data relate to swept-wing aircraft configurations.

Glenn Research Center
National Aeronautics and Space Administration
Cleveland, Ohio, February 17, 2011

References

1. Brown, A.P.: AIRS II Flight Determination of Turboprop Transport Aeroplane Lift, Drag and Propulsive Efficiency Effects in Freezing Drizzle Icing. AIAA 2004–4949, 2004.
2. Brown, Anthony P.: Analysis of the Aerodynamic Effects of Freezing Drizzle Inflight Icing on a Turboprop Aircraft. AIAA–1999–3151, 1999.
3. Ashenden, Russell; and Marwitz, John: Characterizing the Supercooled Large Droplet Environment with Corresponding Turboprop Aircraft Response. J. Aircraft, vol. 35, no. 6, 1998, pp. 912–920.
4. Miller, Dean, et al.: NASA/FAA/NCAR Supercooled Large Droplet Icing Flight Research: Summary of Winter 1996–1997 Flight Operations. NASA/TM—1998-206620 (AIAA 98–0577), 1998.
5. Ashenden, Russell; and Marwitz, John D.: Turboprop Aircraft Performance Response to Various Environmental Conditions. J. Aircraft, vol. 34, no. 3, 1997, pp. 278–287.
6. Ranaudo, R.J., et al.: The Measurement of Aircraft Performance and Stability and Control After Flight Through Natural Icing Conditions. AIAA–1986–9758, 1986.
7. Ranaudo, R.J., et al.: Performance Degradation of a Typical Twin Engine Commuter Type Aircraft in Measured Natural Icing Conditions. NASA TM–83564 (AIAA–1984–179), 1984.
8. Addy, Harold E., Jr.; and Lee, Sam: Icing Encounter Duration Sensitivity Study. AIAA 2009–4263, 2009.
9. Reehorst, Andrew L.; and Richter, G. Paul: New Methods and Materials for Molding and Casting Ice Formations. NASA TM–100126, 1987.
10. Broeren, Andy P.; Bragg, Michael B.; and Addy, Harold E., Jr.: Effect of Intercycle Ice Accretions on Airfoil Performance. J. Aircraft, vol. 41, no. 1, 2004, pp. 165–174.
11. Addy, Harold E., Jr., et al.: A Wind Tunnel Study of Icing Effects on a Business Jet Airfoil. NASA/TM—2003-212124 (AIAA 2003–0727), 2003.
12. Papadakis, Michael, et al.: Aerodynamic Performance of a Swept Wing with Ice Accretions. AIAA 2003–731, 2003.
13. Gile Laflin, Brenda E.; and Papdakis, Michael: Experimental Investigation of Simulated Ice Accretions on a Natural Laminar Flow Airfoil. AIAA 2001–0088, 2001.
14. Gregorek, Gerald; Dresse, John J.; and LaNoe, Karine: Additional Testing of the DHC–6 Twin Otter Tailplane Iced Airfoil Section in the Ohio State University 7×10 Low Speed Wind Tunnel. NASA/CR—2000-209921/VOL2, 2000.
15. Addy, Harold E., Jr.; and Chung, James J.: A Wind Tunnel Study of Icing Effects on a Natural Laminar Flow Airfoil. AIAA–2000–0095, 2000.
16. Papdakis, Michael, et al.: Experimental Investigation of Simulated Ice Accretions on a Full-Scale T-tail. AIAA 2001–0090, 2001.
17. Addy, Harold E., Jr.: Ice Accretions and Icing Effects for Modern Airfoils. NASA/TP—2000-210031 (DOT/FAA/AR–99/89), 2000.
18. Anderson, David N.: Manual of Scaling Methods. NASA/CR—2004-212875, 2004.
19. Lynch, Frank T.; and Khodadoust, Abdollah: Effects of Ice Accretions on Aircraft Aerodynamics. Prog. Aerosp. Sci., vol. 37, no. 8, 2001, pp. 669–767.
20. Busch, Greg T.; and Bragg, Michael B.: Experimental Study of Full-Scale, Iced-Airfoil Aerodynamic Performance Using Sub-Scale Simulations. AIAA 2009–4264, 2009.
21. Bragg, M., et al.: Airfoil Ice-Accretion Aerodynamics Simulation. AIAA 2007–85, 2007.
22. Bragg, M.B.; Broeren, A.P.; and Blumenthal, L.A.: Iced-Airfoil and Wing Aerodynamics. SAE Paper 2003–01–2098, 2003.
23. Bragg, M.B.; Broeren, A.P.; and Blumenthal, L.A.: Iced-Airfoil Aerodynamics. Prog. Aerosp. Sci., vol. 41, no. 5, 2005, pp. 323–362.
24. Bragg, M.B.; and Gregorek, G.M.: Environmentally Induced Surface Roughness Effects on Laminar Flow Airfoils: Implications for Flight Safety. AIAA Paper 89–2049, 1989.
25. Papadakis, Michael, et al.: Aerodynamic Scaling Experiments With Simulated Ice Accretions. AIAA–2001–833, 2001.
26. Papadakis, Michael; Alansatan, Sait; and Yeong, Hsiung W.: Aerodynamic Performance of a T-Tail With Simulated Ice Accretions. AIAA–2000–363, 2000.
27. Busch, Greg; Broeren, Andy; and Bragg, Michael: Aerodynamic Simulation of a Horn-Ice Accretion on a Subscale Model. AIAA 2007–87, 2007.
28. Busch, G.T.; Broeren, A.; and Bragg, M.: Aerodynamic Simulation of a Horn-Ice Accretion on a Subscale Model. J. Aircraft, vol. 45, no. 2, 2008, pp. 604–613.
29. Bragg, M.B.; and Khodadoust, A.: Experimental Measurements in a Large Separation Bubble Due to a Simulated Glaze Ice Shape. AIAA–1988–116, 1988.
30. Broeren, Andy; Bragg, Michael; and Addy, Harold: Flowfield Measurements About an Airfoil With Leading-Edge Ice Shapes. J. Aircraft, vol. 43, no. 4, 2006, pp. 1226–1234.
31. Lee, Sam; and Bragg, Michael B.: Investigation of Factors Affecting Iced-Airfoil Aerodynamics. J. Aircraft, vol. 40, no. 3, 2003, pp. 499–508.
32. Broeren, Andy, et al.: Aerodynamic Simulation of Runback Ice Accretion. J. Aircraft (AIAA–2009–4261), vol. 47, no. 3, 2010, pp. 924–939.
33. Broeren, Andy P., et al.: Aerodynamic Simulation of Runback Ice Accretion. NASA/TM—2010-215676 (AIAA 2009–4261), 2009.
34. Soeder, Ronald H., et al.: NASA Glenn Icing Research Tunnel User Manual. NASA/TM—2003-212004, 2003. Available from the Center for AeroSpace Information.
35. Cabler, Susan J.M.: Aircraft Ice Protection. Federal Aviation Administration Advisory Circular, AC 20–73A, 2006.
36. Blumenthal, Leia A.: Surface Pressure Measurement on a Three-Dimensional Ice Shape. M.S. Thesis, Univ. of Illinois at Urbana-Champaign, 2005.

37. Wright, William: User's Manual for LEWICE Version 3.2. NASA/CR—2008-214255, 2008.
38. Busch, Greg T.: Ice Accretion Aerodynamic Simulation on a Subscale Model. M.S. Thesis, Univ. of Illinois at Urbana-Champaign, 2006.
39. Vickerman, Mary B., et al.: Toward an Efficient Icing CFD Process Using an Interactive Software Toolkit—SmaggIce 2D. AIAA–2002–0380, 2002.
40. Kim, Han S.; and Bragg, Michael B.: Effects of Leading-Edge Ice Accretion Geometry on Airfoil Performance. AIAA–99–3150, 1999.
41. Blumenthal, Leia A., et al.: Issues in Ice Accretion Aerodynamic Simulation on a Subscale Model. AIAA 2006–262, 2006.
42. Allen, H. Julian; and Vincenti, Walter G.: Wall Interference in a Two-Dimensional-Flow Wind Tunnel, With Consideration of the Effect of Compressibility. NACA Report 782, 1944.
43. McCullough, George B.; and Gault, Donald E.: Example of Three Representative Types of Airfoil-Section Stall at Low Speed. NACA TN 2502, 1951.
44. Busch, Greg T.; Broeren, Andy; and Bragg, Michael B.: Aerodynamic Fidelity of Sub-scale Two-Dimensional Ice Accretion Simulations. AIAA 2008–7062, 2008.
45. Broeren, Andy P.; Busch, Greg T.; and Bragg, Michael B.: Aerodynamic Fidelity of Ice Accretion Simulation on a Subscale Model. SAE Paper 2007–01–3285, 2007.
46. Kim, Han: Effect of Leading-Edge Ice Accretion Geometry on Airfoil Performance. M.S. Thesis, Univ. of Illinois at Urbana-Illinois, 2004.
47. Olsen, W.; Shaw, R.J.; and Newton, J.: Ice Shapes and the Resulting Drag Increase for a NACA 0012 Airfoil. NASA TM–83556 (AIAA–1984–109), 1984.
48. Desplas, P.: F1 Pressurized Subsonic Wind Tunnel User's Guide. Large Technical Facilities, Le Fauga-Mauzac Wind Tunnels Departement, ONERA, France, 1998.
49. Moëns, F.: SUNSET Project: Numerical Investigations for the Preparation of the F1 Test Campaign. ONERA Technical Report No. RT 1/12405 DAAP, ONERA, France, 2007.
50. Kline, S.J.; and McClintock, F.A.: Describing Uncertainties in Single-Sample Experiments. The American Society of Mechanical Engineers Seventy-Seven Year Index Technical Papers 1880–1956, The American Society of Mechanical Engineers, New York, NY, 1953, p. 3.
51. Coleman, Hugh W.; and Steele, W. Glenn, Jr.: Experimentation and Uncertainty Analysis for Engineers. Wiley-Interscience, New York, NY, 1989.
52. CassouDeSalle, D.; and Gilliot, A.: SUNSET (StUdies oN Scaling EffecTs Due to Ice) Tests at High Reynolds Number in F1 Wind Tunnel. ONERA Test Report No. PV 4/12361 DSFM, ONERA, France, 2008.
53. CassouDeSalle, Denis, et al.: Experimental Investigations of Simulated Ice Accretions at High Reynolds Numbers in the Onera F1 Wind Tunnel. AIAA 2009–4265, 2009.
54. Broeren, Andy P., et al.: Effect of High-Fidelity Ice-Accretion Simulations on Full-Scale Airfoil Performance. J. Aircraft, vol. 47, no. 1, 2010, pp. 240–254.
55. Broeren, Andy P., et al.: Effect of High-Fidelity Ice Accretion Simulations on the Performance of a Full-Scale Airfoil Model. AIAA 2008–434, 2008.
56. Jones, B. Melvill: An Experimental Study of the Stalling of Wings. Aeronautical Research Committee Reports and Memoranda No. 1588 (T.3483), Aeronautics Laboratory, Cambridge, U.K., 1933.
57. Haines, A. Barry: Scale Effects on Aircraft and Weapon Aerodynamics. AGARD–AG–323, 1994.
58. Tani, I.: Low-Speed Flows Involving Bubble Separations. Progress in Aeronautical Sciences, Vol. 5, 1964, pp. 70–103.
59. Kerho, Michael F.; and Bragg, Michael B.: Airfoil Boundary-Layer Development and Transition With Large Leading-Edge Roughness. AIAA J., vol. 35, no. 1, 1997, pp. 75–84.
60. Abbott, Ira Herbert; and von Doenhoff, Albert E.: Theory of Wing Sections, Including a Summary of Airfoil Data. Dover Publications, New York, NY, 1959.
61. Lee, Sam, et al.: Geometry and Reynolds-Number Scaling on an Iced Business-Jet Wing. AIAA–2005–1066, 2005.
62. Busch, Greg T.: Experimental Study of Full-Scale Iced-Airfoil Aerodynamic Performance Using Sub-Scale Simulations. Ph.D. Dissertation, Univ. of Illinois at Urbana-Champaign, 2010.
63. Whalen, Edward A.; Broeren, Andy P.; and Bragg, Michael B.: Aerodynamics of Scaled Runback Ice Accretions. J. Aircraft, vol. 45, no. 3, 2008, pp. 1076–1088.
64. Jackson, Darren Glenn: Effect of Simulated Ice and Residual Ice Roughness on the Performance of a Natural Laminar Flow Airfoil. M.S. Thesis, Univ. of Illinois Urbana-Champaign, 1999.

REPORT DOCUMENTATION PAGE	Form Approved OMB No. 0704-0188

1. REPORT DATE *(DD-MM-YYYY)*	2. REPORT TYPE	3. DATES COVERED *(From - To)*
01-06-2011	Technical Paper	

4. TITLE AND SUBTITLE
Aerodynamic Simulation of Ice Accretion on Airfoils

5a. CONTRACT NUMBER

5b. GRANT NUMBER

5c. PROGRAM ELEMENT NUMBER

6. AUTHOR(S)
Broeren, Andy, P.; Addy, Harold, E., Jr.; Bragg, Michael, B.; Busch, Greg, T.; Guffond, Didier; Montreuil, Emmanuel

5d. PROJECT NUMBER

5e. TASK NUMBER

5f. WORK UNIT NUMBER
WBS 457280.02.07.03.02.02

7. PERFORMING ORGANIZATION NAME(S) AND ADDRESS(ES)
National Aeronautics and Space Administration
John H. Glenn Research Center at Lewis Field
Cleveland, Ohio 44135-3191

8. PERFORMING ORGANIZATION REPORT NUMBER
E-17506

9. SPONSORING/MONITORING AGENCY NAME(S) AND ADDRESS(ES)
National Aeronautics and Space Administration
Washington, DC 20546-0001

10. SPONSORING/MONITOR'S ACRONYM(S)
NASA

11. SPONSORING/MONITORING REPORT NUMBER
NASA/TP-2011-216929

12. DISTRIBUTION/AVAILABILITY STATEMENT
Unclassified-Unlimited
Subject Categories: 02, 03, and 05
Available electronically at http://www.sti.nasa.gov
This publication is available from the NASA Center for AeroSpace Information, 443-757-5802

13. SUPPLEMENTARY NOTES

14. ABSTRACT
This report describes recent improvements in aerodynamic scaling and simulation of ice accretion on airfoils. Ice accretions were classified into four types on the basis of aerodynamic effects: roughness, horn, streamwise, and spanwise ridge. The NASA Icing Research Tunnel (IRT) was used to generate ice accretions within these four types using both subscale and full-scale models. Large-scale, pressurized wind-tunnel testing was performed using a 72-in.- (1.83-m-) chord, NACA 23012 airfoil model with high-fidelity, three-dimensional castings of the IRT ice accretions. Performance data were recorded over Reynolds numbers from 4.5×10^6 to 15.9×10^6 and Mach numbers from 0.10 to 0.28. Lower fidelity ice-accretion simulation methods were developed and tested on an 18-in.- (0.46-m-) chord NACA 23012 airfoil model in a small-scale wind tunnel at a lower Reynolds number. The aerodynamic accuracy of the lower fidelity, subscale ice simulations was validated against the full-scale results for a factor of 4 reduction in model scale and a factor of 8 reduction in Reynolds number. This research has defined the level of geometric fidelity required for artificial ice shapes to yield aerodynamic performance results to within a known level of uncertainty and has culminated in a proposed methodology for subscale iced-airfoil aerodynamic simulation.

15. SUBJECT TERMS
Aircraft icing; Airfoil; Aerodynamic stalling; Scale models

16. SECURITY CLASSIFICATION OF:			17. LIMITATION OF ABSTRACT	18. NUMBER OF PAGES	19a. NAME OF RESPONSIBLE PERSON
a. REPORT	b. ABSTRACT	c. THIS PAGE			STI Help Desk (email:help@sti.nasa.gov)
U	U	U	UU	75	19b. TELEPHONE NUMBER *(include area code)* 443-757-5802